

POLITECNICO DI TORINO

Master's Degree in Sustainable Nuclear Energy
A.Y. 2025/2026

Master's Degree Thesis

Computational feasibility study of small sample temperature reactivity worth experiments in the VENUS-F reactor

Supervisors:

Dr. Nicolò ABRATE
Federico DI CROCE
Dr. Antonin KRÁSA

Candidate:

Riccardo GNOCCHI

September 2026

Abstract

Lead-cooled Fast Reactors (LFRs) are a key class of Generation IV nuclear reactors and require comprehensive design qualification and licensing frameworks. Neutronic analysis plays a pivotal role in this process; however, the computational models used require verification and validation steps through high-quality experimental data. Integral experiments conducted in zero-power reactors are essential in providing these inputs. To this end, the zero-power fast spectrum VENUS-F reactor, operated at SCK CEN, serves as a neutronic mock-up of fast heavy-metal-cooled technologies.

Within this context, this work presents a computational feasibility study, based on a Monte Carlo framework, for a new experimental campaign in the VENUS-F reactor. The experiment will be designed to reproduce the temperature feedback mechanisms typical of power reactors, specifically the fuel Doppler effect. The proposed approach relies on measuring the reactivity effect induced by the insertion of small samples in the reactor, focusing on its temperature dependence. The investigation considered multiple experimental locations across the core and temperature ranges that are both achievable within the facility and representative of full-scale applications. ^{238}U was selected as the primary target nuclide. By simulating reaction rates and reactivity effects, a non-negligible temperature dependence was observed, particularly in specific core locations characterized by a more epithermal neutron spectrum. The numerical investigation was subsequently extended to other relevant fissile nuclides (^{240}Pu) and other largely present nuclides and materials (^{56}Fe, Al_2O_3). While ^{240}Pu exhibited a Doppler response comparable to that of ^{238}U, the temperature effect of the other candidates was negligible. In conclusion, by verifying and comparing multiple locations and different temperature gradients, the study successfully identified promising experimental combinations that will allow for the measurement of reactivity changes due to Doppler effect within the VENUS-F reactor.

Acknowledgements

First and foremost, I would like to express my gratitude to SCK CEN for the invaluable opportunity to work in high-level research within the nuclear sector. It has been a privilege to be part of a productive environment defined by its long-term commitment to invest in human talent for a better world.

I am deeply indebted to my supervisor, Federico Di Croce, for his constant support, unwavering availability and crucial guidance in improving this work. I also extend my sincere thanks to my other two supervisors: Antonin Krása, for selecting me for this position and providing highly useful advice, and Nicolò Abrate, for his readiness to help whenever I needed assistance.

To my colleagues at SCK CEN and the people of Boeretang: thank you for making this experience both beautiful and stimulating. You have enriched my time here with shared moments of life that I will never forget. I truly believe our beautiful friendship will easily bridge the thousands of kilometers separating us, keeping us close as a big, warm, and cherished diverse family.

La mia più profonda gratitudine va alla mia famiglia, a mamma, papà e Andrea, per tutto il sostegno che ho ricevuto. Mi avete festeggiato negli alti e incoraggiato nei bassi, senza farmi mai mancare nulla e dandomi la possibilità di vivere appieno le mie esperienze. Dedico a voi questo traguardo. Mi dimostrate costantemente un amore profondo che mi sforzo di meritare ogni singolo giorno. Spero davvero di avervi resi orgogliosi.

Last but certainly not least, I want to thank my girlfriend, Lucrezia. Your love allows me to remain focused on the truly important things in life, which I look forward to building and sharing with you. Thank you for inspiring me to be better, pushing me to become the best version of myself and for giving me the chance to look to the future with eyes full of dreams.

Table of Contents

List of Figures IV

1 Introduction 1
- 1.1 General background . . . 1
- 1.2 Past research on Doppler reactivity coefficient . . . 3
- 1.3 VENUS-F research reactor . . . 6
- 1.4 Objective of the Thesis . . . 8

2 Theory and Methods 10
- 2.1 Reactor Physics . . . 10
- 2.2 Monte Carlo method . . . 13
  - 2.2.1 Neutron flux estimation . . . 14
  - 2.2.2 Reactivity worth computation methods . . . 15
- 2.3 Error propagation . . . 16
- 2.4 Doppler Effect . . . 17
- 2.5 Computational tools . . . 18
  - 2.5.1 SERPENT2 Monte Carlo code . . . 18
  - 2.5.2 Nuclear Data processing . . . 19
  - 2.5.3 Python . . . 22

3 Characterization of models for VENUS-F experiments 23
- 3.1 Detailed model analysis . . . 23
- 3.2 VENUS-F simplified model description and validation . . . 26
  - 3.2.1 Criticality study and modification of simplified model . . . 26
  - 3.2.2 Similarity evaluation . . . 29
  - 3.2.3 Neutron flux spatial distribution . . . 30
- 3.3 Temperature adaptation methods . . . 33

4 Preliminary analysis on Reaction Rates 36
- 4.1 Cross Section Extraction . . . 37
  - 4.1.1 PointWise Representation . . . 38
  - 4.1.2 GroupWise Representation . . . 40
- 4.2 Multi-group Reaction Rates in VENUS-F . . . 42

4.2.1 Energy-dependent and -integrated reaction rate results 42
4.2.2 Reaction Rate variation by temperature change 46

5 ^{238}U reactivity worth calculations 52
5.1 Sample insertion 52
5.2 ^{238}U sample reactivity worth at room temperature 53
5.3 ^{238}U sample reactivity worth temperature variation and trends 57
5.4 Neutron flux and reaction rates in the sample 60
5.4.1 Neutron Flux 61
5.4.2 Reaction rates 63
5.5 Investigation of the $\Delta\rho$ in modified geometries 68
5.5.1 Long sample 68
5.5.2 Hollow sample 69
5.5.3 Alternative core configuration 70

6 Reactivity worth of alternative materials 73
6.1 ^{240}Pu sample temperature-dependent reactivity worth 73
6.1.1 Long sample 75
6.2 Temperature-dependent reactivity worth of additional non-fissile materials 77
6.2.1 ^{56}Fe temperature-dependent reactivity worth 77
6.2.2 Alumina (Al_2O_3) temperature-dependent reactivity worth 79

7 Conclusions 81

A Further insights on cross section production 86
A.1 Number of points for PointWise reconstruction 86
A.2 Impact of the grid choice on GroupWise approach 87

B Flux and Reaction Rates inside the sample 89
B.1 Flux Spectra and Spatial Distributions 89
B.2 Reaction Rates Spatial Distributions 92
B.2.1 Capture Reaction Rates 93
B.2.2 Fission Reaction Rates 94

Bibliography 97

List of Figures

1.1 Thermal cycles on sample employed in [12]. 4
1.2 ZPR-III core schematic [13]. 5
1.3 Computed ^{238}U and ^{240}Pu contribution to Doppler in the MOX fuel analyzed [15]. 5
1.4 VENUS-F Reactor, taken from [18]. 7

2.1 Simplified Random Walk generation algorithm. The probability of reaction x (P_x) is based on a ratio between its cross sections and the total. For simplicity, fission is neglected. 14
2.2 Doppler broadening of U-238 Capture Resonance at 6.67 eV. 18

3.1 VENUS-F neutron flux spectra (top) across four experimental locations for several energy grids and the corresponding statistical uncertainties (bottom). 25
3.2 VENUS-F core models: detailed representation vs first homogenized core, before the modifications for criticality. 26
3.3 On the left, normality check on the implicit k_{eff} by the replicas, with the Shapiro-Wilk method (p-value > 0.05 indicates normality). On the right, k_{eff} replicas convergence, with standard deviation and standard error . . . 28
3.4 Detailed vs. Simplified model: neutron Flux spectrum across all locations. The grey curves refer to the detailed model, the colored to the simplified. The near-perfect overlap indicates high similarity. 30
3.5 Calculated energy-integrated neutron flux spatial distribution in the VENUS-F simplified, critical core model. 31
3.6 VENUS-F simplified, critical core flux for different energy intervals, normalized on the global maximum. 32
3.7 Integrated ^{238}U capture rates comparison: ACE vs TMP. Error bars refer to 1-σ. 35

4.1 PointWise reconstruction of ^{238}U capture cross section, at different temperatures. 39
4.2 PointWise ^{238}U capture cross section in two resonance regions, highlighting the points chosen by NJOY during the reconstruction, for different temperatures. 39

4.3 PointWise and GroupWise representation of ^{238}U capture cross section inside two resonance regions, at two different temperatures. 40
4.4 GroupWise ^{238}U capture cross section, on several grids, overlaid upon the PointWise representation, all at 900 K 41
4.5 ^{238}U capture rate distribution, in all experimental locations, at 300 K and 900 K, for the finest grid (2000 groups). 45
4.6 ^{238}U capture rate variation in the first resonance, in the Lead Reflector, for a temperature jump between 300 K and 900 K. The box reports the exact values, of the highlighted point, from left to right 45
4.7 ^{238}U capture rate cumulative, in the Lead Reflector, for three different temperatures, normalized to the maximum. The capture cross section is shown in grey in the background. 46
4.8 Correlation matrices on the total reaction rates at different temperatures, in all experimental locations under analysis. Top-left: Core Center, top-right: Lead Reflector, bottom-left: Outer Core, bottom-right: Graphite Reflector. 49
4.9 Integral ^{238}U capture rates and their relative percentage variations. Absolute values at the corresponding temperatures are shown in blue (left axis), while relative changes, in percentage, with respect to the 300 K reference value are shown in red (right axis). Errorbars refer to 1-σ. 50

5.1 VENUS-F core vertical layout: perturbed and unperturbed configuration . 53
5.2 Convergence study of $\Delta\rho$ replicas for 300 K ^{238}U sample in the Graphite Reflector experimental assembly. p-value > 0.05 indicates normality. 54
5.3 ^{238}U capture, fission, elastic and inelastic scattering cross sections. 55
5.4 Fission vs capture reaction rates in the ^{238}U sample, distribution in energy, in the Graphite Reflector and Core Center assemblies. 56
5.5 The blue points show the $\Delta\rho$ of ^{238}U sample insertion across various temperatures (bottom x-axis). The green points show $\Delta\rho$ due solely to the temperature jump (top x-axis). Error bars represent 1-σ. 58
5.6 Reactivity worth from ^{238}U sample insertion: computed values and fitting function on temperature. 59
5.7 Comparison of neutron flux inside the ^{238}U sample and in an empty sample volume, in the Graphite Reflector assembly. Sample is at room temperature. 61
5.8 Comparison of neutron flux around the first ^{238}U capture resonance, located at 6.7 eV, inside the sample at 200 K and 900 K. Sample is inside the Graphite Reflector. 62
5.9 Total flux spatial distribution in the ^{238}U sample located in the Graphite Reflector channel. The cuts are horizontal, along the sample midplane and at the north and south of the sample. 63
5.10 Normalized ^{238}U capture rate (energy-integrated), at 300 K, in the sample inserted in the Graphite Reflector (left) and in the Core Periphery (right). The cut is vertical, along the x-axis. 64

5.13 Integral ^{238}U capture rates in the sample, together with their relative percentage variations in temperature. Absolute values at the corresponding temperatures are shown in blue (left axis), while relative changes, in percentage, with respect to the 300 K reference value are shown in red (right axis). Errorbars refer to $1-\sigma$. 65
5.11 ^{238}U capture rates in the five energy intervals, for the Graphite Reflector. Three temperatures are shown. The cut is vertical, along the x-axis. 66
5.12 Fraction of ^{238}U capture rate contained in each radial portion of the sample. In the first plot, the values are integrated over all the energy domain. In the bottom, they refer only to the second energy bin (Table 3.5). In bold, the volume fraction of each portion is indicated. Both capture and total reaction rates are shown. 67
5.14 Mid-plane view of the simplified VENUS-F core, with the new configuration under analysis. The sample is in (-1,1). 71
5.15 Effect of core modification on flux spectra in the Core Center experimental assembly. 72

6.1 ^{240}Pu sample $\Delta\rho$ in two core locations. The blue points show the $\Delta\rho$ of sample insertion across various temperatures (bottom x-axis). The green points show the net $\Delta\rho$ due to the temperature jump (top x-axis). Error bars represent 1-σ. 74
6.2 Capture cross sections of ^{238}U and ^{240}Pu. 75
6.3 Neutron flux in the large sample volume (empty). First figure shows the axial profiles in the Core Periphery and Graphite Reflector; the middle and right figures present the neutron flux spectrum at top edge (bottom is identical), together with the one in the midplane, for the two locations. . . 77
6.4 ^{56}Fe reaction rate distributions in energy: elastic scattering and capture. . 79
6.5 Elastic scattering and capture cross section of ^{16}O. Obtained using SANDY. 80
6.6 The blue points show the $\Delta\rho$ of Al_2O_3 sample insertion across various temperatures (bottom x-axis). The green points show $\Delta\rho$ due solely to the temperature jump (top x-axis). Error bars represent 1-σ. 80

A.1 Total RMSE for w=2 and multiple grids, at different temperatures 87
A.2 Local RMSE inside five different energy regions 88

B.1 Comparison of neutron flux without and inside the sample, in the Core Periphery assembly. Sample is at room temperature. 90
B.3 Total flux spatial distribution in the sample located in the Graphite Reflector channel. The cuts are vertical, along two perpendicular orientations. The core midplane is located at z=79.64. 90
B.2 Comparison of neutron flux around the first capture ^{238}U resonance, located at 6.7 [eV], inside the sample at 200 K and 900 K. Sample is inside the Core Periphery. 91

B.4 Total flux spatial distribution in the sample located in the Core Periphery channel. The cuts are horizontal, along the middle and near the ends. . . 91
B.5 Total flux spatial distribution in the sample located in the Core Periphery channel. The cuts are vertical, along two perpendicular orientations. The core midplane is located at z=79.64. 92
B.6 Normalized capture reaction rate, at 300 K, in the sample inserted in the Graphite Reflector channel. The cut is horizontal, at three heights. 93
B.7 Normalized capture reaction rate, at 300 K, in the sample inserted in the Core Periphery channel. The cut is vertical, along two directions. 93
B.8 Normalized capture reaction rate, at 300 K, in the sample inserted in the Core Periphery channel. The cut is horizontal, at three heights. 94
B.9 Normalized fission reaction rate in the sample inserted in the Graphite Reflector channel. The cut is vertical, along two directions. 95
B.10 Normalized fission reaction rate in the sample inserted in the Graphite Reflector channel. The cut is horizontal, at three heights. 95
B.11 Normalized fission reaction rate in the sample inserted in the Core Periphery channel. The cut is vertical, along two directions. 96
B.12 Normalized fission reaction rate in the sample inserted in the Core Periphery channel. The cut is horizontal, at three heights. 96

Chapter 1

Introduction

1.1 General background

Nuclear power will be a major player in the future decarbonization of the electricity grids of industrialized countries, in the pursuit of Net Zero goals, while also offering new opportunities for sustainable growth in developing regions and economies [1]. In the last decades however, especially in the western world, the deployment of new nuclear power plants faced growing obstacles, both techno-economical and related to social acceptance. These problems have pushed toward the development of new designs and approaches to nuclear reactors, namely the so called "Generation IV" or "Gen IV". They comprise very diverse technologies, all with the shared characteristics of applying a new approach on specific areas, as the safety [2]. Specifically, Gen IV reactors rely on passive or intrinsic safety features, ensuring the reactor safety during accidental conditions without any external action. On the downside, these designs entail new challenges that must be overcome to successfully convert the on-paper projects in real, reliable and cost-effective technologies.

Among these new designs, much effort has been put towards the development of Lead-cooled Fast Reactors (LFRs) [3]. Thanks to the high thermal capacity of lead, they operate at ambient pressure, far from the boiling point, therefore avoiding the fast loss of coolant typical of pressurized reactors and the consequent core overheating in case of primary loop breach. Moreover, they offer the possibility to close the fuel cycle. Long lived radioactive elements, like minor actinides, produced as a by-product during operations by previous generation reactors, requiring millennial-scale waste management strategies, can indeed serve as fuels for LFRs. This capability stems from operating with a fast neutron spectrum in the reactor core. Conversely, since this is a novelty for large scale projects, the neutron interactions at fast energies had been investigated and studied far less.

The lack of knowledge affects many areas of reactor design and licensing, from material choice to the validation of computational tools. Focusing on the latter, one of problems regards the reliability of neutronic simulations, which are heavily dependent on input data such as the Nuclear Data [4] [5]. Nuclear Data have been identified as one of the

most important sources of uncertainty in the neutronic design of many advanced systems, significantly impacting the evaluation of relevant reactor parameters [6]. In MYRRHA [7], one of the most prominent heavy-metal-cooled reactor concepts, the Doppler reactivity coefficient suffers from relevant uncertainty [6]. The Doppler coefficient contributes to determine the reactor response to any power transient and it is one of the main focus for safety studies and licensing. Exploring this issue further, Fiorito et al. identified a critical need for further development in fast-spectrum nuclear data evaluation [8]. The work focused on the uncertainty quantification of the Doppler reactivity feedback coefficient in MYRRHA. Specifically, it analyzed the impact of nuclear data uncertainties on the Doppler reactivity coefficient (K_D), defined as the change in system reactivity associated with a temperature variation. Table 1.1 reports the relative standard deviation on K_D from the nuclear data uncertainties, which is of the order of 2-3% and seems independent of the temperature jump.

Model	$T_1 \rightarrow T_2$	$\sigma_{K_D,\mathrm{ND}}/K_D$
MYRRHA full 3D core	300 → 900 K	3.0%
	900 → 1800 K	2.1%
	300 → 1800 K	3.0%

Table 1.1: Nuclear data uncertainty on Doppler reactivity coefficient (K_D) in MYRRHA [8].

The two main contributors to the uncertainty are ^{238}U and ^{240}Pu, yielding uncertainties of the order of 1.5 to 2%. This highlights the necessity of nuclear data improvement of specific nuclides to reduce uncertainties in the Doppler reactivity coefficient in fast systems.

New experimental campaigns, engineered for assessing the accuracy and precision of nuclide-specific and reaction-specific data, are then required. In fact, high quality experimental results can be used for validation and improvement of nuclear data. Integral experiments in zero power reactors can give a relevant contribution, also regarding the Doppler reactivity coefficient.

1.2 Past research on Doppler reactivity coefficient

Reactivity effects have been extensively measured in research reactors. A primary application is the estimation of the reactivity worth of small samples inserted into the reactor core to characterize their nuclear properties. To quantify this effect, different experimental techniques are available, which can be classified according to the approach implemented [9]:

- **Compensation with control rods:** Following the insertion of the sample, the reactor critical state is re-established by compensation with control rods. The reactivity worth of the sample is directly inferred from the movement of the rod during a single-step procedure.
- **Sample oscillation:** The technique relies on a cyclic perturbation, implemented via either mechanical movement ("mechanical oscillation") or temperature modulation ("temperature oscillation"). The reactor power floats freely, and the reactivity is deduced from the resulting neutron flux fluctuations.
- **Closed-loop oscillation:** Combining aspects of both approaches, this method pairs periodic sample insertion with reactivity compensation by means of a pilot rod. The sample is oscillated while an automatic pilot rod continuously compensates for the induced perturbation, maintaining the reactor stable at constant power level. As for the compensation method, the pilot rod displacement yields the reactivity.

Beyond standard reactivity measurements, these techniques can also be applied to evaluate the Doppler effect. Doppler reactivity effect, or more in general, temperature reactivity coefficients, have been investigated since the early years of nuclear power commercialization. A wide range of integral experiments on Doppler reactivity effects have been conceived and performed over time; some of these studies provide crucial insights for this investigation. This section provides a concise review of the existing experimental literature that has inspired and guided the analysis presented in the work.

Pearce and Walker [10] measured the metallic uranium temperature reactivity coefficient, by means of sample oscillation in ZEEP, the Zero Energy Experimental Pile built at the Chalk River Laboratories, in Ontario [11]. It is a thermal system, with heavy water as moderator. The samples were oscillated sinusoidally at 2.55 $\pm$ 0.02 cycles per minute, between high and low flux zones for several hours. An interesting aspect of this study was the temperature range. In fact, both heated and cooled samples were investigated, for temperature ranges from 30 °C to 230 °C and from 10 °C to -140 °C, yielding a slightly larger coefficient for the cooled case.

Kato and Butler presented Doppler temperature effect measurements in an EBR-I Assembly mock up inside ZPR-III [12], the fast critical assembly constructed at the Argonne National Laboratory. The experimental setup was similar to the one in Pearce et al. [10], employing metallic uranium samples and deriving the reactivity change from the neutron flux fluctuation. However, in this case, there was no physical movement of the

sample, and the reactivity effect came from cyclically oscillating the sample temperature (Figure 1.1).

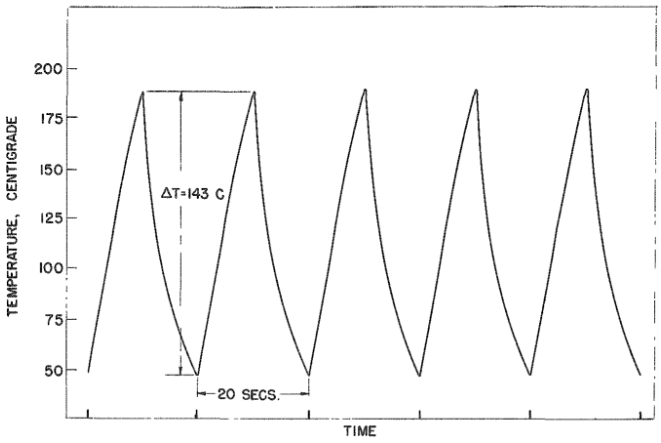


Figure 1.1: Thermal cycles on sample employed in [12].

The thermal volume expansion issue was tackled fabricating the uranium elements in the form of a helix. The paper contains two key features relevant to this work. First of all, they also measured plutonium samples for comparison with metallic uranium. While the uranium shows a quite strong negative reactivity effect, plutonium tends to provide a positive feedback. Second, for the interpretation of the results, the neutron flux importance variation in different spatial directions inside the reactor was estimated. Both features (the investigation of plutonium and neutron importance in the core) will be considered in this study.

Doppler effect measurements were carried out in the ZPR-III facility [13] exploiting a two-zone method. The Doppler effect in UO_2 pellets with the temperature regulated by an external heater (keeping the heated sample at around 800 K) was measured. The heated sample replaced the room temperature one, and the reactivity worth was evaluated with the compensation method. Figure 1.2 shows a schematic of the core and the two positions where the samples were kept.

In addition to the choices on the setup, an interesting result regards the reactivity variation depending on the neutron flux spectrum in the experimental location. In fact, the reactivity measurements were repeated with a slightly modified assembly, providing a softer spectrum. Specifically, the results show a more pronounced Doppler effect in the softer, more thermalized spectrum. The relevance of the energy range constitutes a central theme in this work.

Doppler reactivity effect measurements were recently carried out in the FCA facility, Japan's only critical assembly for the study of the neutronic characteristics of fast reactors [14], using sample oscillation technique [15]. The chosen material consisted in MOX fuel. The results were then compared with calculations implemented in standard code systems, obtaining good agreement. Also in this case, the material investigated were uranium and plutonium, in particular ^{238}U and ^{240}Pu. These two nuclides are particularly relevant to

Doppler effects [16] [17], although their contribution to the Doppler reactivity effect is distributed differently in energy, as shown in Figure 1.3. The figure depicts the calculated Doppler index for both isotopes (defined as DIX $= \phi \cdot N \cdot \delta\sigma$, where ϕ is the neutron flux, N the atomic number density, and $\delta\sigma$ the cross-section variation), highlighting the specific resonances that drive the Doppler effect for each nuclide.

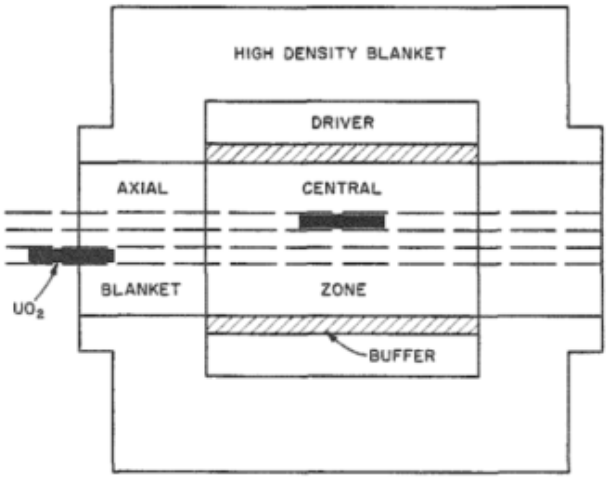


Figure 1.2: ZPR-III core schematic [13].

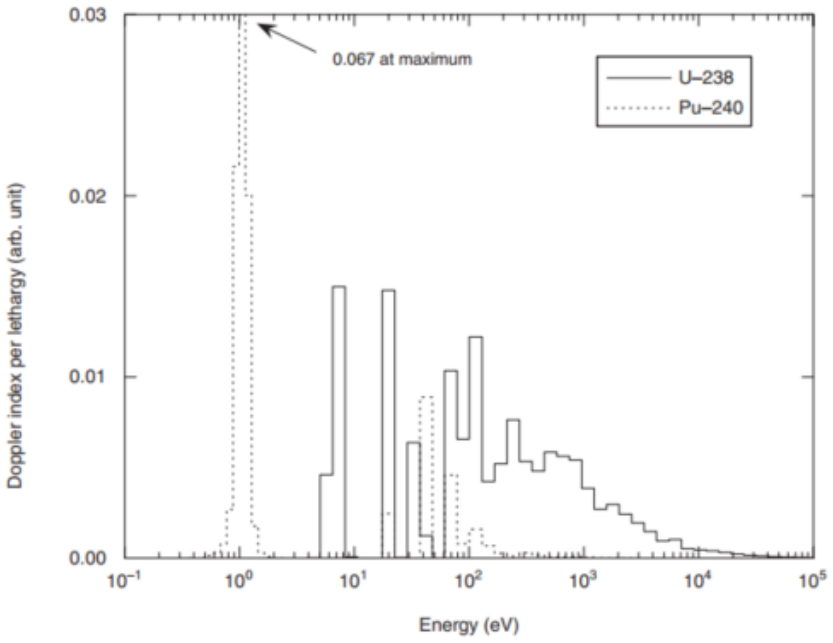


Figure 1.3: Computed ^{238}U and ^{240}Pu contribution to Doppler in the MOX fuel analyzed [15].

The Doppler index energy dependence provides insights on the energy regions where the Doppler effect is most influential, being mostly concentrated in the low epithermal part. This additional information is key; indeed, energy-range considerations will be frequently addressed throughout this work.

Table 1.2 summarizes the measurements presented in this section, characterizing them according to the most important parameters in the context of this work: the reactor neutron flux spectrum, the sample materials, the experimental method and the temperature ranges investigated.

Paper	Spectrum	Material	Method	Temperature Range
Pearce et al. [10]	T	U	Mechanical oscillation	(−140, 230) °C
Kato et al. [12]	F	U, Pu	Temperature oscillation	(50, 193) °C
Gasidlo et al. [13]	F, E	U	Compensation	(300, 800) K
Andoh et al. [15]	F	U, Pu	Closed loop oscillation	(300, 800) °C

Table 1.2: Features of measurements performed in the papers. F=Fast, E=Epithermal, T=Thermal.

1.3 VENUS-F research reactor

As outlined in Section 1.1, integral experiments in research reactors can be informative on the accuracy and precision of nuclide- and reaction-specific nuclear data. In this context, the VENUS-F reactor, operated at the Belgian Nuclear Research Centre (SCK CEN), plays a central role (Figure 1.4).

Specifically, VENUS-F is a fast spectrum research reactor designed to improve the knowledge of nuclear data and support the development of lead-based Gen-IV systems [18]. Originally designed as a thermal, water-moderated reactor, it was later transformed to support the development of those technologies, with a particular focus on the MYRRHA project.

VENUS-F is a zero-power reactor (lower than 100 W), operating at ambient temperature without need of active cooling. The reactor is highly flexible. The reactor core contains materials in solid form, which can be replaced and rearranged to resemble in materials and configurations different types of lead fast reactors. The rectangular core, surrounded by a lead reflector, comprises assemblies in a 12x12 lattice. The assemblies can be reflective (with lead or graphite) or fuel-based. The fuel assemblies house the fuel rodlets, containing 30% enriched metallic uranium, surrounded by solid material rodlets and plates designed to simulate specific coolant material compositions.

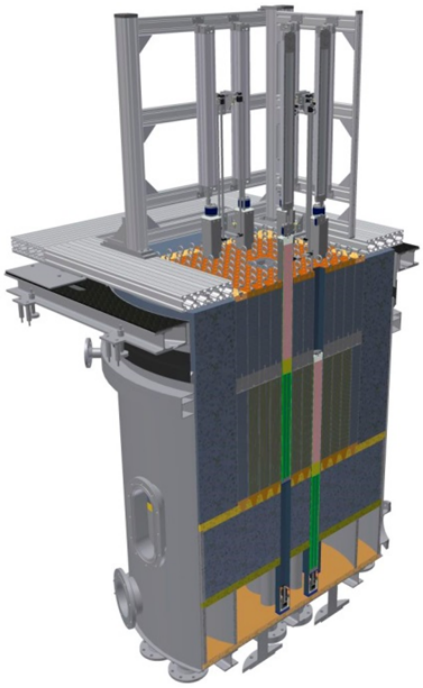


Figure 1.4: VENUS-F Reactor, taken from [18].

At the present day, oscillation experiments are being carried out in VENUS-F, aiming at measuring small sample reactivity worth [19]. The samples are oscillated following a trapezoidal waveform, between the midplane and the reactor top. Through ^{235}U fission chambers, the neutron flux is monitored and later used to reconstruct the sample reactivity. The paper reports the validation of the experimental process for a B_4C sample, obtaining an uncertainty in the order of 0.03-0.04 pcm.

Another way to study the Doppler reactivity effect in VENUS-F exists; it has already been implemented in the past and reported in 2017 by Krása et al. [20]. In the study, several integral experiments were performed, and one measured the reactivity induced by a 4 K increase in core temperature, quantified at $-(2.9 \pm 0.3)$ pcm. Comparative simulation were also carried out, and good agreement with the experimental results was found. However, heating the entire core entails several practical complications, thus a different approach is required.

1.4 Objective of the Thesis

Considering the need of accurate nuclear data and code validation to design future fast reactors, several neutronic experiments are performed in VENUS-F. Among these, following the past research on temperature reactivity effects, the study of the Doppler effect is now being proposed, by oscillating small samples at different temperatures. Specifically, the sample reactivity worth temperature variation directly links to the Doppler reactivity effect. A primary constraint lies in the magnitude of the perturbation: the global reactivity effect induced solely by a temperature change in a small sample is generally minor, and the measurement precision is a limiting factor. While a sufficiently large temperature variation, sample volume, or material density would yield a clearly measurable perturbation, such ideal conditions are rarely feasible in an existing facility with spatial and thermal handling constraints.

Therefore, the requirements demanded by the experimental conditions suitable for capturing the features of the Doppler effect must match the capability of performing such experiments in the VENUS-F facility.

The objective of the thesis is thus to define the optimal and feasible experimental conditions to measure the Doppler reactivity effect produced by inserting a small sample in the VENUS-F core. The study is entirely computational, employing the high-fidelity SERPENT2 Monte Carlo code, and working on a simplified but physically representative model of VENUS-F reactor core.

The analysis will explore several different setups, taking into account the constraints, which are:

- **Measurement precision**: The measurements will be performed using the oscillation technique, which allows measuring reactivity effects of the order of 1–10 pcm with a precision of approximately 0.03 pcm [19]. Consequently, the computational predictions must demonstrate significant reactivity effects, ideally around two orders of magnitude greater than the achievable experimental uncertainty.

- **Realizable temperature**: While simulations allow the temperature to be adjusted arbitrarily over broad ranges, experimental conditions impose strict physical boundaries. In practice, the achievable sample temperatures are constrained between an estimated lower limit of 77 K and an upper bound of approximately 1200 K.

- **Location of the experimental channels**: The measurements cannot be performed at an arbitrary position in the reactor, but only in specific experimental assemblies. These assemblies have fixed characteristics, in term of neutron flux spectra and adjoint flux (importance) profiles.

In order to have a full picture on the possibility to perform such experiments and their features, the simulations will compute the reactivity worth dependence on:

- **Sample characteristics**: Various sizes and geometrical configuration will be tested; moreover, the investigation will involve different materials, comparing their capability

of perturbing criticality and the magnitude of the Doppler reactivity effect within them.

- **Temperature ranges**: Both heating and cooling will be investigated, evaluating the effect by a temperature jump from room temperature (300 K). The aim is to identify the most promising pathway to reach the intended goal, while characterizing the reactivity response in temperature.
- **Spectral conditions**: The study investigates sample oscillation across several experimental channels distributed throughout different core regions, namely the center and periphery of the fuel zone, as well as the lead and graphite reflectors. As hinted in the previous studies, the neutron energy distribution in the experimental location will have an influence on the sample reactivity change due to temperature variation. The calculations will evaluate this influence and its consequence on the feasibility of the experiments.

Chapter 2

Theory and Methods

This chapter presents the theoretical knowledge, resolution methods and numerical applications useful for the treatment of the problem analyzed in the work. The following sections outline the fundamental physics principles, the statistical and uncertainty propagation theory underlying the calculations and procedures developed, along with a brief overview of the computational tools employed.

2.1 Reactor Physics

The governing equation for studying the behavior and interaction of neutrons in matter is the so called "transport equation", reported in Equation 2.1. It arises from a neutron balance on a differential volume in the phase space, a 7 variables space including geometrical coordinates, energy, direction of flight and time. The formulation starts from the definition of a *neutron angular density* (N):

$$N(\mathbf{r}, \mathbf{\Omega}, E, t)$$

that is the expected number of neutrons at the position $\mathbf{r}$, with direction Ω, energy E at time t, per unit volume, direction of flight, energy and time [21]. The integration over the differential phase-space volume element ($dV\, d\Omega\, dE\, dt$) gives the expected number of neutrons within that region of the phase space. The other key components of the transport equation are the macroscopic cross section (Σ), defined as the interaction probability of neutrons with matter per unit length of travel. They generally depend only on the geometrical coordinates (for the different position of the materials) and energy, even though some interactions can have different probability of emission at different directions. The balance include the fission neutron emission spectra (χ), the scattering function (f_s), the fraction of delayed neutron (β), the neutron multiplicity (ν), the source term (S) and the concentration of delayed precursors (C_i).

$$\begin{cases} \dfrac{1}{v}\dfrac{\partial\phi(\mathbf{r},E,\mathbf{\Omega},t)}{\partial t} + \mathbf{\Omega}\cdot\nabla\phi(\mathbf{r},E,\mathbf{\Omega},t) + \Sigma_t(\mathbf{r},E)\phi(\mathbf{r},E,\mathbf{\Omega},t) \\ \quad = \displaystyle\int dE' \int d\Omega'\, \Sigma_s(\mathbf{r},E')\phi(\mathbf{r},E',\mathbf{\Omega}',t)\, f_s(\mathbf{r},E'\to E,\mathbf{\Omega}'\to\mathbf{\Omega}) \\ \qquad + \dfrac{\chi_p(\mathbf{r},E)}{4\pi}\displaystyle\int dE' \int d\Omega'\,(1-\beta)\,\nu(\mathbf{r},E')\Sigma_f(\mathbf{r},E')\phi(\mathbf{r},E',\mathbf{\Omega}',t) \\ \qquad + \dfrac{\chi_d(\mathbf{r},E)}{4\pi}\displaystyle\sum_{i=1}^{R}\lambda_i C_i(\mathbf{r},t) + S(\mathbf{r},E,\mathbf{\Omega},t) \\ \dfrac{\partial C_i(\mathbf{r},t)}{\partial t} = -\lambda_i C_i(\mathbf{r},t) + \beta_i \displaystyle\int dE' \int d\Omega'\,\nu(\mathbf{r},E')\Sigma_f(\mathbf{r},E')\phi(\mathbf{r},E',\mathbf{\Omega}',t) \end{cases} \tag{2.1}$$

The transport equation is formulated in terms of the neutron flux (ϕ), defined as the product of the neutron angular density and scalar velocity (v). The neutron flux is a convenient choice for computing many parameters of primary interest, such as the power produced by fission, or the activation of a material caused by neutron absorption. The full transport equation is a time dependence problem, considering both prompt and delayed neutrons. The latter are produced by the decay of certain fission products (precursors) and their evolution is governed by Equation 2.1. This allows a precise description of the neutrons behavior, considering the different timescales of their generation and their effect on the overall balance.

Steady state (time-independent) transport equation is used in criticality problems and the equation is simplified down to [22]:

$$\begin{aligned} \mathbf{\Omega}\cdot\nabla\Phi(\mathbf{r},E,\mathbf{\Omega}) + \Sigma_t(\mathbf{r},E)\Phi(\mathbf{r},E,\mathbf{\Omega}) \\ = \int dE' \int d\Omega'\, \Sigma_s(\mathbf{r},E'\to E,\mathbf{\Omega}'\to\mathbf{\Omega})\Phi(\mathbf{r},E',\mathbf{\Omega}') \\ + \frac{\chi(\mathbf{r},E)}{4\pi}\frac{1}{k}\int dE' \int d\Omega'\,\nu(\mathbf{r},E')\Sigma_f(\mathbf{r},E')\Phi(\mathbf{r},E',\mathbf{\Omega}'). \end{aligned} \tag{2.2}$$

The equation now has the form of an eigenvalue problem, introducing the eigenvalue $1/k$ to obtain a non-trivial, time-independent solution [22]. The effective multiplication factor, k_{eff}, represents the first, fundamental eigenvalue of the system. In a generational framework, it quantifies the ratio of the total neutron population between successive generations (neutron flux multiplication). The value of k_{eff} indicates the stability of the system, and its variation characterizes a new quantity, the reactivity. The reactivity of the system quantify the distance from criticality and it is defined as the k_{eff} relative deviation from criticality ($k_{\text{eff}} = 1$). The reactivity is often indicated in pcm (1×10^5):

$$\rho = \frac{\delta k}{k} = \frac{k-1}{k} \tag{2.3}$$

To have additional information on the neutron characteristics in the phase space, focusing on their capability to produce a desired outcome, the *Adjoint transport equation*

(Equation 2.4) is defined. It is a separated mathematical formulation whose physical significance is the description of neutron importance (ϕ^+). This new equation exploits the transport operators, defining their adjoints, applying them to the balance of the importance of neutrons, which is proportional to their ability to induce the reaction of interest (e.g., fission in power reactors).

$$\begin{aligned} -\mathbf{\Omega}\cdot\nabla\phi^+(\mathbf{r},E,\mathbf{\Omega}) + \Sigma_t(\mathbf{r},E)\phi^+(\mathbf{r},E,\mathbf{\Omega}) \\ = \int dE' \int d\Omega'\, \Sigma_s(\mathbf{r},E')\phi^+(\mathbf{r},E',\mathbf{\Omega}')\, f_s(\mathbf{r},E'\to E,\mathbf{\Omega}'\to\mathbf{\Omega}) \\ + \frac{1}{k^+}\int dE' \int d\Omega'\, \nu(\mathbf{r},E')\Sigma_f(\mathbf{r},E')\frac{\chi(\mathbf{r},E)}{4\pi}\phi^+(\mathbf{r},E',\mathbf{\Omega}') \end{aligned} \tag{2.4}$$

Reactivity effects can be studied in the framework of *Perturbation Theory*, employing both normal and adjoint transport equations. This allows a quantification, in terms of reactivity, of the deviation from stable conditions caused by a perturbation in the system. Its formulation is based on combining the perturbed transport equation with the importance function. After these manipulations, an exact equation for the reactivity is obtained [21] (left side of Equation 2.5). This formulation can simplified via first order approximation, under the hypothesis of small flux perturbation ($\phi_2 \approx \phi_1 + \delta\phi$, $\hat{A}' \approx \hat{A} + \delta A$ for a generic operator A), neglecting second order contributions:

$$\rho = \frac{<\phi_1^+|\hat{F}'\phi_2> - <\phi_1^+|\hat{L}'\phi_2>}{<\phi_1^+|\hat{F}'\phi_2>} \approx \frac{<\phi_1^+|\delta\hat{F}\phi_1> - <\phi_1^+|\delta\hat{L}\phi_1>}{<\phi_1^+|\hat{F}\phi_1>} \tag{2.5}$$

where $\hat{F}', \hat{L}'$ are the perturbed fission and transport operators, the δ indicate their small variation (for example a change on the cross section), <> indicates integration over the phase space and the subscripts 1,2 indicate, respectively, the unperturbed and perturbed state.

Exact perturbation theory also yields the definition of reactivity *worth* [23]:

$$\Delta\rho = \rho_2 - \rho_1 = \frac{k_2 - k_1}{k_1 k_2} = \frac{\langle\phi_1^+|\frac{1}{k_{\text{eff},2}}\delta\hat{F}\phi_2\rangle - \langle\phi_1^+|\delta\hat{L}\phi_2\rangle}{\langle\phi_1^+|\hat{F}_1\phi_2\rangle} \tag{2.6}$$

As previously, a simplified form exists, approximating the perturbed flux with the original ($\phi_2 \approx \phi_1$) and it is valid for small and localized perturbations. Due to its simplicity, it is usually the most used, but a careful handling is required due to its blindness to second order effects and the possibility of flux distortions if the perturbation is strong.

The reactivity is a fundamental quantity for various reasons: first of all, it is the main input for reactor transient analysis, essential for safety studies in nuclear power plants. Furthermore, reactivity effect measurements in research reactors are widely used for core characterization and nuclear data investigation. These types of experiments lie at the core of the thesis motivation, as explained in the previous chapter.

2.2 Monte Carlo method

The Monte Carlo method is a statistical technique used to simulate a mathematical or physical experiment on a computer [24]. It has a very broad scope of application, encompassing integrals estimations, uncertainty propagation and random walk treatment. For reactor physics, the latter serves as the foundation for the study of particle transport. The approach is not based on directly solving the transport equation, but instead on a stochastic simulation of the process, by generating a number of neutron histories, and following each particles from the emission (by an external source or fissile materials for criticality calculation) to the leakage or absorption. It can be done thanks to the stochastic interpretation of the cross sections, as probability of interaction per traveled distance. Indeed, considering a neutron traveling in an interactive medium with cross section Σ, its probability of interaction in an interval dx around x is $\Sigma(x) \cdot dx$. Then, the number of neutron starting from x and arriving in $x + dx$ is:

$$N(x + dx) = N(x)[1 - \Sigma(x) \cdot dx] \tag{2.7}$$

By separating the variables and integrating, it can be demonstrated that the neutron population, in a interactive media, along its travel length, is exponentially distributed, with a probability density function as:

$$f(x) = \Sigma(x) e^{-\int_0^x \Sigma(x) dx} \tag{2.8}$$

Hence, it is possible to sample the free flight of a neutron, applying the *Inverse transform method*:

1) Random number generation ρ, uniformly distributed in [0,1]

2) Pose ρ equal to cumulative: $\rho = F(x)$

3) Compute free flight (L) inverting the cumulative: $L = x$

For a homogeneous medium: $L = -\frac{1}{\Sigma} \ln(\rho)$

A simplified algorithm for random walk generation is shown in Figure 2.1.

Once a sufficient number of neutron histories has been simulated, results are extracted from "tallies" (or detectors), which record the quantities under analysis within specific regions of the phase space. What constitutes a "sufficient number" varies from problem to problem. Because this is a statistical method with a finite number of iterations, the final results will always carry statistical uncertainty, which will be dependent on the number of neutron histories. The bridge between average values obtained from a stochastic simulation of a probability-based phenomenon and the real features of the physical mechanism is provided by the Central Limit Theorem, which states [25]:

Assumptions Let $X_1, X_2, \ldots, X_n$ be a sequence of random variables satisfying the following conditions:

- They are **independent and identically distributed**.
- They have a **finite expected value**: $\mathbb{E}[X_i] = \mu$.
- They have a **finite and strictly positive variance**: $\mathrm{Var}(X_i) = \sigma^2 \in (0, \infty)$.

Statement Let $\bar{X}_n = \frac{1}{n}\sum_{i=1}^{n} X_i$ be the sample mean of the first n variables. As the sample size n approaches infinity, the standardized random variable converges to a standard normal distribution $\mathcal{N}(0, 1)$:

$$\frac{\bar{X}_n - \mu}{\sigma/\sqrt{n}} \xrightarrow{d} \mathcal{N}(0, 1)$$

In brief, for a large enough sample size, the mean of the result distribution converge onto the expected value of the physical phenomenon.

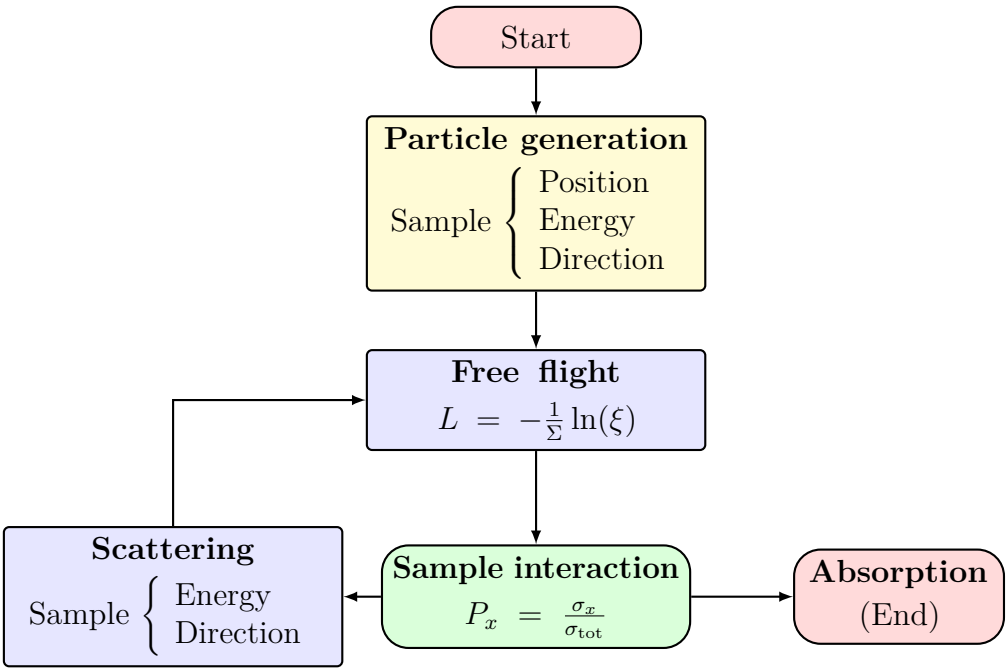


Figure 2.1: Simplified Random Walk generation algorithm. The probability of reaction x (P_x) is based on a ratio between its cross sections and the total. For simplicity, fission is neglected.

2.2.1 Neutron flux estimation

In particle transport, Monte Carlo methods often estimate flux from the collision density. A conservation equation for it can be derived, over the whole phase space, including the source of particles as a zero-th collision (Q_c) and a general transport kernel (K) (combination of transition between points in the phase space and collision kernels). Equation 2.9 shows the incoming particles collision density (ψ) conservation relationship [26].

$$\psi(P) = Q_c(P) + \int dP' \psi(P') K(P', P) \tag{2.9}$$

Generally, in MC transport codes, a functional of the collision density is scored inside the detectors [26]. This functional is called reaction rate, and its formula includes the probability function of the response (reaction) under analysis (Equation 2.10). Different types of detector response can be drawn by the same set of random walks, only changing the probability function, also called "pay-off function" (f_ψ) [26] .

$$R = \int dP \, f_\psi(P) \, \psi(P) \tag{2.10}$$

For neutron transport, in the phase space, Equation 2.10 then becomes:

$$R = \iint d\mathbf{r} \, dE \, f(\mathbf{r}, E) \, \psi(\mathbf{r}, E) \tag{2.11}$$

where the definition of the pay-off function determines the quantity to be retrieved. For example, for the collisional estimations of the integral flux, f is the inverse of the total cross section (or zero if the position $\mathbf{r}$ is outside the domain of interest).

Alternatively, the scalar flux $\bar{\Phi}_V$ within a target volume V can be evaluated using the track-length estimator. This approach relies directly on the fundamental definition of scalar flux as the total distance traveled by particles per unit volume and time. In a Monte Carlo simulation, the average flux is calculated by summing the segment lengths traversed by all particles inside the volume and averaging over the total number of simulated histories N:

$$\bar{\Phi}_V = \frac{1}{V \cdot N} \sum_{i=1}^{N} \sum_{j} w_{i,j} \cdot l_{i,j}$$

where $w_{i,j}$ is the statistical weight of particle i during its j-th segment, and $l_{i,j}$ is the path length spent inside volume V. Unlike the collision estimator, which scores a contribution only when a nuclear interaction occurs, the track-length estimator tallies a non-zero value for every particle traversing the volume, regardless of whether a collision takes place. This improves the statistical accuracy, in particular for small samples or weakly interacting media.

2.2.2 Reactivity worth computation methods

Reactivity variations can be calculated in Monte Carlo through different approaches. One strategy relies on *Perturbation Theory*, whose theory is described in Section 2.1. Various implementation of the first-order version of perturbation theory are available in several Monte Carlo codes, including SERPENT2, which exploits a collision-based approach [27].

On the other hand, a vastly used method for computing reactivity changes is the EigenValues Difference Method (EVDM) [28], implementing the the formula:

$$\Delta\rho = \frac{k_2 - k_1}{k_1 k_2}, \tag{2.12}$$

which computes the reactivity worth ($\Delta\rho$) as the eigenvalue difference in two criticality simulations of the two states (1, 2) under analysis. This will be the standard method used in the following calculations, exploiting its simplicity. Nonetheless, it has limitations. In particular, when calculating small reactivity variations (such as in pile-oscillation experiments), subtracting two large, independent eigenvalue estimates results in large relative uncertainties. A very large computational time is then required to drive the variance down in both states.

Therefore, considering the fact that in this work the target uncertainty for the k_{eff} computations is around 0.5 pcm (1-σ), in order to assess quite accurately the temperature effect, a single pair of Monte Carlo simulations would be too time-consuming. Thus, random sampling through parallel calculations [29] is exploited. Computation time is reduced by executing simulations in parallel across multiple compute nodes. In particular, the methodology implemented requires generating many replicas of "fast" simulations, and then combining the results exploiting their statistical independence. The replicas in each configuration produce a k_{eff} vector with N components, and Formula 2.12 is applied for each pair of values. This yields the $\Delta\rho$ distribution across replicas, from which we derive the best estimate and its associated uncertainty. This procedure can be applied on any couple of k_{eff} vectors.

$$\begin{pmatrix} k_1^1 \\ k_2^1 \\ \vdots \\ k_N^1 \end{pmatrix}, \begin{pmatrix} k_1^2 \\ k_2^2 \\ \vdots \\ k_N^2 \end{pmatrix} \xrightarrow{\text{EVDM}} \begin{pmatrix} \Delta\rho_1 \\ \Delta\rho_2 \\ \vdots \\ \Delta\rho_N \end{pmatrix} \quad \Bigg| \quad \begin{aligned} &\textbf{Sample Average:} \\ &\bar{\Delta}\rho = \frac{1}{N}\sum_{i=1}^{N}\Delta\rho_i \\ &\textbf{Sample Standard Deviation:} \\ &s = \sqrt{\frac{1}{N-1}\sum_{i=1}^{N}(\Delta\rho_i - \bar{\Delta}\rho)^2} \\ &\textbf{Sample Standard Error:} \\ &\text{SE} = \frac{s}{\sqrt{N}} \end{aligned} \tag{2.13}$$

2.3 Error propagation

The random sampling procedure described before allows quantifying the uncertainty from the distribution of the results. However, error propagation can be performed via First-Order Propagation. Two distinct implementations of to FOP are present in this work. First, it was used to check the statistical independence of the simulations. Since every single k_{eff} value in the two vectors described in Equation 2.13 is computed in a separate MC simulation, they should be mutually independent. To verify this, the FOP formula has been applied at every n-th step to the two n-th averaged k_{eff} values. After a sufficient number of iterations, the results coincided with the standard deviation computed as in Equation 2.13. To put it briefly, mathematically speaking:

$$s = \sqrt{\frac{1}{N-1}\sum_{i=1}^{N}(\Delta\rho_i - \bar{\Delta\rho})^2} \longrightarrow \sqrt{\frac{\sigma^2_{\bar{k}_{1,n}}}{\bar{k}^4_{1,n}} + \frac{\sigma^2_{\bar{k}_{2,n}}}{\bar{k}^4_{2,n}}} \tag{2.14}$$

Additionally, other parts of the work required a more structured application of FOP. In fact, under the assumption of model linearity, uncertainties are propagated using the sandwich formula by combining the input covariance matrix with the model's sensitivity matrix [30]:

$$\mathbf{\Sigma}_Y \approx \mathbf{J}\,\mathbf{\Sigma}_X\,\mathbf{J}^T \tag{2.15}$$

where $\mathbf{\Sigma}_Y$ is the output covariance matrix, $\mathbf{\Sigma}_X$ is the input covariance matrix, and $\mathbf{J}$ is the Jacobian matrix representing the model sensitivities. Detailed descriptions of the implemented linear uncertainty propagation formulations are provided case by case.

2.4 Doppler Effect

The Doppler effect is the thermal broadening of the resonance cross-sections of a nuclide due to the thermal motion of the nucleus [31]. Figure 2.2 shows the first capture resonance of ^{238}U (at 6.67 eV) across various temperatures, showing how increased thermal motion flattens and broadens the peak. Microscopically, the probability of neutron interaction with matter (i.e. cross section) depends on the relative velocity between the particle and the nucleus. However, the nucleus belongs to the atom, that is in continuous motion, due to its thermal energy, with a distribution dependent on temperature. Consequently, as temperature increases, the thermal motion distribution broadens; when the cross section is averaged over this distribution, the resonance peak becomes shorter and wider [31]. This phenomenon leads to a variation of neutron interaction probability that in a nuclear system results in energy-dependent reaction rates variation that can be locally positive or negative. Macroscopically, temperature changes during operational and accidental transients always result in a Doppler reactivity feedback that plays a critical role in core stability and reactor safety.

The impact of the Doppler reactivity effect depends on the core configuration and materials [32]:

- In thermal reactors, it provides a prompt negative feedback, able to respond to quick reactivity insertions, by decreasing the neutron probability of escaping the resonance zone while thermalizing.
- In fast designs, it can be the largest contributor to the net power coefficient of reactivity [33], but its effect can also be slightly positive, for example for some sodium-cooled reactors [32]. Yet, in fast systems, it has not been thoroughly studied.

The Doppler reactivity feedback is commonly expressed by the Doppler coefficient, K_D:

$$\frac{dk}{dT} = \frac{K_D}{T} \tag{2.16}$$

where k is the effective multiplication factor, and T represents the average fuel temperature. The large uncertainty on K_D is critical for reliable core safety evaluations [8] and effort must be paid to accurately characterize and reduce it. Furthermore, the impact of Doppler broadening strongly depends on the neutron energy spectrum; the relative increase in absorption is substantially larger at lower resonance energies compared to fast energies [33] due to larger cross-sections.

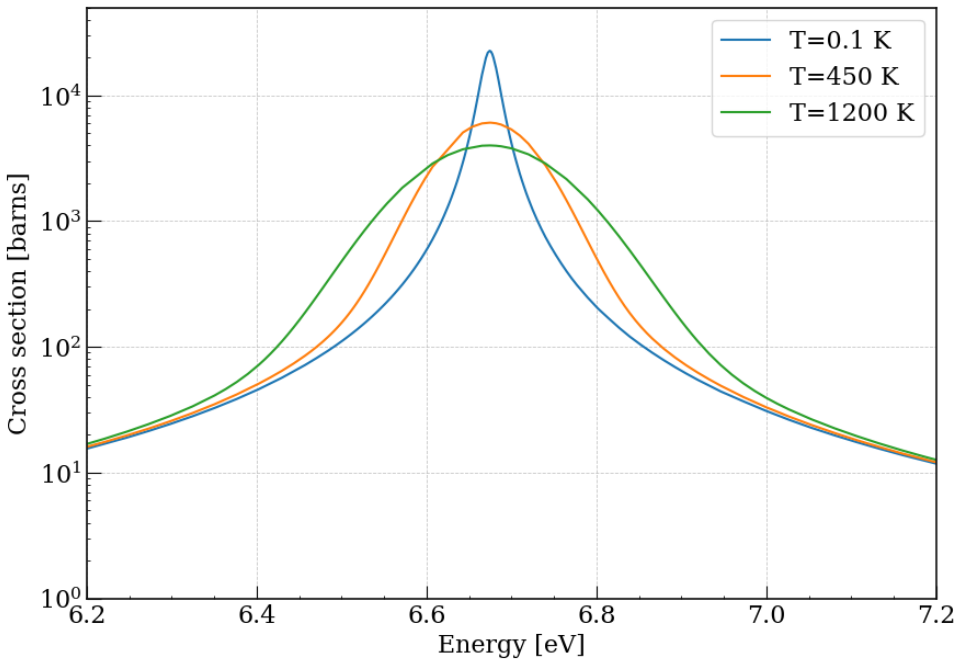


Figure 2.2: Doppler broadening of U-238 Capture Resonance at 6.67 eV.

2.5 Computational tools

This section provides a brief overview of the tools and codes used for nuclear data processing, transport simulations, uncertainty analyses and general computations required for the study.

2.5.1 SERPENT2 Monte Carlo code

SERPENT2 [34] is a 3D continuous-energy Monte Carlo code for neutron and photon transport, featuring built-in burnup calculation capabilities. Its core capabilities span traditional reactor physics, such as spatial homogenization, criticality safety, and fuel cycle analysis, multi-physics coupling with thermal-hydraulics, CFD, and fuel performance codes, as well as radiation transport and shielding for dose evaluations, fusion research, and medical physics. The code relies on ACE-format cross-section libraries derived from

evaluated nuclear data files (ENDF). Every nuclide in the simulation links directly to the nuclear data. Nuclides are grouped to form materials entities. Each material can be at different temperature and this is handled by two distinct material temperature adaptation mechanisms:

1. **Doppler broadening pre-processor:** Invoked via the *tmp* card alongside the target temperature (in Kelvin), this routine broadens the base cross sections, taken from the lowest available temperature file, prior to the transport calculation, storing it in the memory. This approach avoids computational overhead during tracking, though it increases the memory footprint.

2. **On-the-fly adjustment (TMS):** Activated using the *tms* card, this method performs Doppler broadening dynamically ("on-the-fly") during the simulation as cross sections are queried. It only stores in memory the lowest temperature data. While this eliminates additional memory burden, it can lead to a slight reduction in computational performance.

The geometry is defined by assigning specific materials to each spatial region of the model. Criticality calculations stochastically solve the steady-state problem described in Equation 2.2 using a power iteration scheme divided into two stages: inactive cycles, which allow the fission source distribution to converge from an initial guess, and active cycles, where particle events are scored to reduce the uncertainty of the estimators. Fission source convergence during the inactive cycles, essential to eliminate bias in the observables, is monitored using the Shannon entropy. The primary observable of this calculation is the effective multiplication factor, k_{eff}, which is estimated via [35]:

1. Analog estimator: its an average of the scaling factor employed between successive generations to normalize the neutron population in the system at each cycle.

2. Implicit estimator: it has different levels of optimization, but it is generally based on using a combination of the fission (F), scattering (S), leakage (L) and total (T) rates. For example, for high optimization modes, it is calculated as:

$$k_{\text{eff}} = \frac{F}{T - L - S} \tag{2.17}$$

2.5.2 Nuclear Data processing

Nuclear Data (ND) are a pivotal component of this work. Therefore, the methodologies for storing and processing these data were analyzed, with a particular focus placed on the ENDF format due to its ability to efficiently store diverse datasets and formatting structures within a single file. This format encompasses various regularly updated libraries containing distinct evaluations.

Nuclear data are stored in a machine-readable, FORTRAN-formatted files structured hierarchically called ENDF-6. The data are organized into numbered files. Each file contains specific resources that can be retrieved directly or combined to construct more

complex parameters. Generally, these evaluated datasets consist of tabular data derived from experimental measurements combined with nuclear models. These evaluated files are subsequently processed into specific output formats suitable for visualization or direct integration into transport codes.

Cross section and resonance representation:

For cross section data the ENDF-6 format adopts a dual representation. In the continuous energy regions, data are provided in a PointWise format, whereas in the resonance energy ranges, they are described by adding contributions by resonance parameters.

These parameters are contained in **File 2** (`MF=2`), which consists of a single section, primarily intended for incident neutron evaluations. The presence of a flag indicates that the resonance contributions must be calculated from these parameters and added to the background PointWise cross sections. Within the Resolved Resonance Region (RRR), this parametric representation can be expressed using various formalisms (such as Single-Level Breit-Wigner, Multi-Level Breit-Wigner, Reich-Moore, or R-Matrix). Conversely, for the Unresolved Resonance Region (URR), where only the Single-Level Breit-Wigner (SLBW) formalism is permitted, the cross sections are treated through probability tables.

NJOY 2016

The NJOY Nuclear Data Processing System is one of the most prominent nuclear data processing tools, developed in the 1970s at Los Alamos National Laboratory [36]. It is a Fortran-based code which allows direct interface with ENDF-6 files for nuclear data processing. It includes several modules [37], and the ones most relevant to this work are:

- **RECONR:** Reconstructs PointWise (energy-dependent) cross sections using ENDF resonance parameters and interpolation schemes. It reads an ENDF-6 file and constructs a unified energy grid across all reactions, ensuring that any cross section can be retrieved via linear interpolation within a specified tolerance. The final PointWise cross sections are written onto a "point-ENDF"(PENDF) file. This functionality is essential for the procedures outlined in Chapter 4, particularly for generating accurate nuclear data. A more in-depth description is provided in that chapter.

- **BROADR:** Performs Doppler Broadening and thinning on PointWise cross sections, implementing the point-kernel method. Its procedures are related to the `RECONR` module, especially in the consistency of the energy grid choice. In fact, the `BROADR` module often modifies the discretization of the grid, in order to allow an accurate representation of the new curves.

  By definition, the cross section at a given temperature is the one that would produce the same reaction rate as stationary target nuclei. Then [37]:

$$\rho v\overline{\sigma}(v,T) = \int d\mathbf{v}\prime\rho|\mathbf{v}-\mathbf{v}\prime|\sigma(|\mathbf{v}-\mathbf{v}\prime|)P(\mathbf{v}\prime,T) \tag{2.18}$$

where $\mathbf{v}$ is the velocity of the incident particles, $\mathbf{v\prime}$ is the velocity of the target, ρ is the density of target nuclei, σ is the cross section, and $P(\mathbf{v\prime}, T)$ is the distribution of target velocities in the laboratory system. Integration in terms of relative speed gives the standard form of the Doppler-broadened cross section:

$$\overline{\sigma}(v) = \frac{\alpha^{1/2}}{\pi^{1/2} v^2} \int_0^\infty dV \sigma(V) V^2 \left\{ e^{-\alpha(V-v)^2} - e^{-\alpha(V+v)^2} \right\} \tag{2.19}$$

where $\alpha = \frac{M}{2kT}$, k is Boltzmann's constant, M is the mass of the target nucleus and the relative speed is $V = |\mathbf{v} - \mathbf{v\prime}|$. `BROADR` implements a numerical evaluation of the formula, exploiting the piecewise linearity of the PENDF format. The results are analyzed in the cross section treatment in Chapter 4.

- **GROUPR:** Generates self-shielded multi-group cross sections, group-to-group scattering matrices, photon production matrices, and charged-particle multi-group cross sections from pointwise input. Among these features, only the first is relevant to this work, specifically in Chapter 4. The cross section (Σ), later saved in a "group-ENDF" (GENDF) file, are folded in the multi-group form by means of an integral average on the energy group, with a arbitrary weighting function ($W(E)$):

$$\Sigma^g = \frac{\int_{E_g}^{E_{g-1}} dE \Sigma(E) W(E)}{\int_{E_g}^{E_{g-1}} dE W(E)} \tag{2.20}$$

SANDY

SANDY is a python package that can read, write and perform a set of operations on nuclear data files in ENDF-6 format [38]. It was developed for the stochastic sampling-based generation of perturbed nuclear data files, which are subsequently used for uncertainty propagation. Operating as a wrapper for NJOY, it allows users to bypass direct Fortran input file construction by implementing built-in functions to obtain the desired outputs. Some SANDY methods have been used in this study, specifically:

- `get_endf6_file`: Fetches the ENDF file corresponding to the indicated library, material and nuclear parameter.
- `get_pendf`: Constructs the NJOY input file for the production of PointWise files, with the given characteristics, like reconstruction tolerance, specific nuclear reaction and temperature.
- `get_gendf`: Constructs the NJOY input file for the production of GroupWise files, with possible additional inputs regarding the energy grid and weighting flux.
- `get_xs`: It is implemented in various forms in the different classes, generally works on the PENDF or GENDF file extracting the cross section in the form of pandas DataFrame [39].

- `get_ace`: Similar to `get_pendf` and `get_gendf`, returns an ACE file in DOS format that, after conversion to UNIX, can be used as a input file in the MC simulation in SERPENT2.

2.5.3 Python

Most of the processing and data analysis workflow was developed in Python (version 3.11). It was chosen for its versatility, extensive scientific ecosystem, and efficient data handling. The Python-based modular approach adopted ensured the reproducibility of results and provided flexibility during the debugging and optimization phases of the analysis. Python was used as the core tool for the following activities:

- **Interaction with SANDY:** The code was utilized for the practical integration and execution of the SANDY tool [38], enabling the cross section extraction with specific input parameters.
- **Cross Section Management and Analysis:** Cross sections extracted with SANDY were processed and archived using the `pandas` library [40]. The use of DataFrame structures optimized performance, ensuring rapid manipulation, filtering, and aggregation of large volumes of tabular data.
- **Interfacing with SERPENT2:** The extraction of the SERPENT2 results, for example neutron fluxes from detectors, was automated via the `serpentTools` package [41]. This tool facilitated the parsing of Serpent 2 output files, making data immediately accessible for post-processing stages.
- **Calculations and Visualization:** Python was employed to combine and process data from various sources. Finally, graphical components were managed through specialized libraries (such as `matplotlib` [42] and `seaborn` [43]), allowing for the generation of plots compliant with scientific documentation standards.

Chapter 3

Characterization of models for VENUS-F experiments

The objective of this work is to investigate the reactivity worth of heated/cooled samples in the VENUS-F zero power research reactor. Since the reactivity worth is an integral parameter, the computational study must be carried out on the full geometry model of the reactor. A detailed model including exact fuel assemblies geometry and material composition is available. Although this model provides accurate results [44], simulations are computationally intensive and require tens of hours to reach the required precision for the observable of this study, see Section 2.2.2.

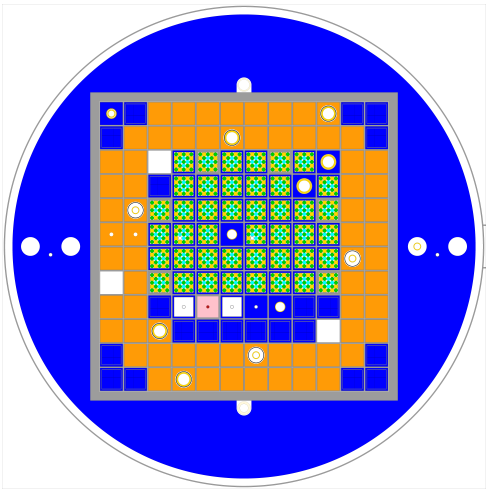
To speed up the calculations, while maintaining sufficient model accuracy, a simplified model has been developed, applying several strategies to light-up the computational overhead. This model was used in the work for the reactivity worth calculations, after being analyzed to ensure criticality and consistency with the detailed model.

The chapter analyzes both models, highlighting the features which will be relevant for this work; moreover, it concludes with an exploration into SERPENT2 material temperature adaptation methods, aimed at selecting the most suitable approach to finally study the temperature reactivity worth.

3.1 Detailed model analysis

The detailed model captures all core characteristics, including internal assembly features. The fuel assembly comprises enriched uranium, bismuth and Al_2O_3 rodlets in a square lattice, surrounded by lead plates inside a stainless steel casing. The neutron flux spectrum in specific experimental locations in the core are studied to highlight the features of their neutron energy distribution. Table 3.1 shows the core model, together with the locations under analysis and the terminology used throughout this study.

VENUS-F Detailed Model



Exp. locations under analysis

Region	**(X, Y)**
Core Center	(-1, 1)
Outer Core	(3, 3)
Core Periphery	(4, 4)
Lead Reflector	(2, -3)
Graphite Reflector	(-1, 5)

Table 3.1: VENUS-F detailed model, together with the experimental positions investigated.

The neutron flux was tallied using four energy grids, see Figure 3.1. The relative uncertainty on each energy bin is also reported in the bottom plot. A few key considerations can be made:

- **Fission peak**: All the locations presents a maximum around 0.5 MeV, attributable to the fission reactions, which heavily drops at higher energies. The peak becomes increasingly pronounced with greater distance from moderating materials.

- **Epithermal tail**: Moving further from the core center, the neutron flux becomes softer, with the epithermal tail appearing in the outer regions of the core and getting more and more pronounced. As expected, the region with the largest number of "slow" neutron is the Graphite Reflector, thanks to the moderation by the carbon.

- **Statistical Uncertainties**: The plots show the close relationship that exists between the rarity of an event and the uncertainty of the statistical observable derived from that event. In fact, the energy regions which are most difficult to reach for a neutron, are the ones with the biggest uncertainties. Moreover, the 2000 groups energy grids presents generally higher Monte Carlo errors for a similar reason. Indeed, keeping the same energy domain, an increased number of groups reduces the probability of a neutron going into a specific bin, therefore its associated uncertainty grows.

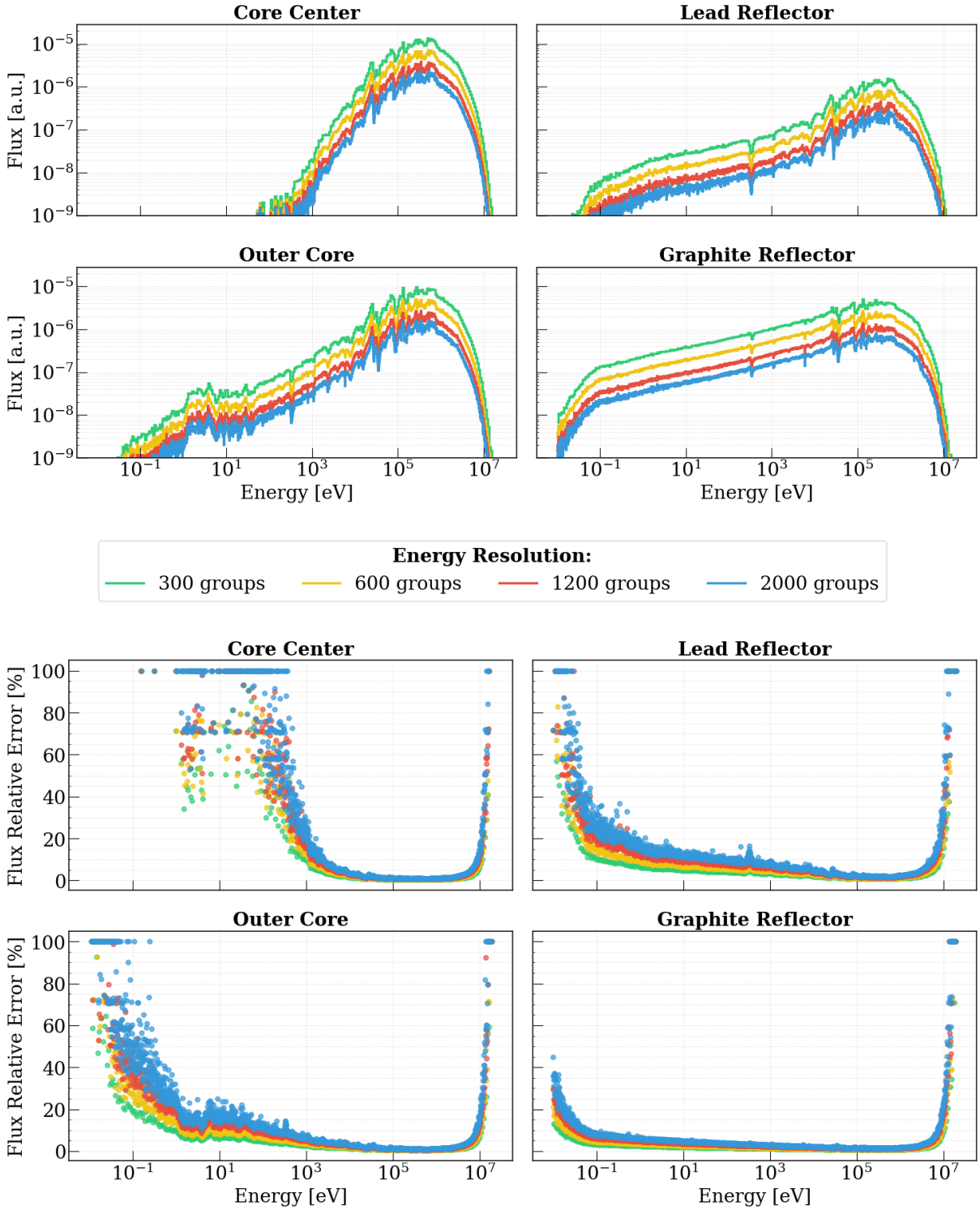


Figure 3.1: VENUS-F neutron flux spectra (top) across four experimental locations for several energy grids and the corresponding statistical uncertainties (bottom).

3.2 VENUS-F simplified model description and validation

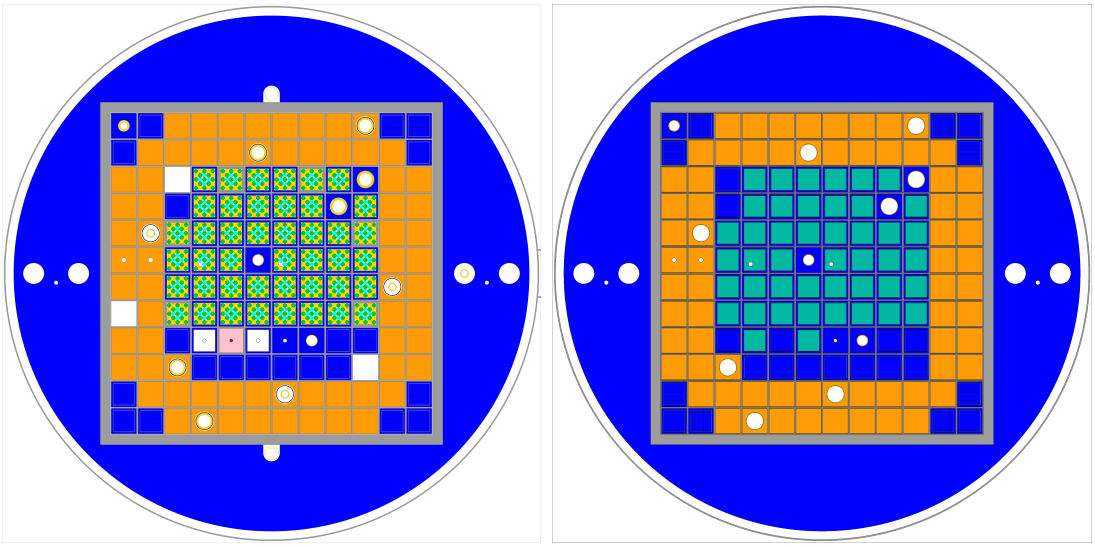
This section analyzes the simplified model of the VENUS-F reactor. Its development regarded syntax simplification, which was done by SCK CEN colleague Daan Houben, modification of some experimental assemblies and homogenization of the fuel assemblies, together with the removal of not-essential details. After being developed and tested, it required further elaborations before its implementation for the reactivity worth calculations. In particular:

1. Criticality study of the simplified model.
2. Model modification to reach as close as possible to criticality.
3. Similarity computation between the new simplified model and the full detailed one.

The following sections outline these preparatory procedures performed prior to the reactivity worth computations.

3.2.1 Criticality study and modification of simplified model

Figure 3.2 shows the detailed core and the first configuration of the simplified.



(a) Full detailed core **(b)** Simplified core

Figure 3.2: VENUS-F core models: detailed representation vs first homogenized core, before the modifications for criticality.

The replacement and homogenization of some important parts of the core modified the system multiplicativity; therefore, its eigenvalue must be investigated. The model has

been run in various simulations, with different combinations of number of neutrons, active and inactive cycles. First, the simulations were run quickly, around 50 minutes (5.5×10^8 simulated histories), not to minimize the MC statistical error as much as possible, but to get a quick preliminary overview. The simulation showed a supercriticality of around 3200 pcm, pretty far from criticality. Then, a long simulation (7×10^9 simulated histories) was run, arriving at around 1 pcm uncertainty and 3278 pcm supercriticality.

Since the simulations of interest focus specifically on criticality calculations, modifications on the model are required to reduce the excess reactivity. Table 3.3 contains the visual representation and description of several modifications. These adjustments were inspired by the visual comparison with the detailed model, in Figure 3.2a, in particular:

- Substitution of reflector assemblies with air
- Insertion of control rod
- Replacement of fuel assemblies with reflectors
- Insertion of void experimental assemblies

At this stage, also the fission source convergence has been checked, by studying the convergence of the Shannon entropy over the inactive cycles. Moreover, for every setup, the eigenvalue convergence has been checked, making sure that the simulated histories are enough to have reasonably accurate values for the purpose.

Finally, after the best configuration has been identified, it was used for more in-depth analyses, with the aim of reducing the MC uncertainty under 0.5 pcm. This is necessary since the computations on the temperature reactivity worth are expected to have values around 1-10 pcm. In order to reduce the uncertainty, instead of lunching one big simulation, several fast replicas of the same model were produced and run in parallel, exploiting the SCK-CEN multi-node cluster. This reduces the overall time needed for the computations. More detailed are reported in Section 2.2.2.

250 replicas were produced and run, their eigenvalue was extracted and, after a normality test, combined for the average value and its standard error. Table 3.2 reports the computational effort for the single replica and Figure 3.3 shows the normality check, the sample average convergence of the implicit k_{eff}, together with the standard deviation of the replicas' population and the standard error. The reference eigenvalue for the unperturbed situation is then:

$$\mathbf{k_{eff} = 1.000472 \pm 0.000048e} \tag{3.1}$$

Average single replica running time	26 min
Average single replica memory allocation	6186.3 MB

Table 3.2: Average computational effort of the replicas

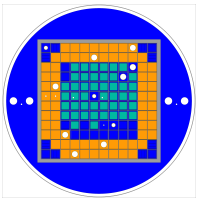
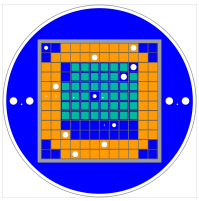
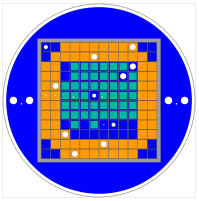
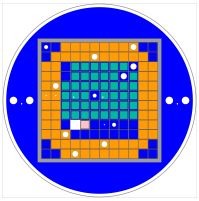
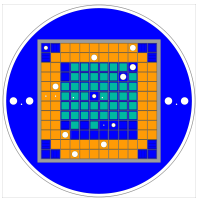
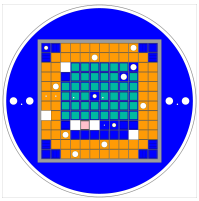
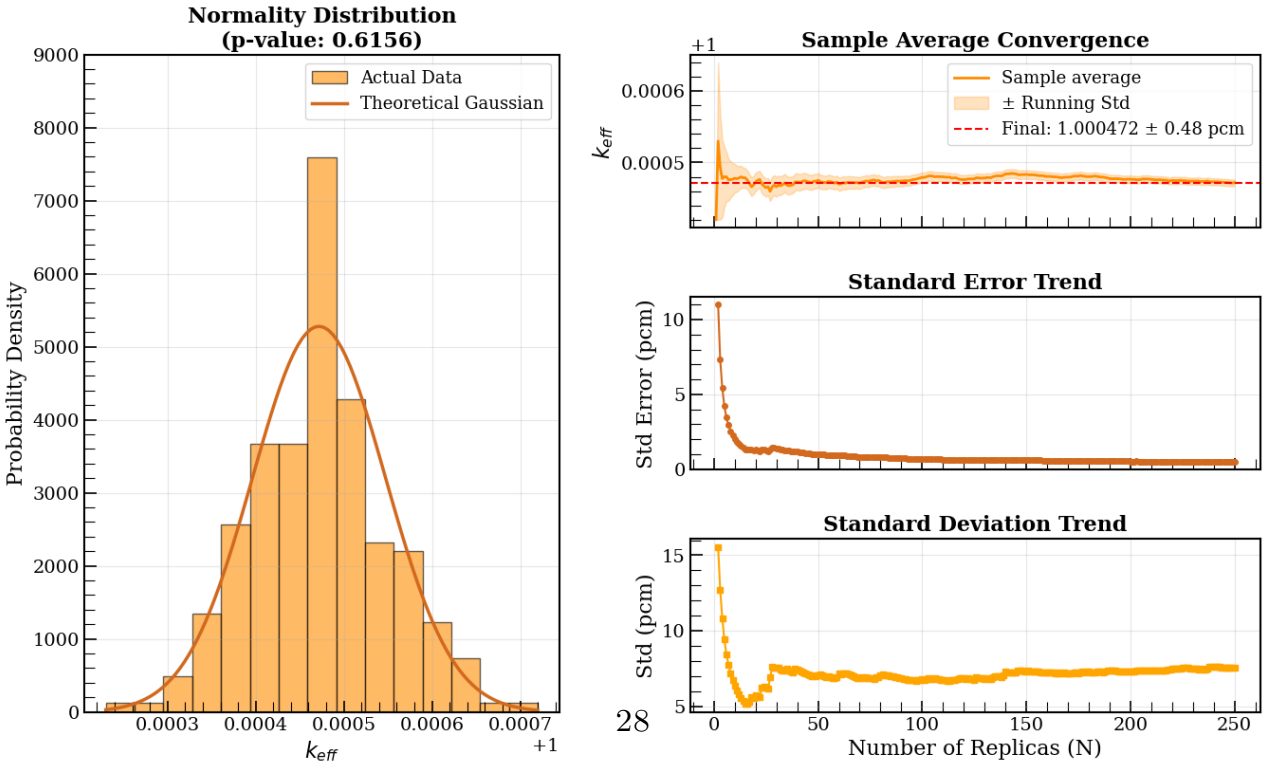
Before	Modified	Adjustments
		• Substitution of two fuel assemblies in (-1,-3) , (-3,-3) with lead reflectors • **Supercriticality:** 2302 ± 4 pcm
		• Substitution of the fuel assembly (-1,-3) with lead reflectors • Substitution of the fuel assembly (-3,-3) with air • Replacement of lead reflector (-2,-3) with control rod • **Supercriticality:** 918 ± 5 pcm
		• Substitution of fuel assemblies (-1,-3), (-3,-3) with air • Substitution of graphite reflector (-5,-2) with air • Substitution of lead reflectors (-4,4), (4,-4) with air • Insertion of void experimental channel in (5,-1) • Replacement of lead reflector (-2,-3) with control rod • **Supercriticality:** 48 ± 5 pcm

Table 3.3: Intermediate VENUS-F simplified model modifications for criticality.

Figure 3.3: On the left, normality check on the implicit k_{eff} by the replicas, with the Shapiro-Wilk method (p-value > 0.05 indicates normality). On the right, k_{eff} replicas convergence, with standard deviation and standard error



3.2.2 Similarity evaluation

The homogeneous simplified model was designed to accelerate calculations without sacrificing essential physical information. Therefore, the model was studied comparing the neutron flux and reaction rates within the experimental channels with the fully detailed model. Previewing the topics of the next chapter, the ^{238}U capture rate is used for the comparison. Preserving these key reactor characteristics during model simplification is essential to ensure that reactivity worth results remain representative of the system.

The metric used to quantify the goodness of the simplified model is the cosine similarity, calculated with Equation 3.2, on the flux and reaction rate vectors. It evaluates the energy orientation of spectral vectors by measuring the correspondence between their distributions.

$$\cos(\theta) = \frac{\mathbf{A} \cdot \mathbf{B}}{\|\mathbf{A}\|\|\mathbf{B}\|} = \frac{\sum_{i=1}^{n} A_i B_i}{\sqrt{\sum_{i=1}^{n} A_i^2}\sqrt{\sum_{i=1}^{n} B_i^2}} \tag{3.2}$$

Figure 3.4 shows the neutron flux spectra, for the two models. It's clear that, apart from the slightly bigger statistical noise on the new values (just due to smaller the simulated histories of the simulation), the flux is very well represented. Table 3.4 instead presents the values of cosine similarity, for the four experimental locations, for fluxes and reaction rates, at 300 K. Other temperatures have been considered for the reaction rate comparison, yielding practically identical results.

Location	**Fluxes [%]**	**Reaction Rates [%]**
Core Center (-1,1)	99.9	99.6
Outer Core (3,3)	99.6	99.7
Lead Reflector (2,-3)	99.9	99.6
Graphite Reflector (-1,5)	99.7	99.9

Table 3.4: Cosine similarity for fluxes and ^{238}U capture reaction rates (at 300 K), in the four experimental locations.

The cosine similarity values for both neutron fluxes and reaction rates demonstrate an excellent correspondence across all investigated locations, with results consistently exceeding 99.5%. Specifically, the flux cosine similarities range from 99.6% in the Outer Core to 99.9% in the Inner Core and Lead Reflector. Likewise, the reaction rate similarities at 300 K remain exceptionally high, varying between 99.6% and 99.9% in both core and reflector regions. These near-unity values confirm a nearly identical energy distribution between the compared vectors, proving that the simplified model captures the spectral behavior with high fidelity regardless of the spatial region.

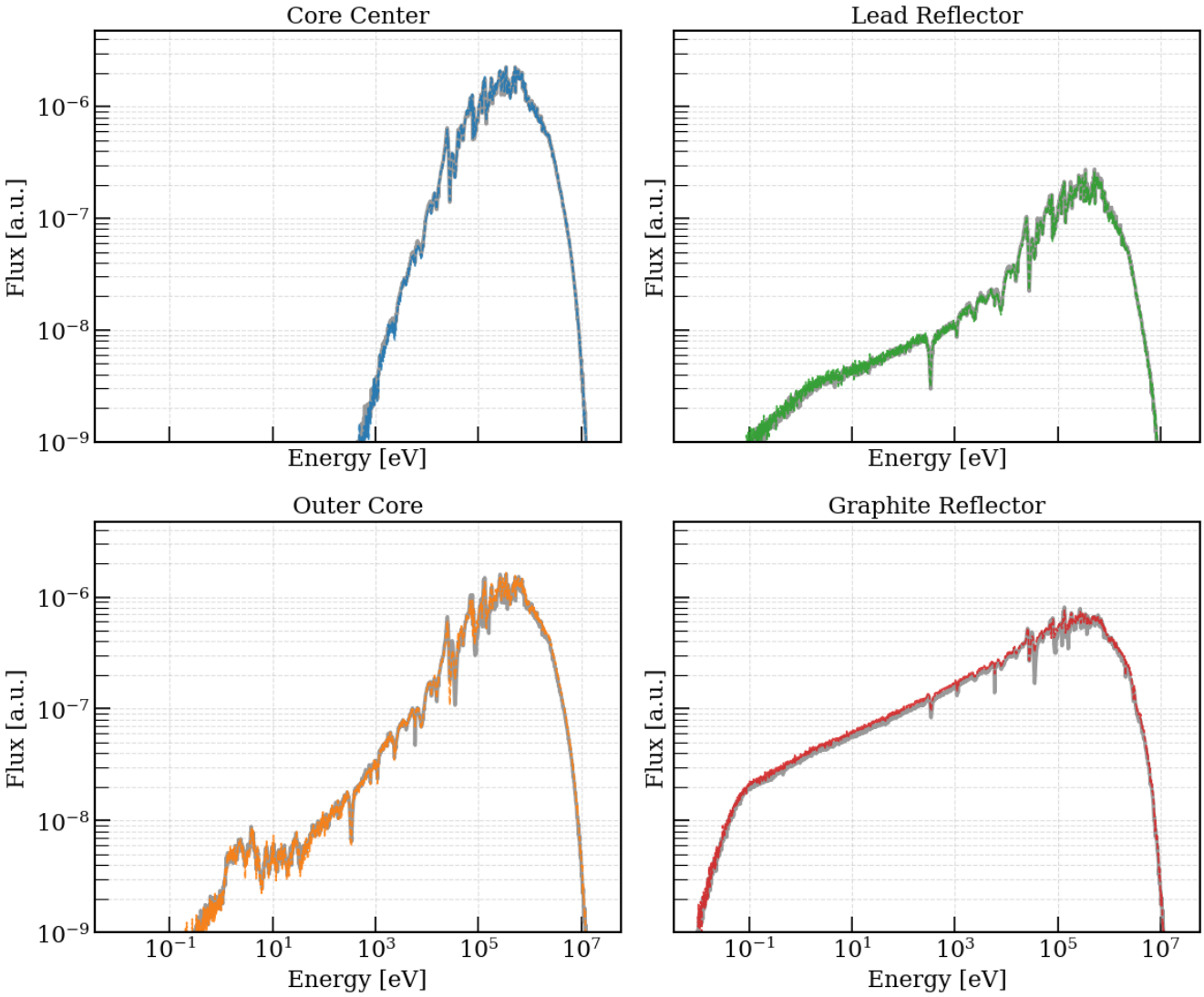


Figure 3.4: Detailed vs. Simplified model: neutron Flux spectrum across all locations. The grey curves refer to the detailed model, the colored to the simplified. The near-perfect overlap indicates high similarity.

3.2.3 Neutron flux spatial distribution

The global effect caused by the sample on the reactor is influenced not only by the spectral conditions in the location where it is inserted, but also by the actual neutron flux magnitude where the sample is inserted. Thus, the spatial neutron flux distribution must be analyzed. Moreover, reactor theory indicates that the neutron importance has a key role in the reactivity perturbation. Even if, in general, the importance is not proportional to the flux, it can be at least roughly evaluated by looking at it. These features will directly affect the observables discussed later.

For these reasons, the unperturbed core has been analyzed with a 2D squared detector, positioned in the midplane, with a 500x500 mesh. Figure 3.5 shows the total flux distribution in the core, until the first ring of graphite reflector. In Figure 3.6 the total flux is divided into 5 energy groups, going from low epithermal energies, to very fast fission energies. The choice of the energy intervals is based on the different region of the capture cross section resonances of ^{238}U, plus a subdivision of the fast range, before and after 1 MeV.

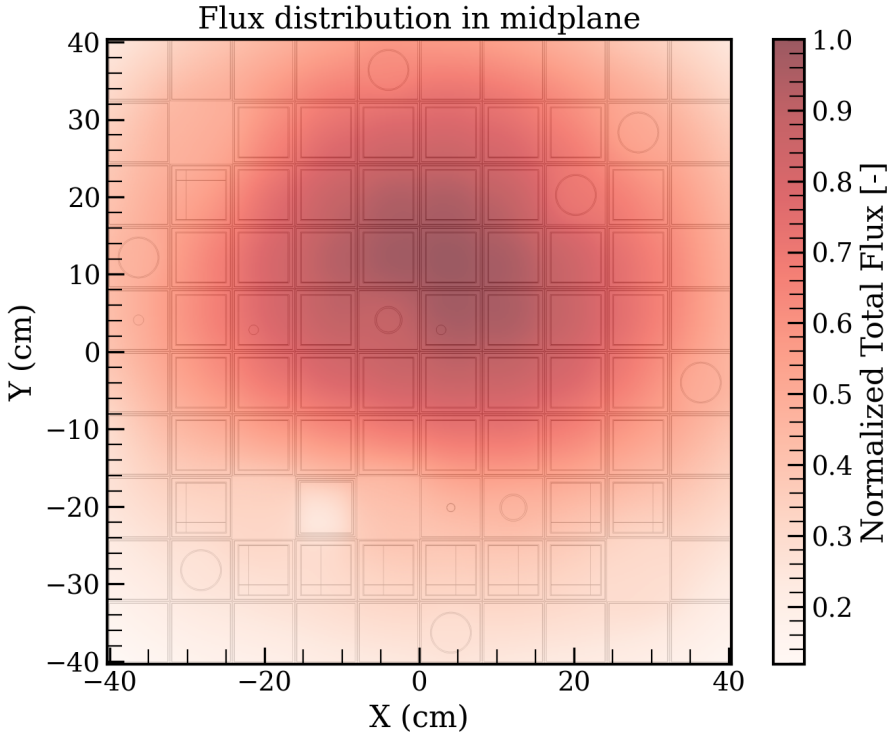


Figure 3.5: Calculated energy-integrated neutron flux spatial distribution in the VENUS-F simplified, critical core model.

As expected, the fuel region exhibits the highest fluxes, with the largest values located one pitch above the center. Conversely, the southern reflector and the control rod region at $(-2, -3)$ present the lowest values.

The energy-breakup highlights that:

- Almost no neutrons reach the slow epithermal range, with the few exceptions located in the graphite reflector region. This is consistent with the absence of a strong moderator.

- Most of the neutron flux is in the energy range between 2×10^4 eV and 1×10^6 eV, with a spatial distribution that resembles the one of the total flux, and a "tail" in the fast fission region ($> 1\times10^6$ eV).

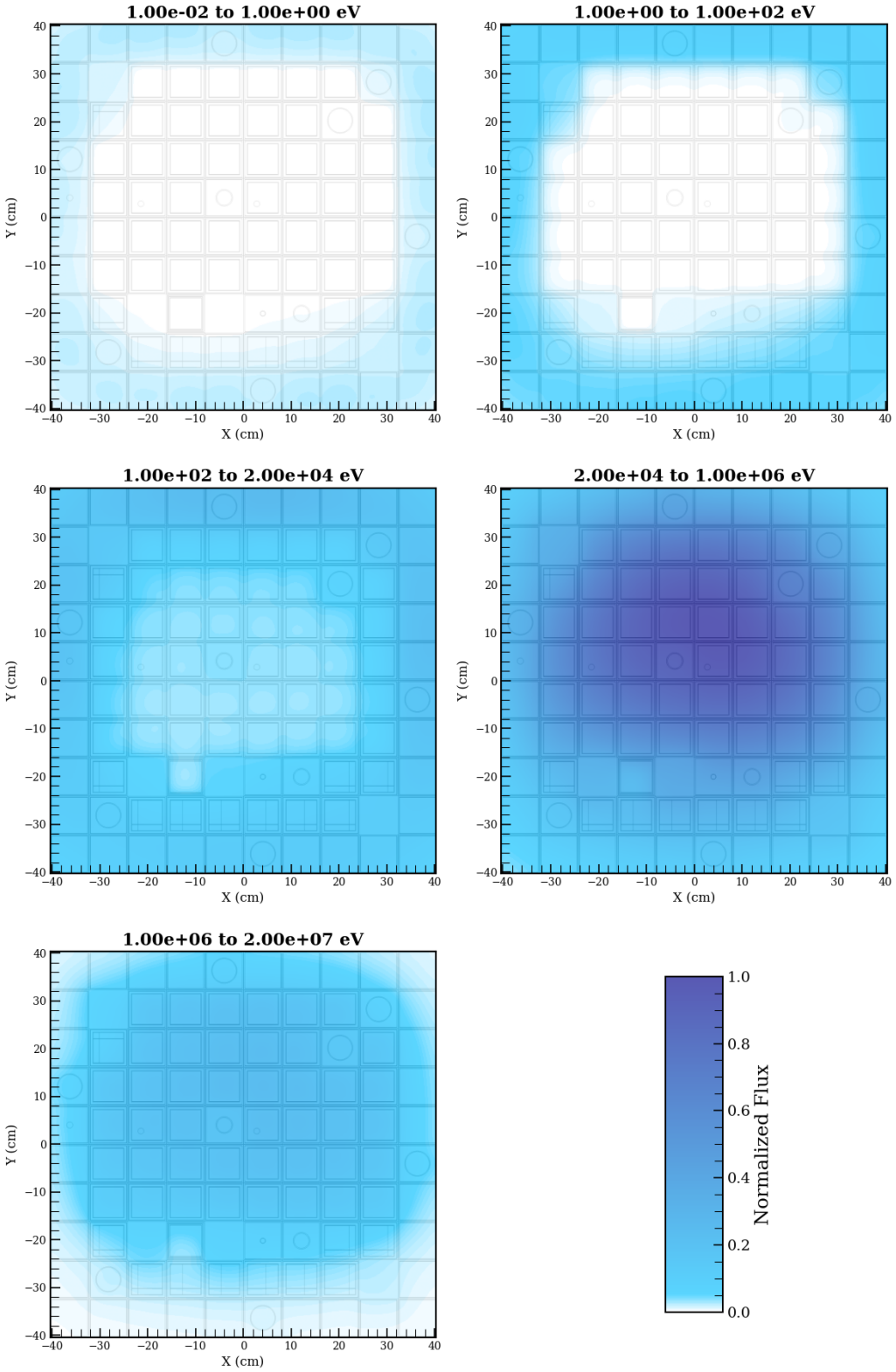


Figure 3.6: VENUS-F simplified, critical core flux for different energy intervals, normalized on the global maximum.

- The relative impact of Doppler broadening on absorption is energy-dependent, being markedly stronger at low energies than at high energies [33]. Thus, a energy interval of significant physical interest is the second, between 1 eV and 1×10^2 eV. Looking at the distribution within these energy values, it is possible to formulate some expectations regarding the temperature effect on reactivity worth in the different locations. In fact, although the core center assembly at $(-1, 1)$ exhibits the highest overall flux, very few neutrons are present in the specific energy range where the Doppler effect is more significant. Instead, locations such as the Graphite Reflector at $(-1, 5)$ or the Core Periphery at $(4, 4)$ feature a relatively higher neutron population in this energy range. Therefore, from this perspective, these two are the most promising locations. Still, in the Core Center, the overall effect of the sample insertion should be significant.

- The Lead Reflector is expected to have a small relevance, since the lead capability to slow down neutron is low (as seen in the flux spectra at low energies) and it is the farthest from the supposed high importance region (active core center).

Table 3.5 reports the energy intervals used. This subdivision will be later considered for further investigations.

Bin	Lower Limit [eV]	Upper Limit [eV]
1	10^{-2}	1
2	1	10^2
3	10^2	$2 \cdot 10^4$
4	$2 \cdot 10^4$	10^6
5	10^6	$2 \cdot 10^7$

Table 3.5: Coarse energy subdivision used for the investigation.

3.3 Temperature adaptation methods

SERPENT2 allows employs ways to define materials at a certain temperature [35]. Two of them (*tmp* and *tms*), presented in Section 2.5, are called by specific options of the *mat* input card. However, direct definition is possible too, using ACE files at the desired temperature, produced out-of-the-box with nuclear data handling tools like SANDY.

These methods have been investigated, over different parameters:

- Computational cost (Memory, time)

- Cosine similarity on the reaction rates

- Integrated reaction rates at different temperatures

During the calculations, an issue emerged with the *tms* method: it supports a maximum of two temperatures at a time. If more are provided, Doppler broadening stops after the second temperature and uses the data at that temperature to all subsequent ones. Consequently, the method was ruled out for current and future use.

The focus is on comparing the remaining two methods under temperature variations. Because these changes primarily affect cross sections, and therefore reaction probabilities, capture reaction rates were chosen as the basis for comparison. The nuclide selected is ^{238}U. The simulations used *tmp* and ACE files for temperatures going from 200 K to 1200 K. Table 3.6 shows the computational costs: as expected, the *tmp* method needs more space, to contain the additional information produced by the Doppler pre-processor, but the difference remains small. Moreover, the two methods are equivalent in running time.

Quantity	**tmp**	**ACE**	**Ratio (ACE / tmp)**
Running Time [min]	2073.25	2064.86	0.996
Memory [MB]	15696.70	14583.84	0.929

Table 3.6: Computational Cost Comparison: *tmp* method vs ACE files

Then, the cosine similarity formula is applied on the reaction rates, at all the temperatures, to investigate their difference. Table 3.7 contains the values for 300 K: once again, practically no difference between the two. Also, other temperatures were investigated, yielding practically equal results.

Location	**Cosine similarity** [%]
Inner Core (-1,1)	99.8
Outer Core (3,3)	99.2
Lead Reflector (2,-3)	99.6
Graphite Reflector (-1,5)	99.9

Table 3.7: ^{238}U capture rates cosine similarity, between ACE and *tmp* method in four experimental locations, at 300 K.

The integrated reaction rates were evaluated at different temperatures. Figure 3.7 shows the values and relative errors (1-σ) for both methods, which exhibit remarkably similar results and trends. In summary, both methods yield highly comparable results and can be selected for future analysis based on situational needs and parameter constraints.

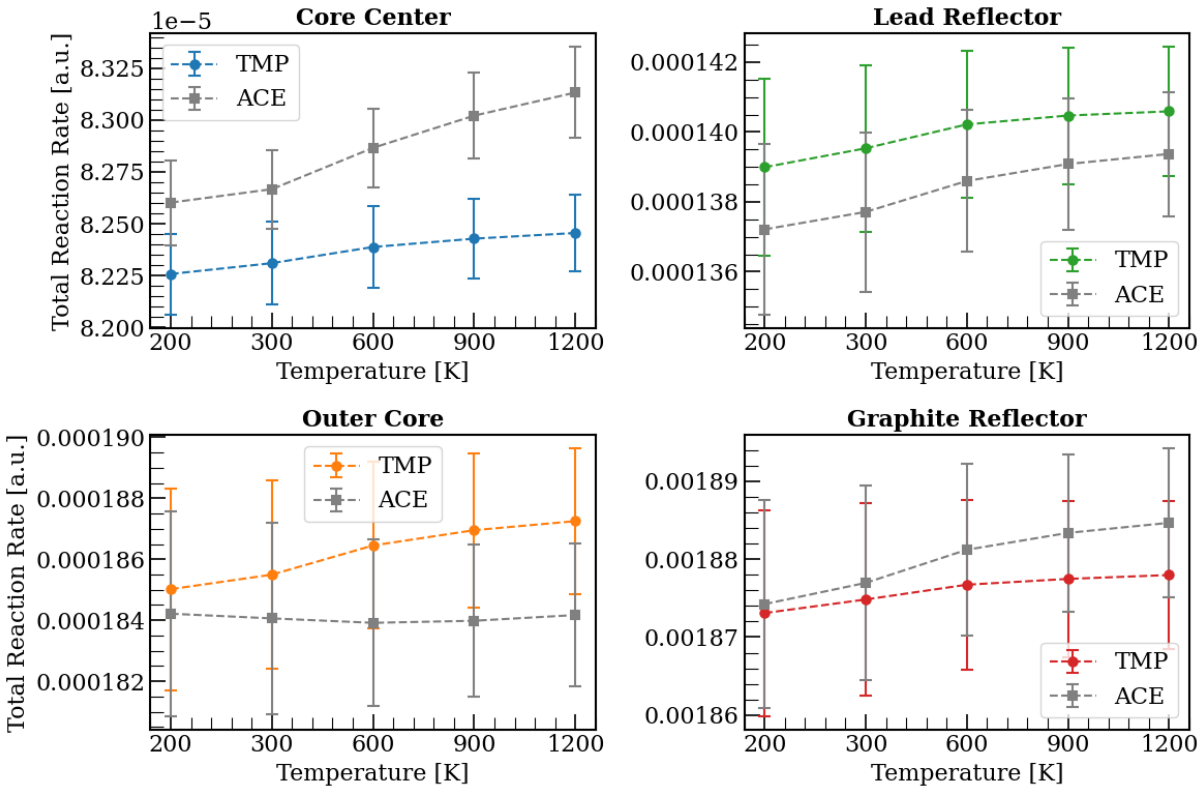


Figure 3.7: Integrated ^{238}U capture rates comparison: ACE vs TMP. Error bars refer to 1-σ.

Chapter 4

Preliminary analysis on Reaction Rates

This chapter focuses on the study of reaction rates as a surrogate for estimating reactivity effects. Reaction rate evaluations have been performed within computational studies and analysis in zero-power reactors for oscillation experiments design [45] and model validation [46]. As seen previously, the reactivity change associated with a small system perturbation can be expressed by first-order perturbation theory, which utilizes the unperturbed neutron importance and flux, the perturbation in the operators, and normalization over the fission source importance (Eq. 2.6). For pure absorption reactivity effects, this expression indicates a proportionality between the change of the sample reactivity worth and the change of reaction rate caused by variation in sample temperature. The temperature modifies the cross section, and neglecting the importance weighting and the phase-space integration, Equation 4.1 is obtained. Therefore, as a preliminary evaluation, the temperature variation of the reaction rates, considering its two main components, the cross section and the flux, serves as a surrogate for the reactivity worth by temperature change.

$$\Delta\rho = \frac{\int \phi^{\dagger}\delta\Sigma\phi}{I_f} \propto \delta\Sigma\phi \tag{4.1}$$

This section focuses on computing ^{238}U capture reaction rates at different temperatures. As highlighted in Sections 1.1 and 1.2, ^{238}U is a key contributor to Doppler reactivity effects in nuclear reactors and yields the largest uncertainty to this parameter [8].

The model developed for the preliminary investigation is very simple: a linear combination, featuring the capture cross section produced with ND processing tools, and VENUS-F neutron spectra, computed in the SERPENT2 full core detailed simulation. The neutron flux is extracted in selected experimental channels inside which the future experimental campaign could take place.

This evaluation will provide insights on the influence of the Doppler broadening on the reaction rates in the four positions. However, it neglects the flux depression phenomenon

that would occur in a real sample. An additional hypothesis concerns the unresolved resonance range: in fact, in this preliminary step, only the average values are considered. The resulting loss of information is considered negligible for the purpose of the study. The analysis also explores cross section extraction by the nuclear data handling tools to better understand their features, while examining potential approaches for computing reaction rates. The work was structured into two main phases:

1. **Cross section production**: They have been reconstructed both in PointWise (PW) and in GroupWise (GW) form, at different temperatures. For the latter, several energy grids and weighting flux choices were considered and analyzed. Particular focus is put on their reconstruction by the nuclear data handling tools.

2. **Reaction rates computation**: The reaction rates are computed by folding the GW cross-sections with the neutron fluxes presented in Section 3.1. An error propagation analysis based on FOP is conducted to examine the correlation between integrated reaction rates across multiple temperatures.

4.1 Cross Section Extraction

The cross sections have been retrieved exploiting the SANDY package and its Python API. SANDY interfaces with NJOY2016 for the interaction with the cross sections in the ENDF6 format, and has dedicated tools for their extraction with different parameters. The procedure exploited functions explained in Section 2.5.2, that call specific modules in NJOY. The function inputs comprised also the argument *err*, that refers to the tolerance used in the reconstruction process: the first computations kept this number quite high (0.25), then it was lowered down to 0.01 (corresponding to a 1% tolerance). Any further reduction would incur unsustainable computational costs without a meaningful gain in accuracy.

JEFF-3.3 [47] nuclear data library is adopted throughout the work.

Reconstruction by NJOY

The `RECONR` module, briefly introduced in Section 2.5, constructs the cross section in the resonance region from the data in the ENDF6 file, producing a Pointwise-ENDF (pendf) file that contains the points of the curves. Outside of the resonance region, the cross section are directly extracted from File 3 of the ENDF6 evaluation. Instead, within the rest of the energy range, resonance parameters from File 2 are added to the background values from File 3, either with a direct adding (this procedure is valid in the resolved region) or after a computation on the statistical distributions given by the file (unresolved region). The final output consists of cross section values on an energy grid optimized for linear interpolation.

Specifically, `RECONR` scans the ENDF6 file twice: first, to establish the energy grid, then, to associate each energy point with the corresponding cross section value. It is done for all the reactions, later constructing the "total" values by direct summation of all the partial contributions.

Generally, in the resonance range, the fundamental data provided regard the energy of the peaks and half-heights. Then, `RECONR` works on parameters that depend on the specific resonance representation (Single-Level Breit-Wigner, Multi-Level Breit-Wigner, Reich-Moore etc) [37]. Each representation has its own general formula, region of application and reconstruction approach. For the unresolved resonance range, if the parameters are not functions of energy, `RECONR` produces the energy grid with 13 points per decade, otherwise it computes the cross section values at their indicated energy magnitude, and then applies linear interpolation in the rest of the energy domain. However, since this last procedure is often found to be inaccurate, `RECONR` can look for large energy gaps and add points in the grid.

4.1.1 PointWise Representation

As explained in Section 2.5, the SANDY function `get_pendf` returns the pointwise file, from which the cross section data is extracted, through the `sandy.Xs.from_endf`. The outcome is a Pandas dataframe with the points in the energy grid and the corresponding values of the cross section. Figure 4.1 shows the capture cross section along the entire energy domain, at three different temperatures. The broadening is clear, the Doppler effect reduces the peaks and thickens the 1200 K curve, as the resonance curves merge with each other. Looking at the cross section change with temperature, the first noticeable feature is that the ratio between the change and the temperature jump causing it tends to diminish with increasing temperatures. Visually, this is highlighted by the blue area that is lost going from 0.1 K to 450 K, which is much larger than the one moving from 450 K to 1200 K, for which the temperature change is almost 1.5 times higher.

The effective reconstruction of the resonances can be explored by focusing on the first few resonances and then comparing their reconstruction with that in the high resonance density region. Figure 4.2 show this, at the three temperatures of the previous graph. In the second subfigure, the energy domain it is 30 times smaller (in lethargy), but contains more peaks. This is due to the energy dependence of resonance widths: as energy increases, individual curves narrow significantly, moving closer and closer to each other.

Moreover, Figure 4.2 shows other characteristics:

- The peaks have always an associated energy value: for each temperature, the maximum value of the resonance is always defined precisely, and it doesn't shift in energy with temperature. In fact, the reconstruction methodology by the `RECONR` module explained before preserves the physics.

- Optimization for linear interpolation: The fine energy grid chosen by NJOY allows for accurate linear interpolation while preserving the resonance profile.

- Resonance overlapping: the Doppler Broadening tends to merge together the curves, increases their smoothness and diminishes the gauges.

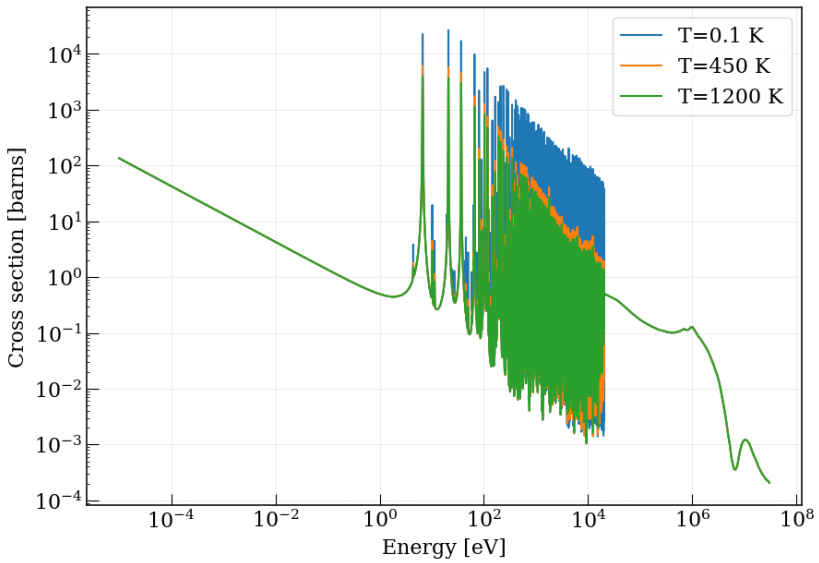


Figure 4.1: PointWise reconstruction of ^{238}U capture cross section, at different temperatures.

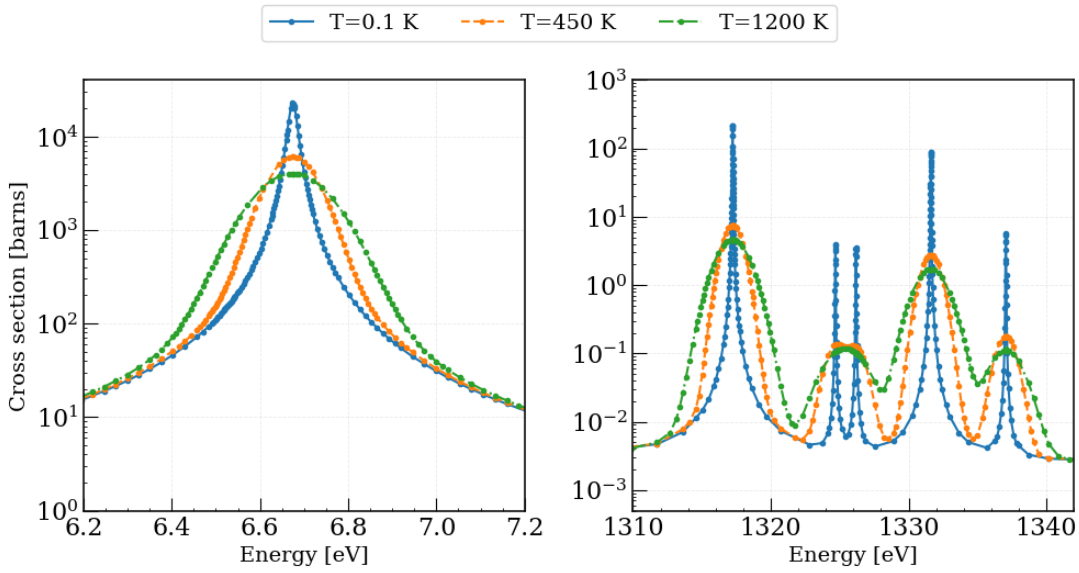


Figure 4.2: PointWise ^{238}U capture cross section in two resonance regions, highlighting the points chosen by NJOY during the reconstruction, for different temperatures.

4.1.2 GroupWise Representation

GroupWise cross sections are widely used in reactor physics, for instance in deterministic codes [48]: a relevant part of the Monte Carlo simulations over the world is launched precisely to define their values [49], [50], [51].

The groupwise representation of a cross section is a weighted integral on each energy bin (Equation 2.20). The weighting function is often a neutron flux in order to preserve integral reaction rates in the energy bin. Default fluxes are available in NJOY and some are tested (homogeneous and a NJOY pre-implemented spectrum typically used for fast reactors) even if low difference is expected. Homogeneous and in-homogeneous energy grids with varying number of groups have also been used. These features have been implemented via the options in the SANDY's function `get_gendf`.

GroupWise cross sections can be directly folded with the neutron fluxes to calculate reaction rates. However, this is an approximated approach that can lead to inaccurate results, particularly in the resonance region, where the resonances may be misrepresented (Figure 4.3). This can be critical for the Doppler effect, and the actual impact remains to be evaluated.

The very high resonances density region can be quite difficult to reproduce by means of the GroupWise representation, even with a large number of groups. This mechanism is shown in Figure 4.3. For a energy discretization uniformly spaced in lethargy, even when using a 2000 groups energy grid, the capability to follow the curves is degrading with increasing energies.

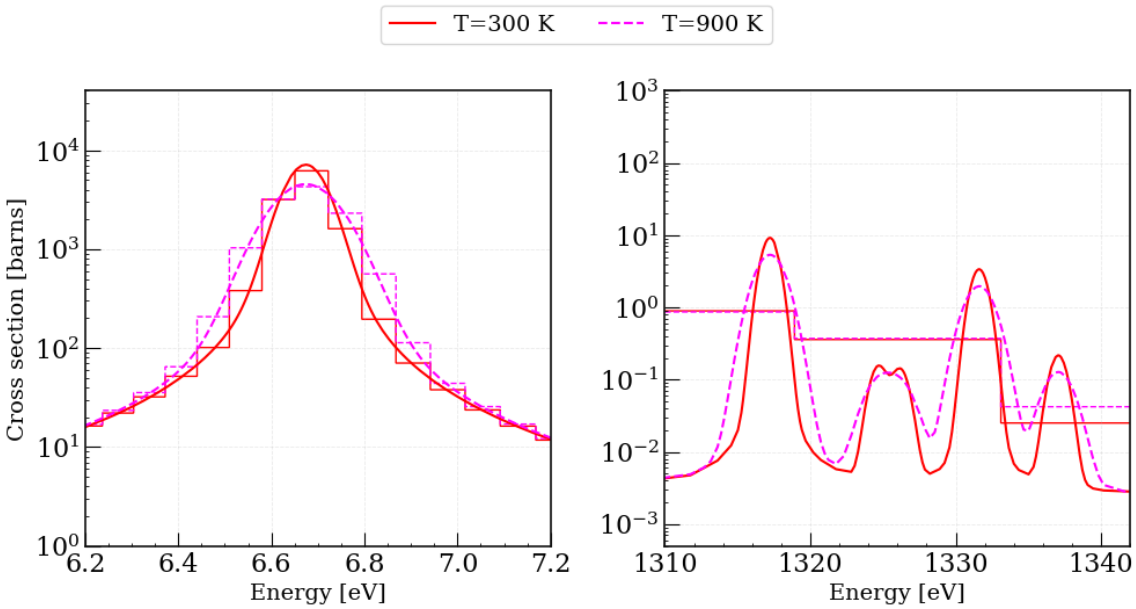


Figure 4.3: PointWise and GroupWise representation of ^{238}U capture cross section inside two resonance regions, at two different temperatures.

Figure 4.4 shows the GroupWise representation of the ^{238}U capture cross section at 900

K as compared to the PointWise (in grey). The discretization error is clear: a large portion of the resonance are averaged out by the GroupWise representation, even using the finest 2000-group grid. This can be explained by the fact that the successive resonance peaks and valleys are so densely spaced that even a high number of groups fails to resolve them, flattening the curves. Although the GroupWise discretization error decreases at higher temperatures, it remains considerable. In conclusion, the discretization by the multi-group approach entails an error that increase with narrower and closely spaced resonances; thus, higher temperatures and lower energies yield better accuracy. Additional analyses are reported in Appendix A.

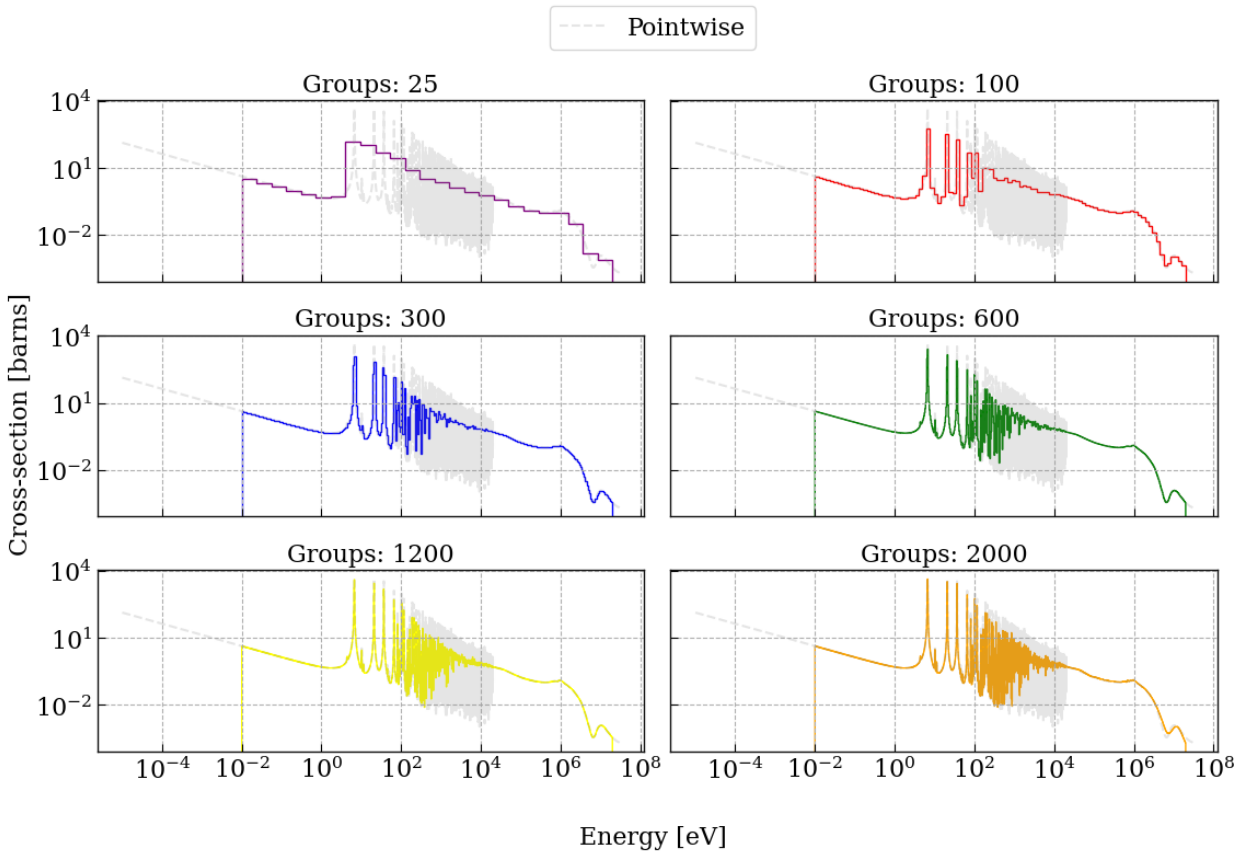


Figure 4.4: GroupWise ^{238}U capture cross section, on several grids, overlaid upon the PointWise representation, all at 900 K

4.2 Multi-group Reaction Rates in VENUS-F

Reaction rates are defined by the integration of the energy-dependent neutron flux $\phi(E)$ and the macroscopic cross section $\Sigma(E,T)$:

$$R(T) = \int \Sigma(E,T)\phi(E)\,\mathrm{d}E. \tag{4.2}$$

The discrete version of this expression is the linear combination to produce groupwise reaction rate distribution ($\vec{r}(E,T)$), which are subsequently summed to obtain the integrated value ($R(T)$, sometime referred to as "total reaction rates").

$$\vec{r}(E,T) = \vec{\Sigma}(E,T) \cdot \vec{\phi}(E) \tag{4.3}$$

$$R(T) = \sum_{g=1}^{G} \Sigma_g(T) \cdot \phi_g = \sum_{g=1}^{G} r_g \tag{4.4}$$

It is worth emphasizing that these calculations concern the ^{238}U capture cross-section for a sample placed in the previously described experimental channels. For this analysis, the finest energy grid chosen for tallying the neutron flux in the detailed VENUS-F model (Section 3.1), comprising 2000 energy groups spanning from 10^{-2} eV to 2×10^{8} eV, was used.

4.2.1 Energy-dependent and -integrated reaction rate results

Tables 4.1, 4.2, 4.3, 4.4 report the integrated values for the all the locations, normalized to the 300 K reference on the finest grid.

The most significant integrated reaction rate difference occurs between the Core Center and the Graphite Reflector, where it exceeds an order of magnitude. This gap is justified by the characteristics of the neutron flux spectrum in the two locations, in particular the presence of a strong epithermal tail in the reflector. In fact, at epithermal energies, the ^{238}U capture cross section is larger than at fast energies and exhibits higher resonance peaks, thereby producing higher reaction rates.

Moreover, while the integrated values for coarser grids are predominantly underestimated by a few per cent, some instances show an overestimation. However, this difference is marginal.

Most notably, the reaction rate variations due to temperature changes remain very small, with discrepancies generally below 1%. Uncertainties are not reported, since they require further investigation. In fact, all reaction rates and their respective uncertainty estimates originate from the same flux distribution and are thus statistically dependent. Furthermore, the four regions respond differently to temperature variations.

	Number of groups			
T [K]	Reference	300	600	1200
200	8.608×10^{-5}	0.9714	0.9779	0.9677
300	8.613×10^{-5}	0.9710	0.9772	0.9671
900	8.625×10^{-5}	0.9701	0.9757	0.9663
1200	8.628×10^{-5}	0.9699	0.9753	0.9662

Table 4.1: Total reaction rate in Core Center at several temperatures, normalized per temperature on the reference. Its value is explicitly given. Reference grid has 2000 groups.

	Number of groups			
T [K]	Reference	300	600	1200
200	1.787×10^{-3}	0.9670	0.9877	0.9821
300	1.783×10^{-3}	0.9697	0.9893	0.9832
900	1.770×10^{-3}	0.9780	0.9938	0.9887
1200	1.767×10^{-3}	0.9802	0.9943	0.9892

Table 4.2: Total reaction rate in Graphite Reflector at several temperatures, normalized per temperature on the reference. Its value is explicitly given. Reference grid has 2000 groups.

	Number of groups			
T [K]	Reference	300	600	1200
300	1.9430×10^{-4}	1.0576	1.0333	0.9881
900	1.9519×10^{-4}	1.0521	1.0277	0.9969
1200	1.9593×10^{-4}	1.0479	1.0237	0.9971

Table 4.3: Total reaction rate in Outer Core at several temperatures, normalized per temperature on the reference. Its value is explicitly given. Reference grid has 2000 groups.

	Number of groups			
T [K]	Reference	300	600	1200
300	1.3517×10^{-4}	0.9867	0.9659	1.0274
900	1.3679×10^{-4}	0.9795	0.9619	1.0111
1200	1.3681×10^{-4}	0.9803	0.9636	1.0085

Table 4.4: Total reaction rate in Lead Reflector at several temperatures, normalized per temperature on the reference. Its value is explicitly given. Reference grid has 2000 groups.

The energy-dependent reaction rate are showed in Figure 4.5. Three observations on them can be made:

1. As a consequence of the better representation of the low energy resonances showed in Figure 4.4, the resonances effect on the reaction rates is more visible in the epithermal part of the energy spectrum, while it is less evident at higher energies. The epithermal tail of the flux spectrum allows, in the regions where it is high enough, to catch the resonance effect on the reaction rate.

2. On a side note, the numerical oscillations in the sparsely populated region could strongly affect the precision of the computation. This must be kept in mind in the discussion of the results.

3. The temperature effect in the energy-dependent reaction rate is minimal, not observable from Figure 4.5. Yet, it is present and can have an impact. In fact, looking at the first resonance, variations in the order of tens of percentages can be found. This is illustrated in Figure 4.6, which focuses on the first resonance at 6.7 eV. As the temperature increases from 300 K to 900 K, the reaction rate in the bins around it changes by tens of percentage points. This is in accordance to the Doppler Index results obtained by Andoh et al. [15], presented in Section 1.2, which also shows a large peak around 6.7 eV.

Finally, the calculated reaction rates can be used to identify the energy domains that dominate reactivity. To this end, the cumulative reaction rates across energy were evaluated at various temperatures, as shown in Figure 4.7. The curves highlight a very important aspect, which will be key in explaining many of the subsequent results in this study: the first three to four resonances account for roughly 80% of the overall capture rate. Therefore, neutrons within this energy interval (5-100 eV) have a decisive impact on the Doppler reactivity coefficient.

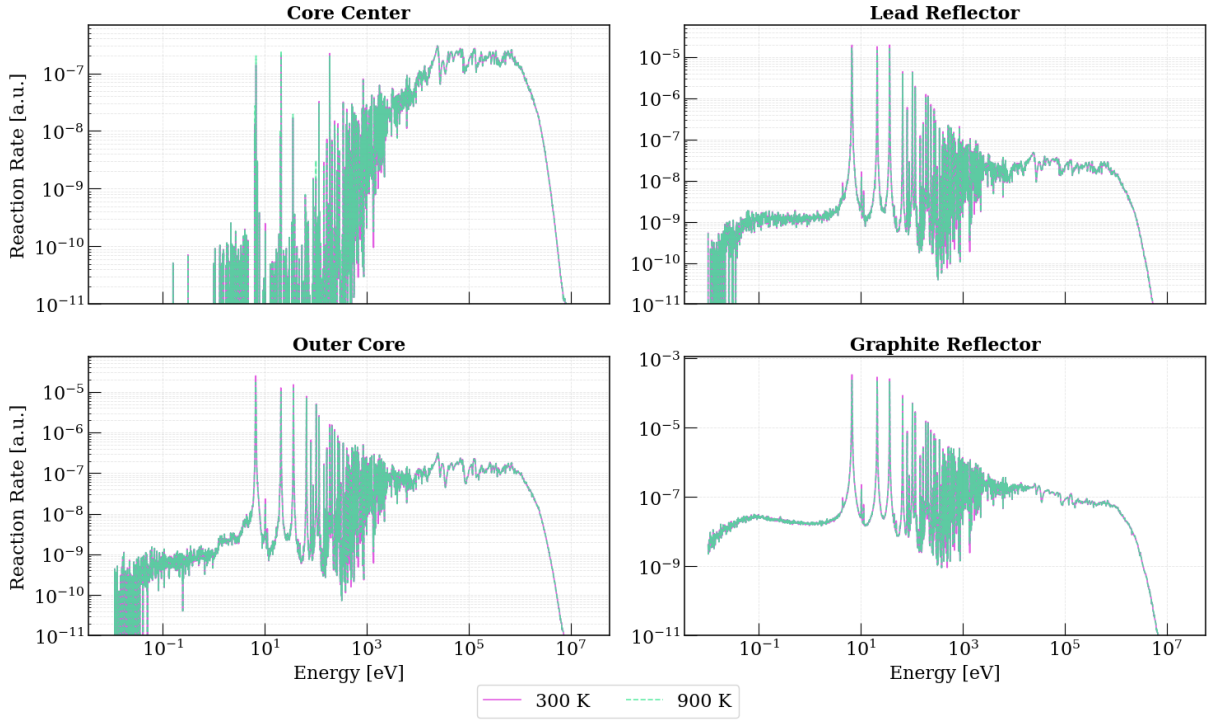


Figure 4.5: ^{238}U capture rate distribution, in all experimental locations, at 300 K and 900 K, for the finest grid (2000 groups).

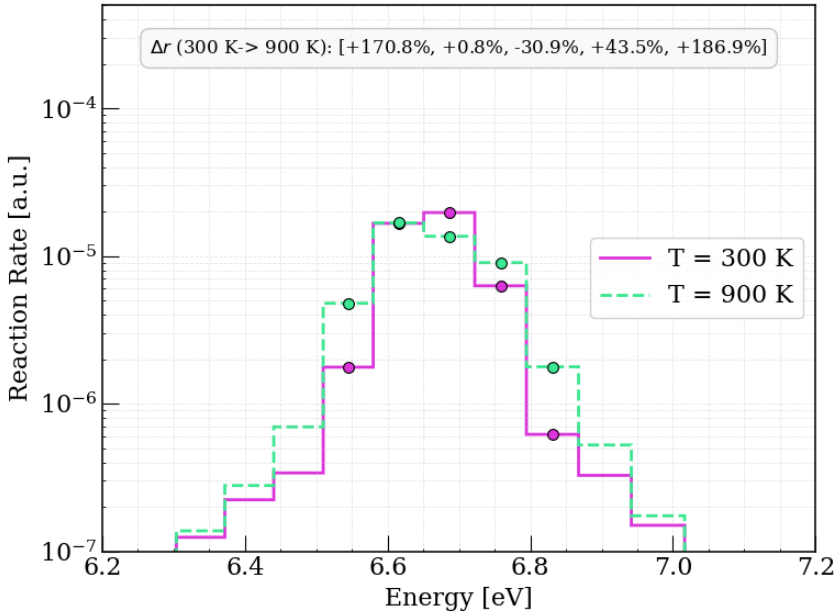


Figure 4.6: ^{238}U capture rate variation in the first resonance, in the Lead Reflector, for a temperature jump between 300 K and 900 K. The box reports the exact values, of the highlighted point, from left to right

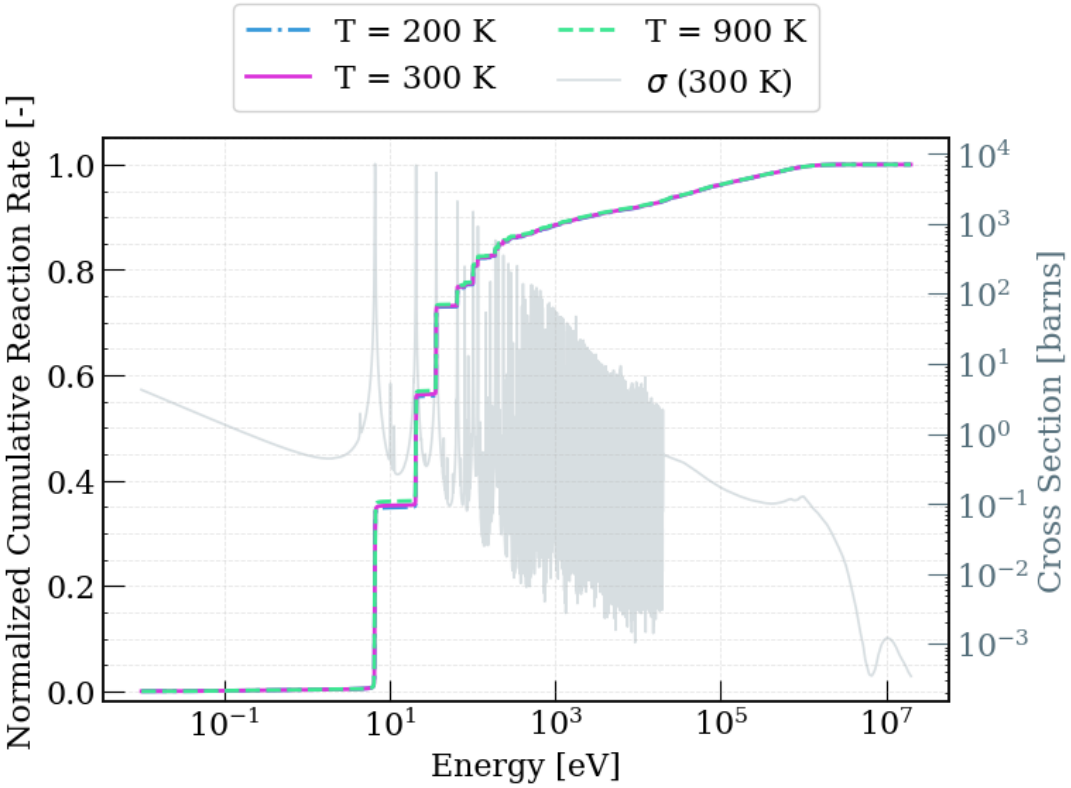


Figure 4.7: ^{238}U capture rate cumulative, in the Lead Reflector, for three different temperatures, normalized to the maximum. The capture cross section is shown in grey in the background.

4.2.2 Reaction Rate variation by temperature change

Hypotheses and Methods

The final aim of the computations is to investigate the temperature effect on the reaction rates. Given the small magnitude of the temperature-induced variations reported in the previous section, robust uncertainty quantification of these changes is essential to distinguish physical variations from random noise. Thanks to the appropriate choice of the model, based on the subdivision in energy groups of the cross section and flux, FOP-based uncertainty propagation can be performed. The correlation that exist between the total reaction rates at different temperature, since they have been computed using the same flux, must be considered.

The following assumptions are made:

- **Linear model**: Both the reaction rate values and their change on temperature are computed employing a linear combination of cross section and flux.
- **Fluxes independence**: The correlations between energy bins of the same neutron

flux are neglected. Therefore, only the stochastic uncertainty of the group fluxes will be propagated.

- **No Nuclear Data uncertainty**: The cross sections are treated as coefficients of the linear combination. $Var[\sigma^c(E)] = 0, \quad \forall E$

The uncertainties associated to the flux are contained in its covariance matrix, that according to the second assumption, is diagonal.

$$\widetilde{C_\phi} = \begin{pmatrix} u^2_{\phi_1} & 0 & \cdots & 0 \\ 0 & u^2_{\phi_2} & \cdots & 0 \\ \vdots & \vdots & \ddots & \vdots \\ 0 & 0 & \cdots & u^2_{\phi_G} \end{pmatrix} \tag{4.5}$$

For the reaction rate energy distribution computation, expressed in Equation 2.10, the sensitivity coefficients of the model are the cross sections. Consequently, the uncertainty in each energy group is the product of the neutron flux uncertainty and the value of the GroupWise cross section in that group. This procedure is exactly equal to applying directly the FOP formula for the standard deviation on the model, in each energy bin [52]:

$$u_f = \sqrt{\left(\frac{\partial f}{\partial x}\right)^2 u_x^2 + \left(\frac{\partial f}{\partial y}\right)^2 u_y^2 + \left(\frac{\partial f}{\partial z}\right)^2 u_z^2 + \cdots} \tag{4.6}$$

Instead, the model of the integrated reaction rate temperature change can be expressed by Equation 4.7:

$$\Delta R_{T_1,T_2} = \sum_{i=g}^{G} \phi_g(\Sigma_{g,T_2} - \Sigma_{g,1}). \tag{4.7}$$

Considering the equation, if the covariance matrix of the integrated reaction rates at different temperatures is known, the computation of the single uncertainty value for a specific temperature jump is straightforward:

$$u_{\Delta R_{T_1,T_2}} = \sqrt{u^2_{R_{T_1}} + u^2_{R_{T_2}} - 2 \cdot u_{R_{T_1},R_{T_2}}} \tag{4.8}$$

Consequently, the covariance matrix must be produced.

To do so, one can consider the integrated reaction rate computation at different temperatures as a linear combination between a matrix of coefficients (the cross sections in the energy bins and at several temperatures) and the energy-dependent neutron flux array, yielding the vector of energy-integrated reaction rates at different temperatures (Equation 4.9).

$$\begin{pmatrix} \Sigma_1^{T_1} & \Sigma_2^{T_1} & \dots & \Sigma_G^{T_1} \\ \Sigma_1^{T_2} & \Sigma_2^{T_2} & \dots & \Sigma_G^{T_2} \\ \vdots & \vdots & \ddots & \vdots \\ \Sigma_1^{T_n} & \Sigma_2^{T_n} & \dots & \Sigma_G^{T_n} \end{pmatrix} \begin{pmatrix} \phi_1 \\ \phi_2 \\ \vdots \\ \phi_G \end{pmatrix} = \begin{pmatrix} R^{T_1} \\ R^{T_2} \\ \vdots \\ R^{T_n} \end{pmatrix} \tag{4.9}$$

The associated covariance matrix for such quantity can be directly derived applying the sandwich formula [52]:

$$\widetilde{C_R} = \widetilde{\Sigma} \cdot \widetilde{C_\phi} \cdot \widetilde{\Sigma}^T = \begin{pmatrix} u_{T_1,T_1} & u_{T_1,T_2} & \dots & u_{T_1,T_n} \\ u_{T_2,T_1} & u_{T_2,T_2} & \dots & u_{T_2,T_n} \\ \vdots & \vdots & \ddots & \vdots \\ u_{T_n,T_1} & u_{T_n,T_2} & \dots & u_{T_n,T_n} \end{pmatrix} \tag{4.10}$$

The computed covariance matrix is used to quantify the uncertainty on $\Delta R(T_1 \rightarrow T_2)$ for every pair of temperatures in a correlated fashion [53], through Equation 4.8.

The correlation matrix ($\widetilde{P_{\Delta R}}$) is computed, applying Equation 4.11 [54] (where $\widetilde{U}$ is the diagonal matrix of the standard deviations for all the reaction rates at the different temperatures), and showed in Figure 4.8.

$$\widetilde{P_{\Delta R}} = \widetilde{U}^{-1} \widetilde{C_R} \widetilde{U}^{-1} \tag{4.11}$$

An additional interesting data to produce is the error on the relative change (in %) of the integrated reaction rate due to temperature, with the latter computed as:

$$\Delta R_{rel}[\%] = 100 \frac{R_2 - R_1}{R_1} = 100 \frac{R_2 - R_1}{R_1} \frac{\frac{1}{R_1}}{\frac{1}{R_1}} = 100 * \frac{\frac{R_2}{R_1} - 1}{1} \tag{4.12}$$

where 1,2 indicate the two different temperatures. Its uncertainty is directly proportional to the one on the ratio between R_2 and R_1, and can be calculated as reported in Equation 4.13. This completes the picture on reaction rate variation by temperature change.

$$u_{\Delta_{R_{rel}}} = \sqrt{100^2 \frac{R_2^2}{R_1^4} u_{R_1}^2 + \frac{100^2}{R_1^2} u_{R_2}^2 - 20000 \frac{R_2}{R_1^3} u_{R_1,R_2}} \tag{4.13}$$

Results

Because the same neutron flux spectrum is used to evaluate reaction rates across different temperatures, a strong positive correlation is expected when calculating reaction-rate changes. In fact, any perturbation in the cross section shifts the reaction rate response in the same direction across all investigated temperatures. As shown in Figure 4.8, the correlation between the reaction rates is always larger than 0.93. Additionally, since reaction rate variations are driven exclusively by temperature-induced cross section changes, a larger temperature jump presents a lower correlation.

Figure 4.9 shows the integrated reaction rates at different temperature, together with their relative variation due to temperature change, across the four experimental locations. The starting temperature is always 300 K, then the sample gets both cooled down to 200 K and heated up to 900 K. As expected, the strong negative correlation helped in reducing the uncertainties on the temperature-driven change compared to those on the integrated

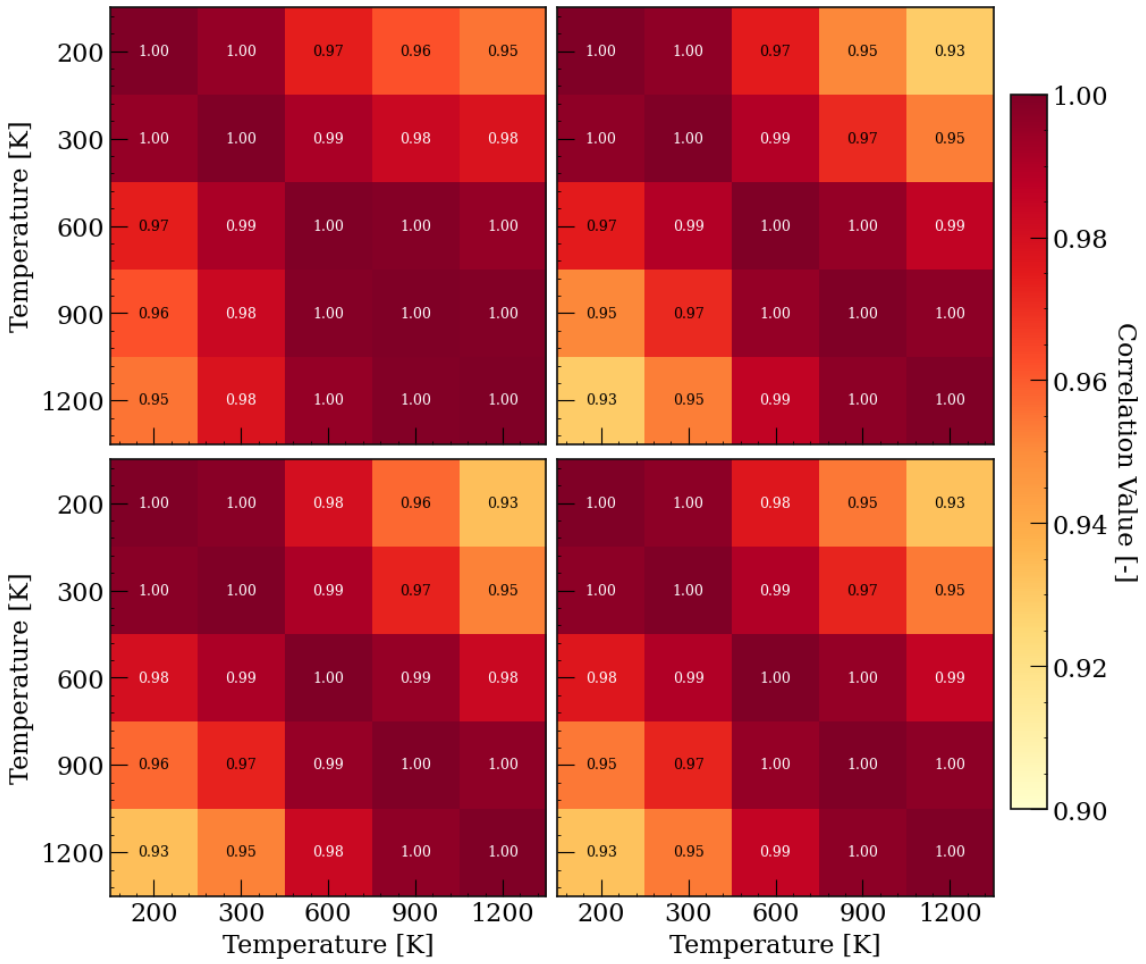


Figure 4.8: Correlation matrices on the total reaction rates at different temperatures, in all experimental locations under analysis. Top-left: Core Center, top-right: Lead Reflector, bottom-left: Outer Core, bottom-right: Graphite Reflector.

reaction rates. In all the regions, there was a strong decrease of the associated uncertainty, about one order of magnitude.

The Core Center presents both the lowest absolute values and the smallest relative change, around 0.1%. As explained before, this is due to the fast neutron flux spectrum (Figure 3.1), where there are few interactions in the low energy resonances, the most important for Doppler. On the other hand, the relative variation of the reaction rates in the Lead Reflector, where the epithermal tail is quite strong, is of the order of 1% for both temperature changes. Also the absolute values are larger. Yet, both locations present behaviors that recall the general consequences of the Doppler effect. The capture rate shows a positive trend with temperature, increasing and decreasing accordingly.

In the Outer Core, the absolute values are larger than in the Core Center, thanks to the effect of the epithermail tail. However, the uncertainties dominate over the variation, and

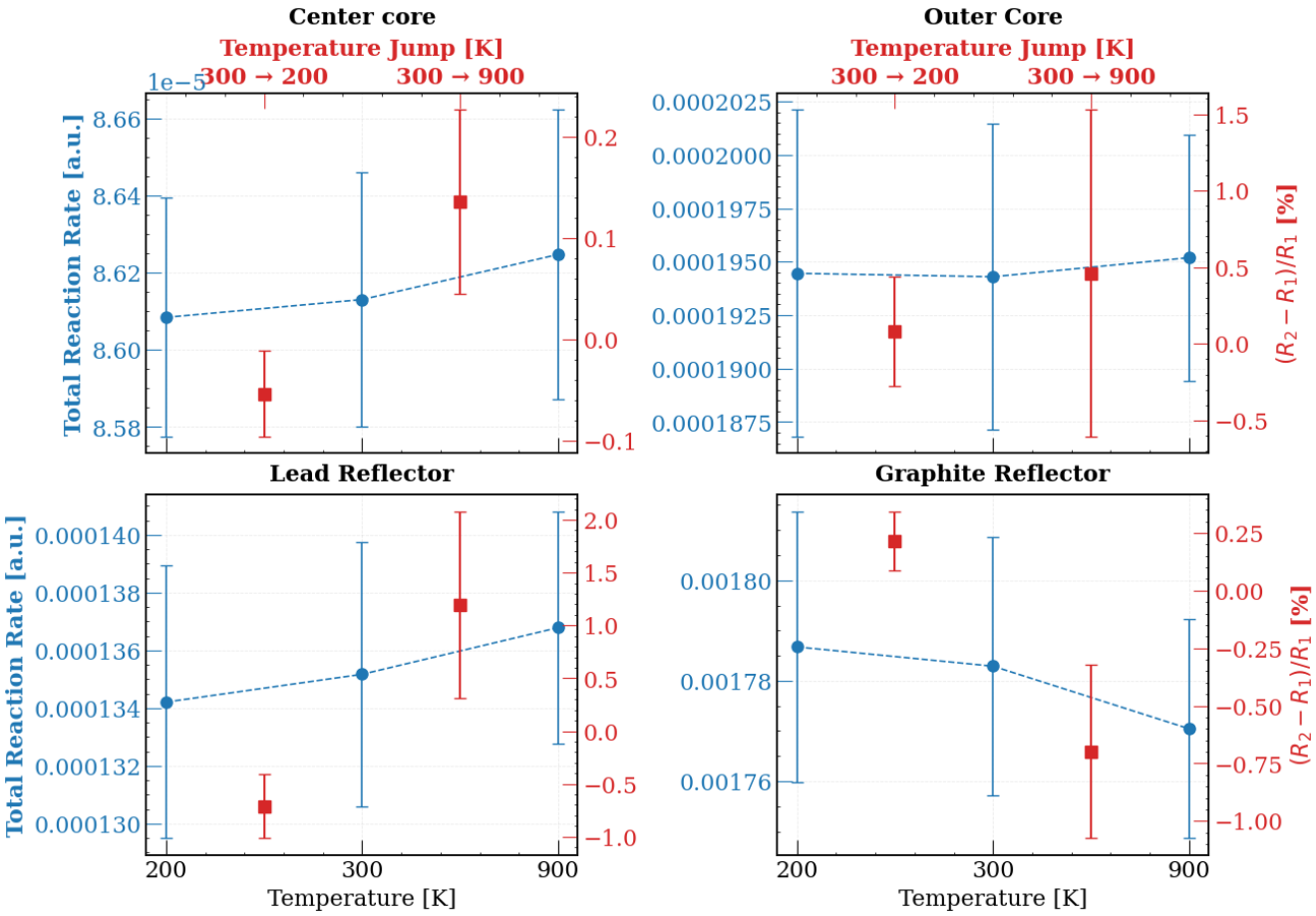


Figure 4.9: Integral ^{238}U capture rates and their relative percentage variations. Absolute values at the corresponding temperatures are shown in blue (left axis), while relative changes, in percentage, with respect to the 300 K reference value are shown in red (right axis). Errorbars refer to 1-σ.

the temperature effect is not significative. The absolute values are largest in the Graphite Reflector, consistent with its strong epithermal tail. On the other hand, relative variations are below 1%, and a strange behavior is detected: their response to temperature change is opposite.

Nonetheless, in all the analyzed locations, the absolute temperature-driven variations are minimal, within 1 or 2-σ.

In conclusion, Table 4.5 briefly presents the pros and cons of the reaction-rate-based approach, reviewing the key considerations discussed in this chapter.

Strengths	**Limitations**
Value comparison: Possibility to compare numerical values across different cases.	**Uncertainty dominance:** MC uncertainties can dominate the overall results.
Doppler effect hints: Potential to capture initial Doppler broadening effects.	**Unreliability of absolute values:** Absolute numerical results may lack direct physical reliability.
Energy-dependent features: Identification and mapping of reaction rate characteristics across energy.	

Table 4.5: Pros and cons of the reaction-rate-based approach.

Chapter 5

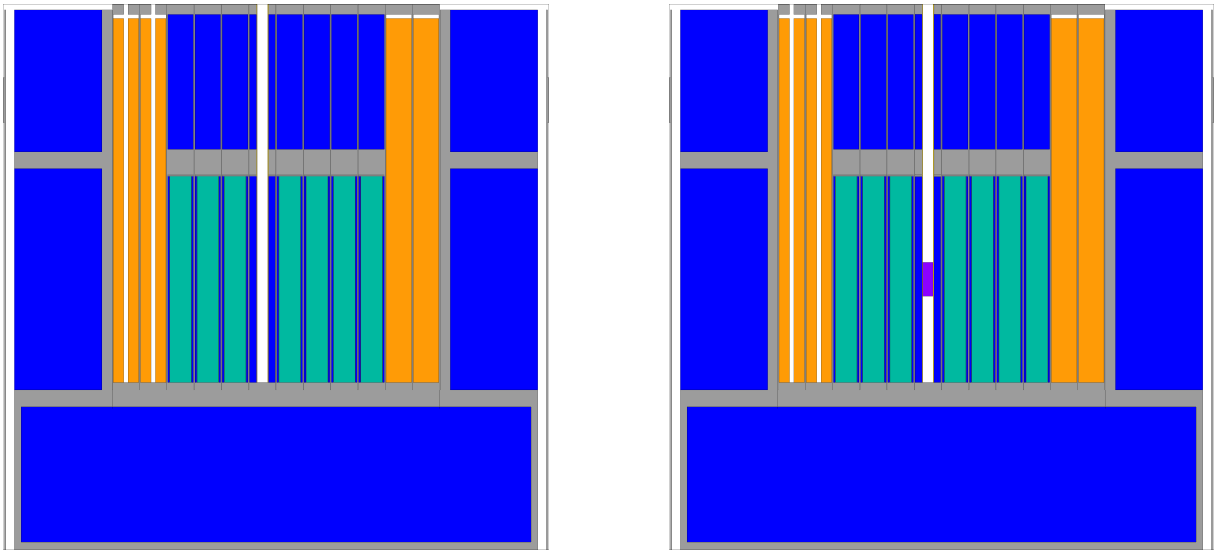
^{238}U reactivity worth calculations

This chapter focuses on the calculation of the reactivity worth of a ^{238}U sample at different temperatures across different VENUS-F core locations. The effect of modified sample geometry is also investigated. The computation methodology, based on the random sampling approach, is detailed in Section 2.2.2, and 250 replicas are used. This value was found to be a good trade-off between statistical accuracy and computational cost. Moreover, the statistical independence test implementing the linear error propagation procedure (Section 2.3) is applied. Finally, the minimum target reactivity worth is about 1 pcm, due to the uncertainty of the reactivity measuring experimental method implemented in VENUS-F, detailed in Section 1.3.

5.1 Sample insertion

The reactivity worth of small samples inserted in the selected experimental channels is calculated. In the simulations, this is modeled by placing a sample at the given temperature inside the specific channel. Due to the model complexity, this modification has been implemented exploiting the modular structure of the input file. A copy of the actual experimental channel assembly was created, filled with the sample, and substituted in the core lattice. Figure 5.1 compares the vertical layouts, with the sample in the Core Center experimental assembly.

The sample diameter was fixed at 3 cm, roughly the maximum width feasible in the experimental setup, while two lengths were considered: 10 cm (standard) and 30 cm (long). The longer sample was considered to assess how strongly the sample length influences the resulting $\Delta\rho$, given the low expected Doppler effect. The material density was 19.10 g/cm^3. All the locations listed in Table 3.1 are investigated.



(a) Unperturbed core **(b)** Core with sample in Core Center

Figure 5.1: VENUS-F core vertical layout: perturbed and unperturbed configuration

5.2 ^{238}U sample reactivity worth at room temperature

The analysis starts investigating the reactivity worth of a ^{238}U sample at room temperature (300 K). This immediately allows excluding experimental locations where the reactivity worth is too small, which would result in negligible temperature-induced reactivity changes. The $\Delta\rho$ comparison with longer sample (30 cm) is tested in the remaining experimental locations.

The replicas were checked in terms of normality and convergence for all the combinations. Table 5.1 shows the results, while Figure 5.2 the convergence, for the sample inside the Graphite Reflector experimental channel. The $\Delta\rho$ distributions presented a standard deviation around 10-12 pcm, that, considering 250 replicas, yielded a statistical uncertainty of 0.6-0.7 pcm. Although they are relatively high, further uncertainty reduction would be computationally prohibitive and physically hardly justifiable, since the nuclear data uncertainties have not been considered. The additional methodology for uncertainty estimation, reported in Section 2.3 has been applied, checking the correspondence with the stochastic error. The two curves are practically equal, as shown in the middle plot on the right in Figure 5.2.

The sample reactivity worth is consistently negative across core locations, highlighting that the ^{238}U capture effect prevails over fission, even in the Core Center, where the neutron spectrum is fast. The sample reactivity worth varies between -1 and -27 pcm depending on the core location. In the Lead Reflector and Outer Core, the values remain between -1 and -2 pcm; these locations were deemed unviable for further study, as any temperature-driven reactivity change would be smaller than the achievable calculation precision (and probably even measurement precision).

Location	^{238}U Sample Reactivity Worth [pcm]		
	Height: 10 cm	**Height: 30 cm**	**Ratio (30 cm/10 cm)**
Core Center	−13.8±0.7	−37.8±0.7	2.7
Core Periphery	−7.9±0.6	−28.2±0.6	3.5
Graphite Reflector	−26.9±0.7	−68.3±0.7	2.5
Lead Reflector	−2.2±0.7	–	–
Outer Core	−1.2±0.7	–	–

Table 5.1: Summary table of $\Delta\rho$ by room temperature ^{238}U samples with different lengths and their ratios.

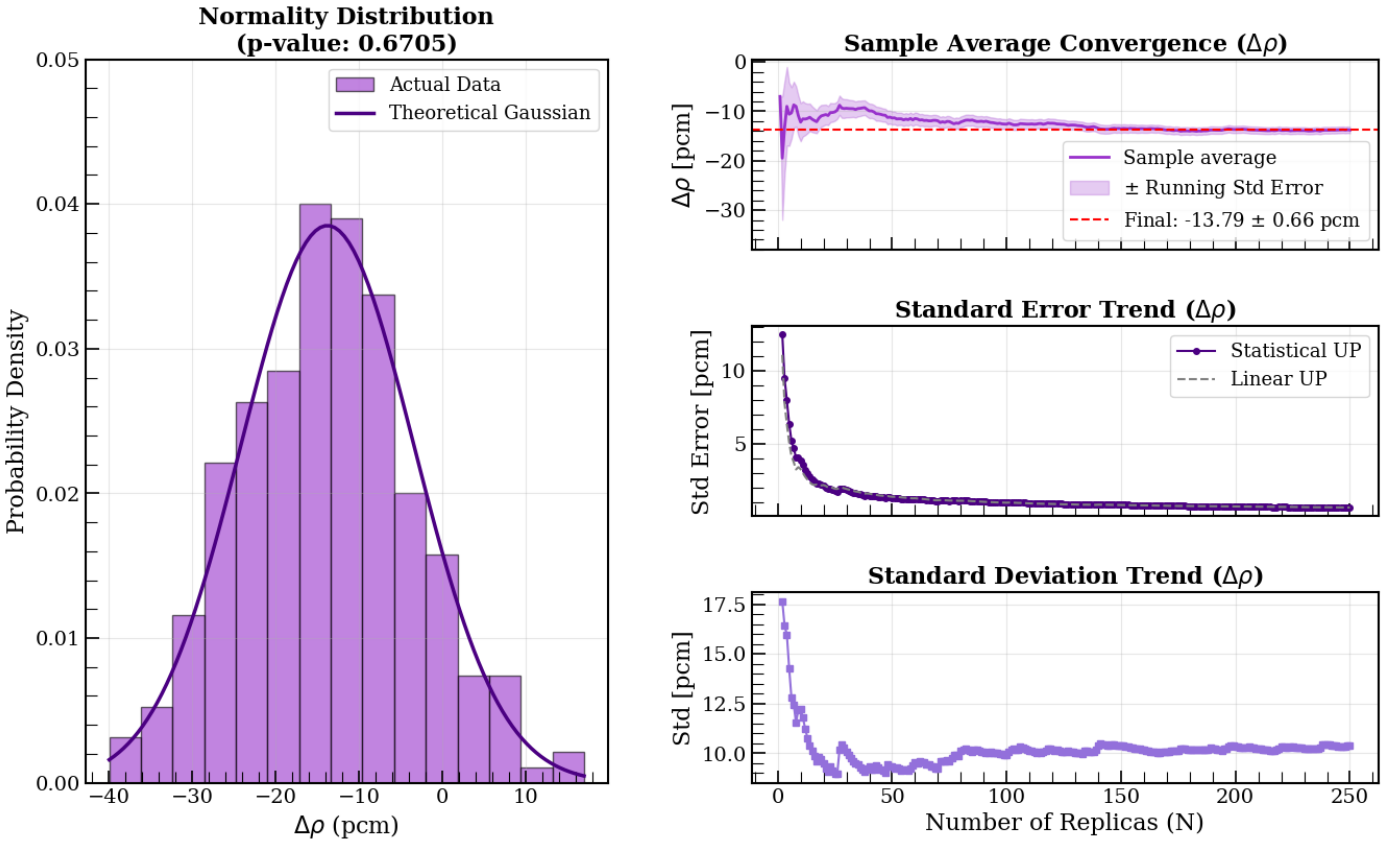


Figure 5.2: Convergence study of $\Delta\rho$ replicas for 300 K ^{238}U sample in the Graphite Reflector experimental assembly. p-value > 0.05 indicates normality.

There is a relevant difference between Core Periphery and Outer Core, although the two assemblies are very close ((4,4) vs (3,3)). The Outer Core assembly is manly surrounded

by fuel, the neutron spectrum is therefore faster. On the contrary, the spectrum is slower in location (4,4) due to the epithermalization by the graphite. The competition between capture and fission is affected by this aspect, causing the differences in the results. Indeed, for ^{238}U, a softer neutron spectrum directly increases the capture rate.

The reactivity worth values for Graphite Reflector and Core Center in Table 5.1 show a phenomenon that is not immediately obvious. Indeed, the sample perturbation is greater in the reflector than in the center, even if the total flux is much lower (see Section 3.2.3). A qualitative explanation can be given by analyzing the flux spectra in those experimental assemblies and the reaction rates (in particular capture and fission) inside the samples.

First, it is instructive to examine the ^{238}U fission and capture cross sections , depicted in Figure 5.3. The capture cross section dominates the majority of the domain, and only around 1 MeV the probability of fission becomes relevant. Therefore, since the net effect on core reactivity stems from the interplay of these two competing phenomena (to a first approximation), the reaction rate distribution in energy can give an indication on which of the two is winning, weighting the probability of a specific interaction (cross section) on the flux. As presented in Section 3.1, the flux at the two locations differs in spectral hardness and the presence of an epithermal tail.

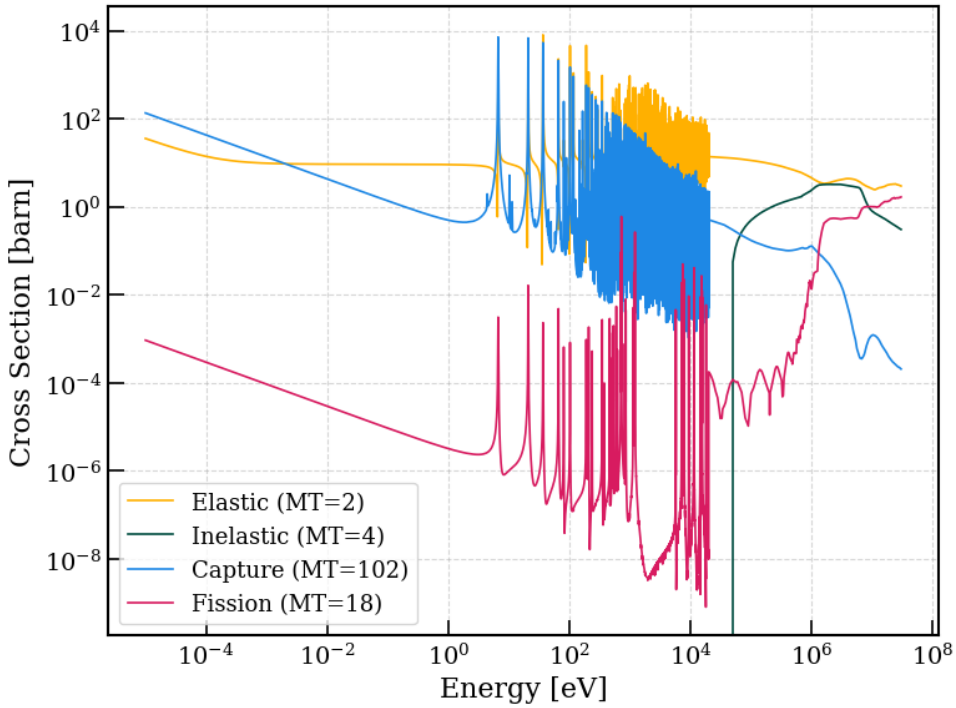


Figure 5.3: ^{238}U capture, fission, elastic and inelastic scattering cross sections.

The reaction rates in the sample are now compared (Figure 5.4). On the one hand, in the Graphite Reflector assembly, epithermalization by carbon enhances the negative contribution from capture (increasing the total capture rate by a factor of 1.8). On the other hand, in the Core Center, the much harder neutron spectrum strongly amplifies

the effect of fission reactions, increasing the total fission rate by a factor of 2.16. Thus, the largest difference between the locations is in the fission rate. The ratios between the energy-integrated reaction rates is reported in Table 5.2. Despite these results on reaction rates are not fully transposable on a reactivity worth analysis, they provide valuable qualitative information. In general, the greater the imbalance towards capture, the higher the (negative) reactivity worth.

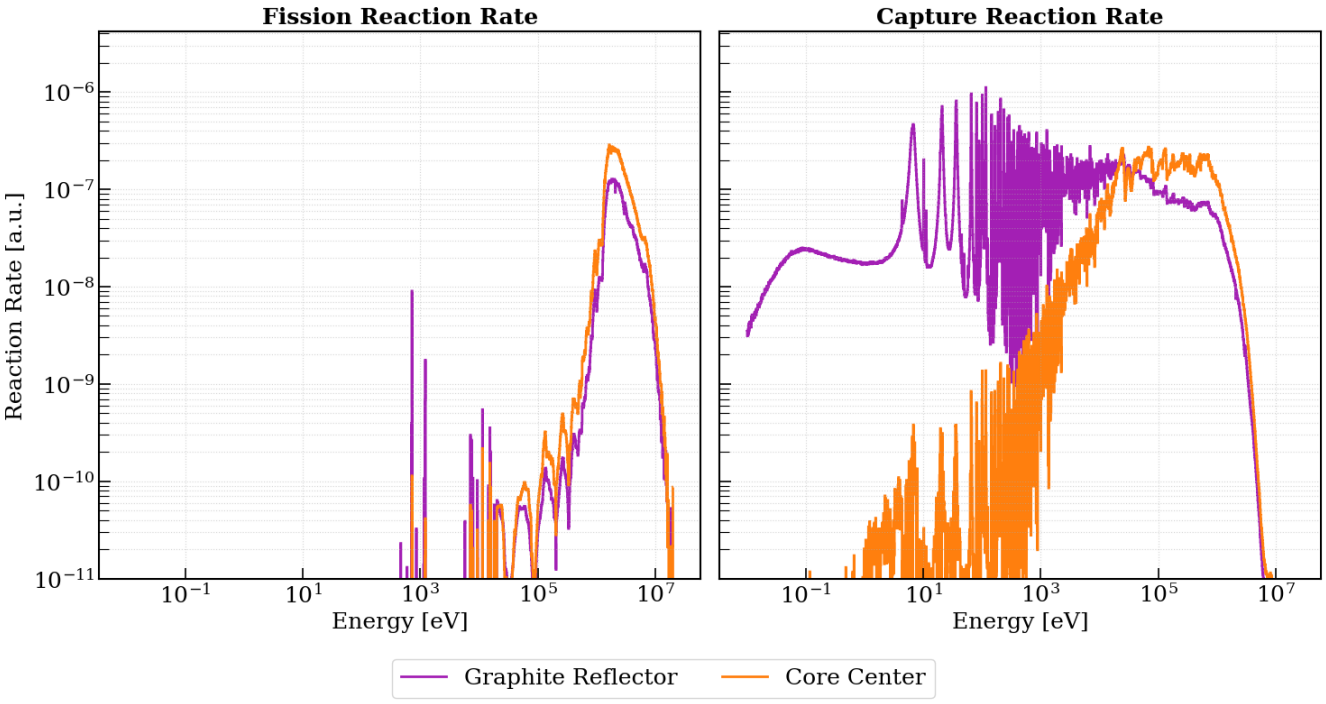


Figure 5.4: Fission vs capture reaction rates in the ^{238}U sample, distribution in energy, in the Graphite Reflector and Core Center assemblies.

Region	Total Fission	Total Capture	Ratio (F/C)
Graphite Reflector	1.10×10^{-5}	1.44×10^{-4}	7.62×10^{-2}
Core Center	2.38×10^{-5}	8.02×10^{-5}	2.96×10^{-1}

Table 5.2: Integrated Reaction Rates and Ratios.

A comprehensive discussion of the results should also include the neutron importance, which plays a role in the reactivity worth expression (Equation 2.6). However, calculating the importance function is computationally demanding and lies beyond the primary scope of this work. Consequently, it has been omitted, with the exception of brief remarks in Section 3.2.3.

5.3 ^{238}U sample reactivity worth temperature variation and trends

Table 5.1 indicated three promising locations: the Graphite Reflector, the Core Center and the Core Periphery. Table 5.3 shows the reactivity worth computed with the ^{238}U sample at 200 K and 900 K in these locations. The ACE files of the cross sections at different temperature are produced with SANDY. For comparison, the $\Delta\rho$ computation in the Graphite Reflector at every temperature was rerun using the SERPENT2 standard Doppler Broadening method *tmp*, see Section 2.5.1, and it yielded fully compatible results.

	Reactivity Worth [pcm]		
Location	**200 K**	**300 K**	**900 K**
Graphite Reflector	-26.0 ± 0.7	-26.9 ± 0.7	-30.0 ± 0.7
Core Center	-13.7 ± 0.7	-13.8 ± 0.7	-13.8 ± 0.7
Core Periphery	-7.1 ± 0.6	-7.9 ± 0.6	-10.2 ± 0.7

Table 5.3: $\Delta\rho$ by insertion of ^{238}U sample at different temperatures. Errors represent 1-σ.

In order to isolate the reactivity worth caused only by the temperature change, the EVDM formula, explained in Section 2.2.2, is applied component by component on the two k_{eff} vectors produced by the simulation with sample inserted at the two different temperatures.

The results are presented in Table 5.4, considering the sample heated up to 900 K, or cooled down to 200 K, both starting at 300 K. Figure 5.5 shows the full effect of the sample together with the reactivity worth only due to temperature change.

	Reactivity Worth [pcm]	
Location	**300 K $\rightarrow$ 200 K**	**300 K $\rightarrow$ 900 K**
Graphite Reflector	0.9 ± 0.7	-3.1 ± 0.6
Core Center	0.08 ± 0.7	0.00 ± 0.6
Core Periphery	0.8 ± 0.6	-2.2 ± 0.6

Table 5.4: $\Delta\rho$ by ^{238}U sample temperature change. Errors represent 1-σ.

The sample temperature variation produced a significant reactivity worth in both the Graphite Reflector and in the Core Periphery, with a larger effect in the first. Increasing the sample temperature by 600 degrees impacted the core reactivity in the range of 2-3 pcm, while the cooling the sample by 100 K yielded a reactivity change of about 1 pcm. These fundamental results demonstrate the feasibility of studying temperature-driven reactivity changes in VENUS-F through small sample reactivity worth measurement.

Moreover, while heating the sample seems to be the best choice, the cooling approach results must not be overlooked, considering that the 200 K value is much larger than the presumed lower limit of the realizable temperature range, which is around 77 K, as reported in the study constraints (Section 1.4).

In the Core Center, both temperature changes did not lead to a statistically significant results. Previous considerations can be useful in explaining the reason. Since the first capture resonances produce the large majority of the reaction rates (Figure 4.7), the Doppler reactivity effect is driven by interactions at those energies. Consequently, a temperature change in the sample does not change neutron interactions in the Core Center, which presents a fast spectrum (Figure 3.1).

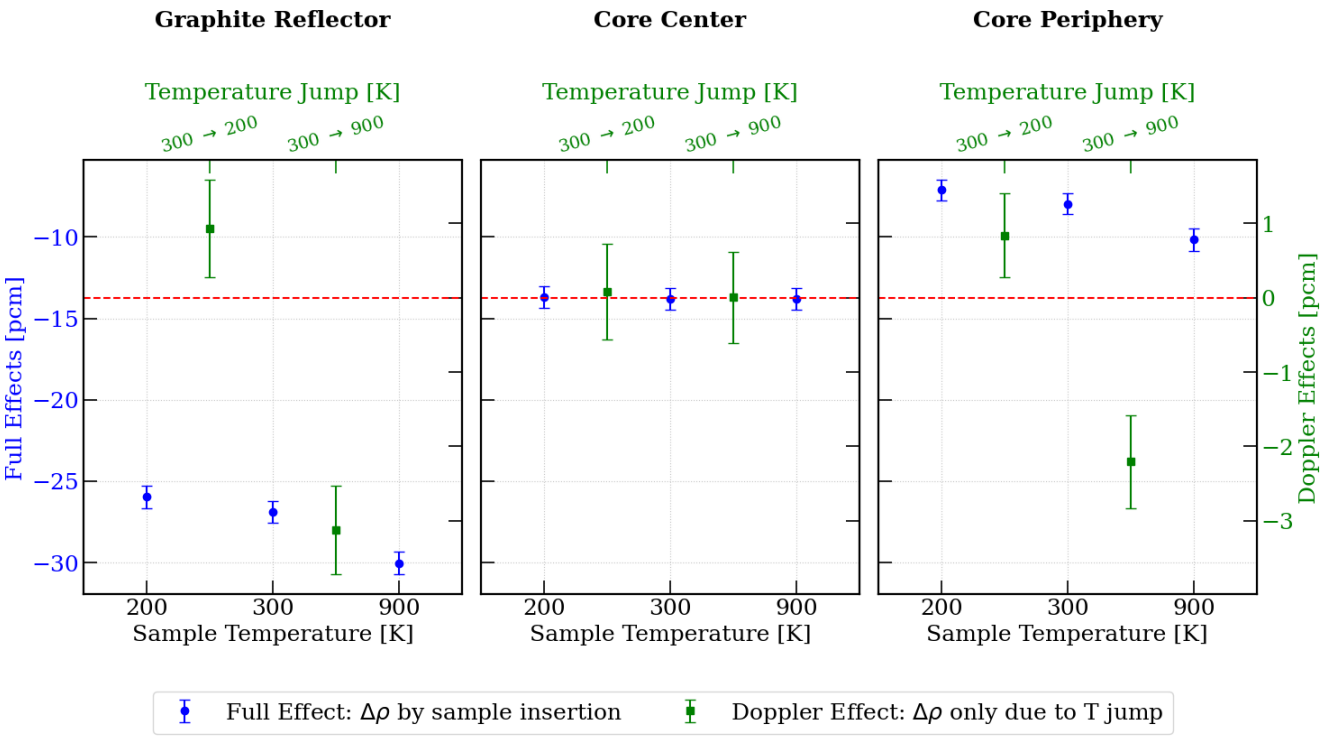


Figure 5.5: The blue points show the $\Delta\rho$ of ^{238}U sample insertion across various temperatures (bottom x-axis). The green points show $\Delta\rho$ due solely to the temperature jump (top x-axis). Error bars represent 1-σ.

Two additional temperatures (600 K and 1200 K) were investigated for the two promising locations, to add information on the $\Delta\rho$ behavior on temperature. Expanding the dataset enabled to improve the fit of the temperature-dependent reactivity worth curve. Once the fitted curve is obtained, it can be used to estimate the $\Delta\rho$ at any temperature.

As shown in Eq. 2.16, reactivity feedback by Doppler effect follows a logarithmic trend in temperature. Then, the fitting employs a logarithmic model, with two degrees of freedom:

$$\Delta\rho(T) = a \cdot ln(T) + c \tag{5.1}$$

The non-linear least squares fitting implemented in `ScyPy` [55] provides the best parameters for the model chosen and their covariance matrix, used then to construct the confidence intervals. The `curve_fit` function received in input the average value and their absolute errors. Figure 5.6 shows the results for sample insertion at different temperatures. Furthermore, Table 5.5 reports the fitting parameters yielded by `curve_fit`.

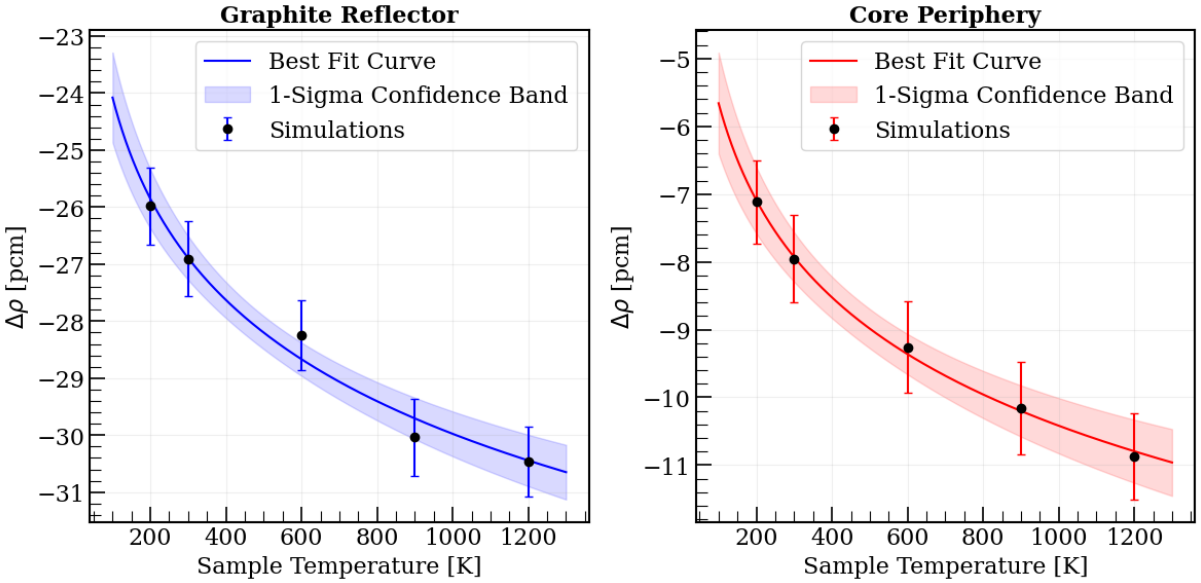


Figure 5.6: Reactivity worth from ^{238}U sample insertion: computed values and fitting function on temperature.

Parameter	Graphite Reflector	Core Periphery
Parameter a	-2.561 ± 0.435	-2.067 ± 0.424
Parameter c	-12.283 ± 2.752	3.860 ± 2.655

Table 5.5: Fitting parameters for $\Delta\rho$ temperature curve by ^{238}U sample insertion.

The logarithmic relationship expected both from the theory (Section 2.4) and from the trends of the "Simulation" points in Figure 5.6, is confirmed by the excellent fitting. The fitting's confidence band, in the region delimited by the computed points, is around 0.3 pcm. Thus the function can be used between 200 and 900 K to predict the sample reactivity worth with a precision that would be computationally challenging to obtain via simulations. Moreover, outside of those boundaries, it is still possible to retrieve quite precise reactivity worth results. For example, the function has been used to compute the Doppler $\Delta\rho$ given by a sample cooled down to 77 K, reported in Table 5.6, for Graphite Reflector and Core Periphery. This approach is of significant interest: both locations exhibit a sample effect above 2.5 pcm, which increases to 3.5 pcm in the Graphite Reflector.

Region	Value [pcm]
Graphite	3.5 ± 1.0
Periphery	2.8 ± 0.9

Table 5.6: $\Delta\rho$ yielded by cooling the ^{238}U sample down to 77 K, starting at 300 K. The values are computed via the fitting model. Errors refer to 1-σ.

Moreover, the fitting function allows quantifying the temperature change that produces a reactivity worth larger than the threshold of detectability, which is around 1 pcm. Cooling the sample down to 180 K, or heating it up to 500 K, yield $\Delta\rho$ above the threshold for both the Graphite Reflector and the Core Periphery.

The results on reactivity worth by a temperature variation of the sample prompted several fundamental observations:

1. **Consistency with the expectations:** Consistently with the observation reported in the spatial flux study, the best location are in the Graphite Reflector and in the Core Periphery while the temperature change of the sample inside the Core Center has practically zero impact on the reactivity.

2. **Negative Doppler reactivity coefficient:** The $\Delta\rho$ values due to the temperature jump follow the general concepts of Doppler effect. A temperature increase enhances neutron capture, thereby reducing the reactivity, and vice versa. This behavior, previously only suggested by the reaction rate analysis in Chapter 4, is now clearly observed.

3. **Detectability of the temperature reactivity effects:** The Doppler reactivity effect is statistically significant in the Graphite Reflector and Core Periphery experimental assemblies. With values of approximately 2–3 pcm, it is within the detection capability of the VENUS-F experimental setup.

4. **Temperature trend fitting:** The reactivity worth by the sample follows a logarithmic distribution in temperature for both insertion and temperature change. Once some results have been computed via simulations, the construction of a fitting model allows reducing the uncertainties. Furthermore, the temperature change that yields a reactivity effect above a given cutoff value can be estimated.

5.4 Neutron flux and reaction rates in the sample

This section investigates the neutron flux perturbation caused by the sample in the two promising locations (Graphite Reflector and Core Periphery). 3D cylindrical mesh detectors comprising the sample volume were used to determine the energy-dependent and -integrated spatial distribution of the neutron flux and reaction rates (capture, fission and total). A similar approach was used to get the neutron flux spatial distribution over

the whole core, Section 3.2.3. This investigation aims to analyze the spatial variation of nuclear reactions within the sample, focusing particularly on potential spatial self-shielding effects [56].

5.4.1 Neutron Flux

Firstly, the energy-dependent neutron flux in the sample volume is analyzed. Figure 5.7 presents the comparison of the flux spectra within the sample and in an empty sample volume, in the Graphite Reflector location. The flux perturbation by the sample is presented as residuals. Instead, Figure 5.8 shows a magnified view around the first major capture resonance of ^{238}U, comparing the flux inside the sample at two temperatures, together with the relative variation due to the temperature change.

In the Graphite Reflector the neutron flux has huge dips in correspondence with the peaks of the resonances. The neutron flux depression is in accordance to the distribution of the cumulative capture reaction rate reported in Figure 4.7. In fact, the phenomenon is dominated by the first four or five resonances, while higher-energy resonances have a negligible effect. Moreover, the presence of localized capture peaks cause a decrease of the flux at the lowest energies: the residuals increase (in absolute value) below 0.1 eV.

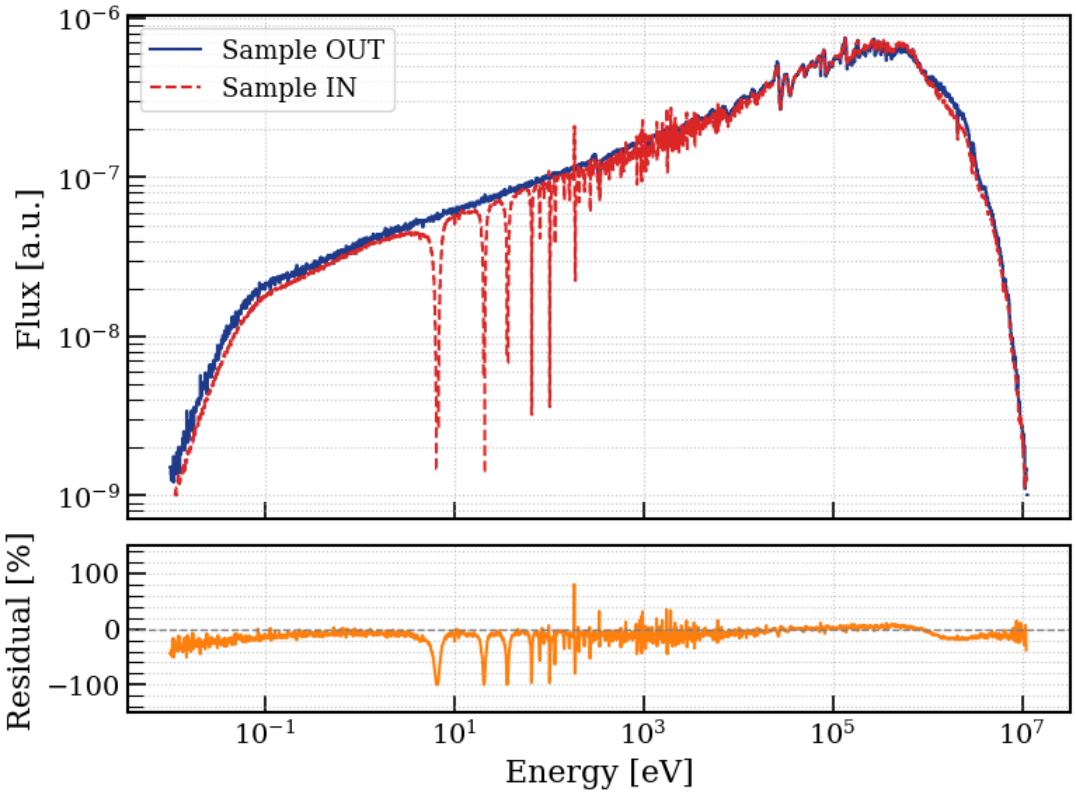


Figure 5.7: Comparison of neutron flux inside the ^{238}U sample and in an empty sample volume, in the Graphite Reflector assembly. Sample is at room temperature.

Location	Variation [%]
Graphite Reflector	-4.7 ± 1.3
Core Periphery	-3.6 ± 2

Table 5.7: Total flux relative percentage variation due to ^{238}U sample insertion, in the two promising locations. Errors refer to 1-σ.

The relative change in total neutron flux caused by sample insertion is reported in Table‘5.7. The uncertainty has been propagated linearly considering 1-σ on the two values. For both locations the values are around 4%, with uncertainties equal or lower than 2%. The insertion of the sample results in a net flux reduction, as neutron capture predominates over fission.

The flux depression across the first ^{238}U capture resonance varies with temperature in a manner consistent with the capture reaction rate evaluated in Chapter 4. Indeed, it qualitatively mirrors Figure 4.6. The Doppler broadening mitigates the flux drop in the peak and enhances it along the wings.

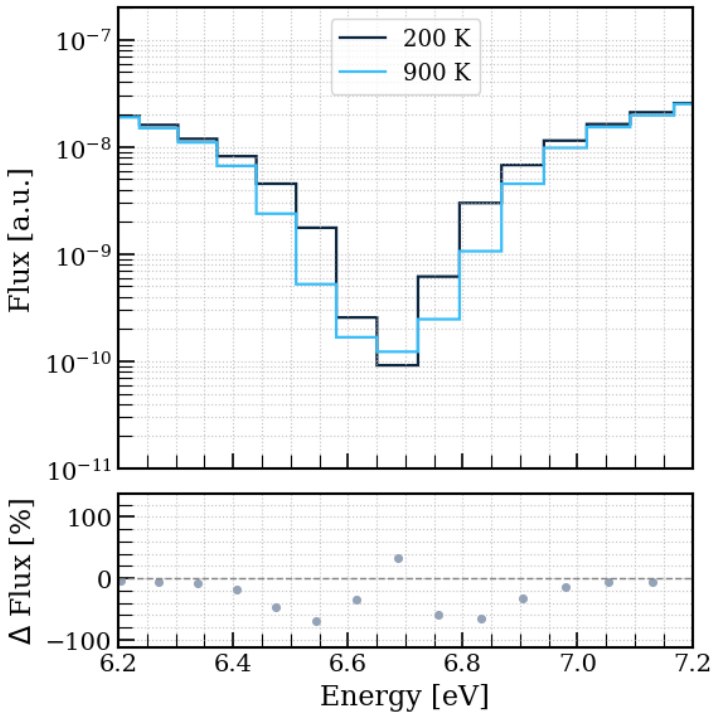


Figure 5.8: Comparison of neutron flux around the first ^{238}U capture resonance, located at 6.7 eV, inside the sample at 200 K and 900 K. Sample is inside the Graphite Reflector.

Additionally, the flux has been extracted across horizontal and vertical cuts across the sample, at different heights and orientations. Moreover, an energy discretization equal to the one implemented in Section 3.2.3 is considered, reported in Table 3.5. Figure 5.9 shows

the total neutron flux spatial distribution in a horizontal cut at three different heights. Extra views, as well as the results of the Core Periphery, are reported in Appendix B.

Regarding the spatial mapping, the analysis on both locations found flat distributions of the flux, with marginal variation across the geometry. The homogeneity is true for all the energy intervals considered.

In conclusion, the energy and spatial self-shielding present opposite characteristics. While in energy the resonance peaks influence strongly the spectra, across the geometry there is no relevant depression of the flux. The latter is true for all the energy intervals.

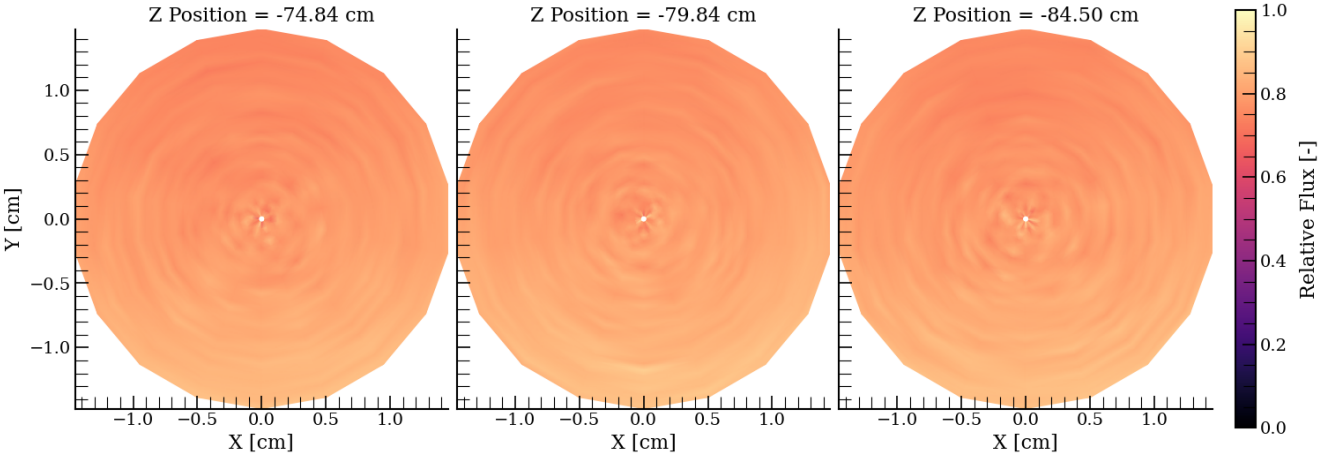


Figure 5.9: Total flux spatial distribution in the ^{238}U sample located in the Graphite Reflector channel. The cuts are horizontal, along the sample midplane and at the north and south of the sample.

5.4.2 Reaction rates

The 3D spatial distributions of capture, fission and total reaction rates at three temperatures were extracted using the five energy groups (Table 3.5) and rigorously examined along all relevant planes and directions.

Figure 5.10 shows a vertical cut of the energy-integrated capture reaction rate in the sample at 300 K, in both locations. Figure 5.11instead presents the capture rate in the different energy groups and at several temperatures, in the Graphite Reflector. Other prospective views and core locations are presented in Appendix B.

The following key observations can be made:

- The temperature has a small influence on the values, and it does not affect significantly their distribution. Of course, its global effect is significant, but for the present investigation it has not a relevant influence.

- The energy-integrated capture reaction rate, as well as the neutron flux, are axially homogeneous since the axial flux gradient in the 10 cm around core midplane is small.

- The total capture rate presents significant radial spatial self-shielding, with a reaction rate drop of around 50% after the first millimeters along the radius. Still, the internal part is significantly reactive. The subdivision in energy group (Figure 5.11) highlights at which energies the spatial self-shielding is located. Bin 2, which contains the first resonances, exhibits a pronounced concentration along the boundary, with values approaching the maximum within the first few millimeters and dropping to approximately 20% in the interior. Bin 3, which also comprises resonances, presents a mild localization of the reaction rates, with a small temperature influence, that tends to increase the values over the whole domain. All the other bins have homogeneous distributions.

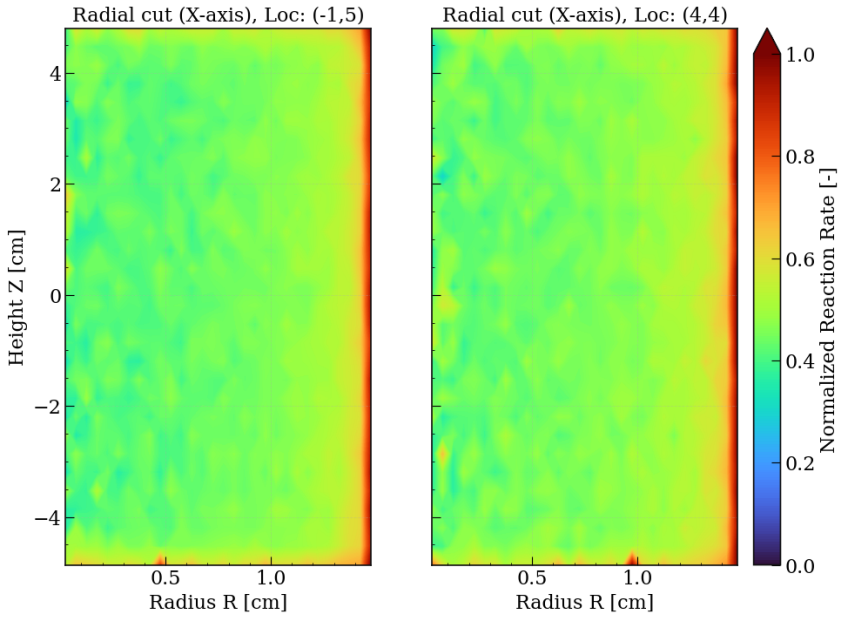


Figure 5.10: Normalized ^{238}U capture rate (energy-integrated), at 300 K, in the sample inserted in the Graphite Reflector (left) and in the Core Periphery (right). The cut is vertical, along the x-axis.

The radial profile of the reaction rates is presented in Figure 5.12. The radius is divided into percentiles, each containing a proportion of the overall reaction rate. Additionally, the corresponding fraction of sample volume for each percentile is indicated in bold. Comparing these values reveals whether the reactions are homogeneously distributed. A slight imbalance is observed only for capture reactions: the outermost region show larger reaction in relative terms, because of the capture reaction rate concentration at the sample boundary (Figure 5.10). This phenomenon is enhanced focusing specifically on the energy region that comprises the first two resonances (Bin 2 in Table 3.5). This is shown in the second plot in Figure 5.12. The discrepancy between volume and integrated reaction rate in the outer shell is larger: for both locations, the outer shell (which comprises 36% of the volume) houses around 52% of the total quantity. The discrepancy mainly affects the

three adjacent portions, each losing roughly 4% reactivity compared to the homogeneous case. Temperature change has negligible impact, except for the capture rates in Bin 2. In that case, it tends, in the two outer portions, to attenuate the concentration, lowering the discrepancy between volume and reaction rate.

Total reaction rates integrated over the entire energy domain do not show non-uniformity along the radius (second rows of plots in Figure 5.12), whereas in the second energy group there is a mild effect, as a consequence of the capture concentration in the outer portion.

This investigation indicates that there are no parts of the sample volume, apart of some few millimeters at the boundary which tend to concentrate the capture reaction rates, which contribute so little to the reactivity that their potential removal would not affect its global effect on the core. Nevertheless, a calculation using a hollow cylindrical sample was performed, with the results presented in Section 5.5.2.

The final evaluation regarding reaction rates inside the sample considered the integrated ^{238}U capture rates, focusing on the temperature variation. They were extracted using a detector matching the exact sample volume, and simulating a large number of neutron histories to reduce uncertainty. Figure 5.13 shows the results, for the two promising locations. In both positions, temperature effects are significant and coherent with the general consequences of the Doppler effect. In fact, the heated sample shows capture rates larger by 5.5-6%, while the cooling approach yields variations around 2%.

Comparing the results with the integrated capture rates computed in Chapter 4, reported in Figure 4.9, the effect of the sample is clear. In fact, the calculations in Chapter 4 did not take into account the flux spectra depression in the sample and this caused strange behavior in the Graphite Reflector.

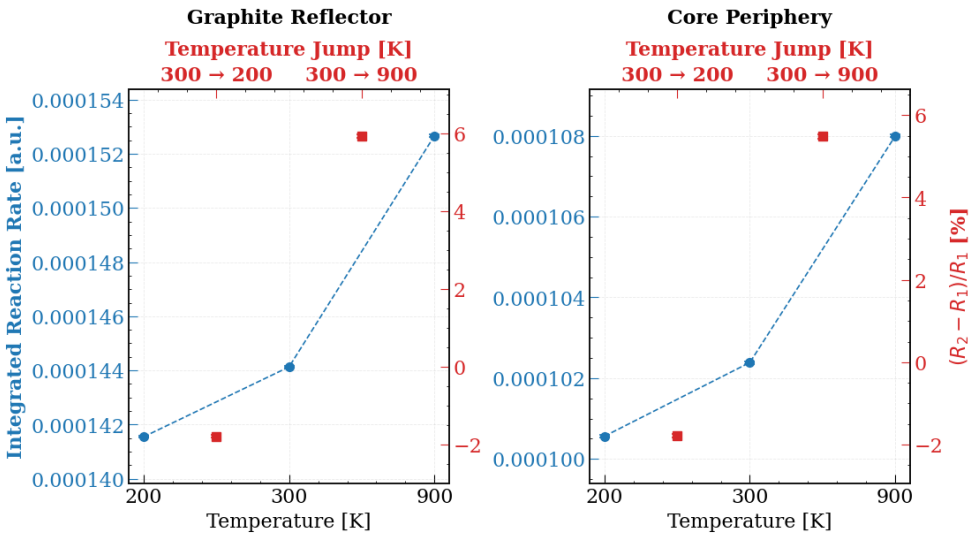


Figure 5.13: Integral ^{238}U capture rates in the sample, together with their relative percentage variations in temperature. Absolute values at the corresponding temperatures are shown in blue (left axis), while relative changes, in percentage, with respect to the 300 K reference value are shown in red (right axis). Errorbars refer to $1 - \sigma$.

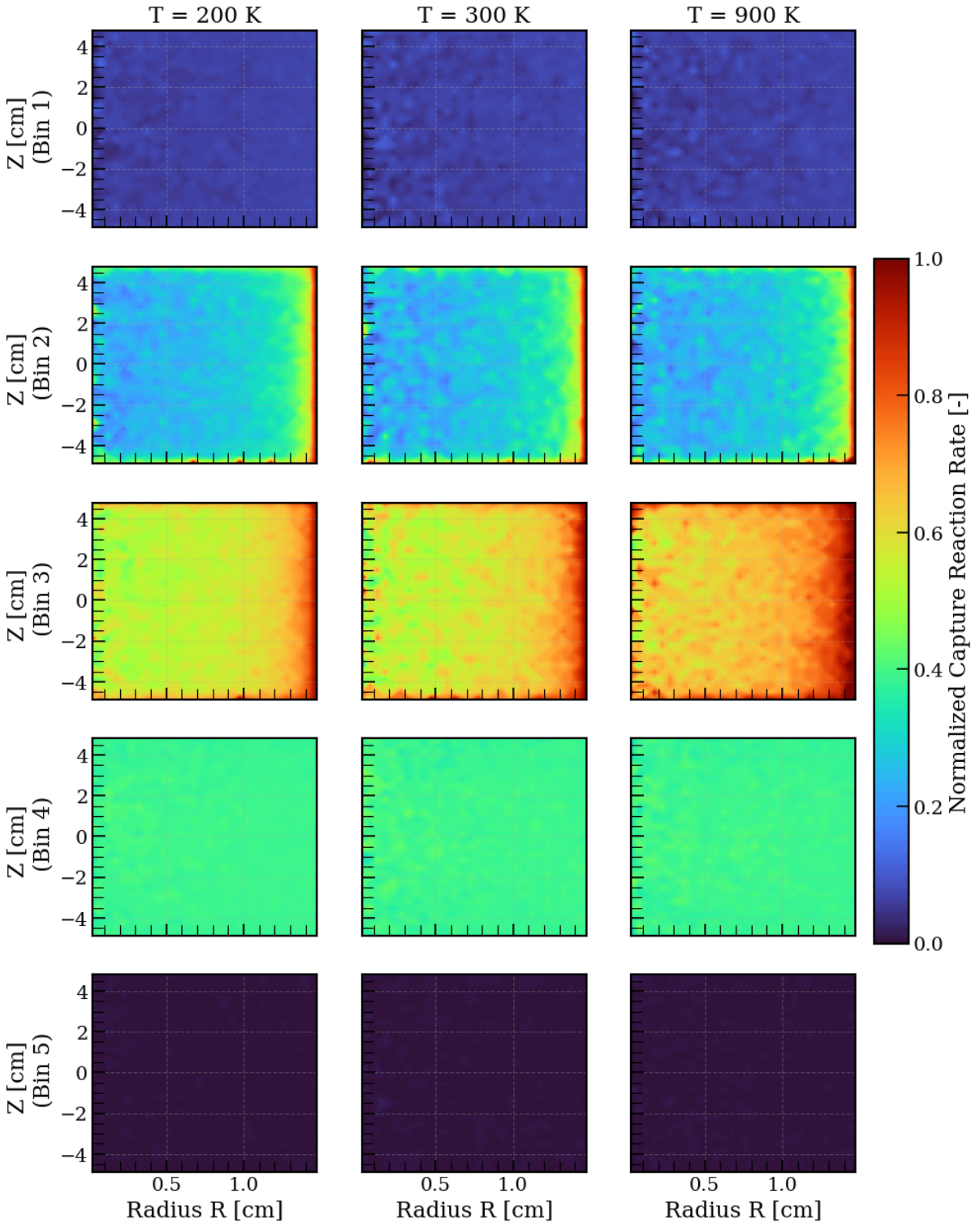


Figure 5.11: ^{238}U capture rates in the five energy intervals, for the Graphite Reflector. Three temperatures are shown. The cut is vertical, along the x-axis.

[H]

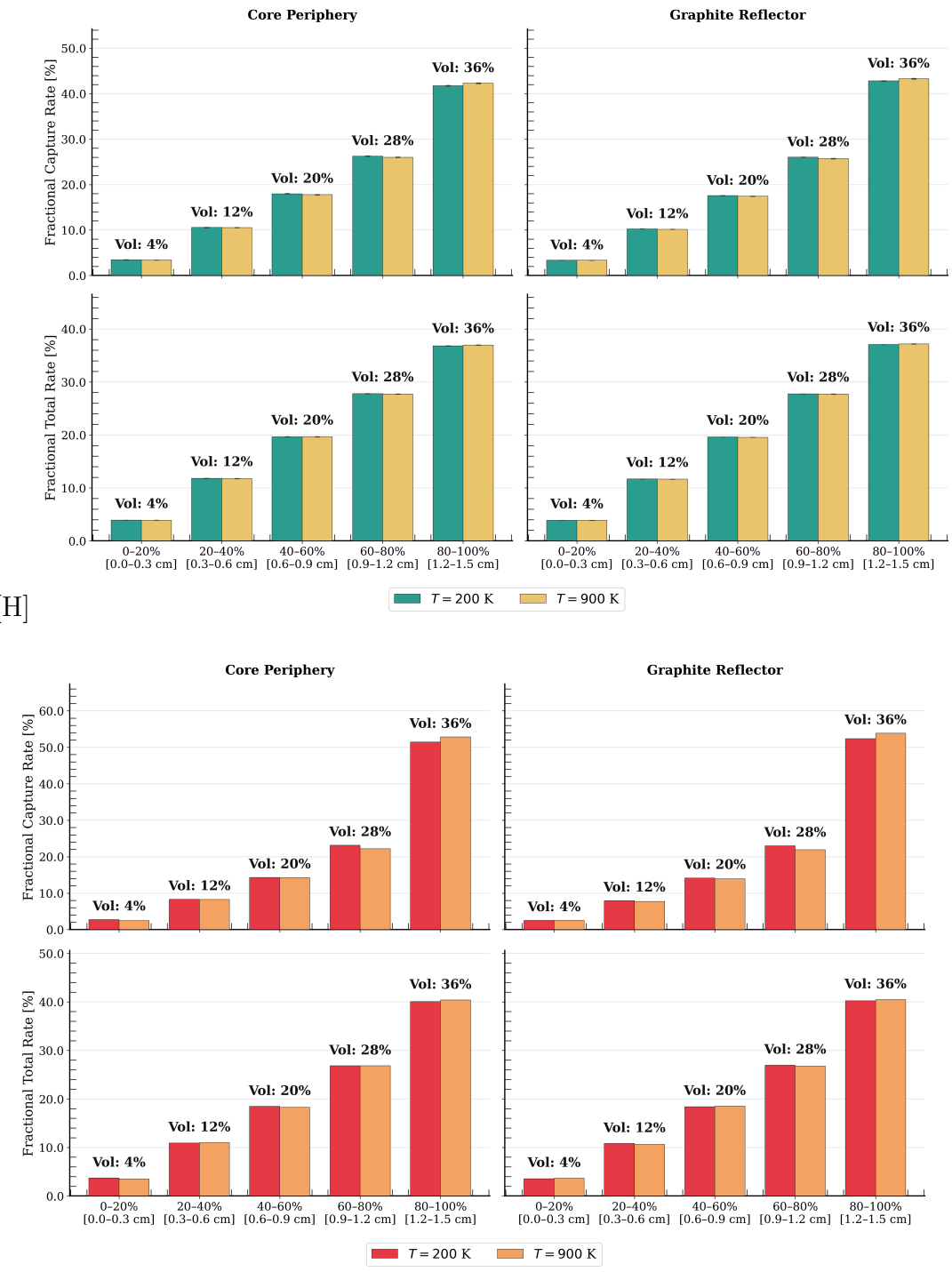


Figure 5.12: Fraction of ^{238}U capture rate contained in each radial portion of the sample. In the first plot, the values are integrated over all the energy domain. In the bottom, they refer only to the second energy bin (Table 3.5). In bold, the volume fraction of each portion is indicated. Both capture and total reaction rates are shown.

5.5 Investigation of the $\Delta\rho$ in modified geometries

The analysis of the ^{238}U sample reactivity worth is extended to some alternative configurations, both in terms of sample geometry and core layout, which are discussed in separate subsections.

5.5.1 Long sample

The Doppler reactivity worth calculations were repeated for the two most promising configurations using an extended 30 cm long sample, with the results summarized below. This geometry modification was applied to increase the sample mass, enhance the reactivity effect and hence the Doppler reactivity effect. While more technically challenging, this setup provides an alternative to the standard design to evaluate how sample length affects temperature-dependent reactivity.

	Reactivity Worth [pcm]		
Location	**200 K**	**300 K**	**900 K**
Graphite Reflector	-66.6 ± 0.6	-68.3 ± 0.6	-75.9 ± 0.6
Core Periphery	-26.5 ± 0.7	-28.2 ± 0.6	-32.4 ± 0.7

Table 5.8: $\Delta\rho$ by insertion of ^{238}U sample at different temperatures (30 cm long sample).

	Reactivity Worth [pcm]	
Location	**300 K → 200 K**	**300 K → 900 K**
Graphite Reflector	1.7 ± 0.6	-7.5 ± 0.7
Core Periphery	1.7 ± 0.6	-4.2 ± 0.6

Table 5.9: $\Delta\rho$ given by temperature change of the ^{238}U sample (30 cm long sample).

Longer samples amplify the reactivity effect, but it is difficult to establish a priori a direct relationship between the increase in length and its consequence on the reactivity change. In fact, the reactivity worth depends on the sample dimensions, but also the neutron flux and the importance in that region and how the neutrons interacts in the sample. The $\Delta\rho$ values from the elongated sample suggest that reactivity contributions from sample insertion (Table 5.8) and temperature variations (Table 5.9) display distinct sensitivities to size increases, an effect most pronounced in the Core Periphery assembly. The increased mass entails relevant increase of the reactivity effect, that, for the insertion, reach tens of pcm in the Core Periphery and even around 70 pcm in the Graphite Reflector. The temperature-induced reactivity worth are well above the uncertainty and the detectability limit, achieving 1.7 pcm for the cooling approach, and more than 4 pcm for the heating case.

Table 5.10 shows the relative sample reactivity worth increase due to the increase in length (3x) across the investigated core locations. The sample reactivity worth increases of more than 3 times in the Core Periphery assembly, while the Doppler reactivity effect increases by a factor of around 2. In the Graphite Reflector the scaling is more similar: both the absolute reactivity worth and the net Doppler reactivity effect increase by approximately 2.5 times. These results indicate that the sample length increase would be more beneficial in maximizing the Doppler reactivity effect in the Graphite Reflector. However, these reactivity worth ratios are affected by large relative uncertainties and small variations are not statistically significant.

In conclusion, an increase in sample length would cause a remarkable gain in the reactivity worth, both by insertion and temperature change. Moreover, cooling this sample by 200 K would yield a reactivity change comparable to a 600 K temperature increase in the standard sample. This represents a promising strategy for the design of future experimental campaigns.

	Graphite Reflector		**Core Periphery**	
T [K]	**Insertion**	**Doppler**	**Insertion**	**Doppler**
200	2.6 ± 0.1	1.9 ± 1.5	3.7 ± 0.3	2.0 ± 1.5
300	2.5 ± 0.1	–	3.5 ± 0.3	–
600	2.6 ± 0.1	3.2 ± 1.6	3.4 ± 0.3	2.5 ± 1.3
900	2.5 ± 0.1	2.4 ± 0.5	3.2 ± 0.2	1.9 ± 0.6
1200	2.6 ± 0.1	2.7 ± 0.5	3.0 ± 0.2	1.6 ± 0.4

Table 5.10: Ratio comparison (30 cm / 10 cm) for $\Delta\rho$ by insertion of ^{238}U sample and by temperature change, in two location, at different temperatures.

5.5.2 Hollow sample

The second modification investigated consists in drilling a 12 mm hole in the center of the cylindrical sample, yielding approximately a 16% volume reduction. With this modification, the goal is to extend the reaction rate analysis (Section 5.4.2) and investigate the role of the central part of the sample in the reactivity worth temperature change.

If every portion of the sample contributes roughly equally to the reactivity worth, removing a portion of it should reduce its reactivity worth in direct proportion to the removed volume fraction. It should be true both for sample insertion and temperature change.

Table 5.11 shows the insertion $\Delta\rho$ variation between the full and hollow sample for different locations and temperatures. The uncertainties have been computed applying FOP, implementing the linear propagation formula on average $\Delta\rho$ values and their associated errors. This method exhibits limitations, as the magnitudes of the reactivity-worth

variations induced by geometric modifications is comparable to the uncertainties on the total values (approximately 0.7 pcm).

Temperature	Graphite Reflector	Core Periphery
200 K	0.878 ± 0.035	0.963 ± 0.136
300 K	0.869 ± 0.034	0.963 ± 0.118
900 K	0.863 ± 0.030	0.848 ± 0.088

Table 5.11: Ratio of $\Delta\rho_{\text{ins}}$ (insertion reactivity) due to ^{238}U sample cylinder excavation.

The sample modification reduced by about $13\% \pm 3\%$ the reactivity worth in the Graphite Reflector. Due to its maximum $\Delta\rho$, this position is the optimal for quantitatively analyzing the impact, assessing that the reduction in reactivity worth scales with the fraction of removed volume. This indicates that flux depression in the sample has a limited effect on the sample reactivity worth, and the peak in capture reaction rates presented in Section 5.4 does not have a significant impact. No significant temperature-dependent trend can be deduced because it is masked by the uncertainty.

On the other hand, in the Core Periphery, the uncertainties are much larger, around 11%, thus no precise indications can be given.

Ultimately, while the results in the Graphite Reflector confirms a clear proportionality between the reactivity reduction and the removed volume, the Core Periphery requires further reduction in uncertainties to draw definitive conclusions regarding the excavation effect. Nonetheless, further investigations on an hollow sample can be valuable, since the mass reduction, that impacted the reactivity by sample insertion, could not be as important for the temperature effect on reactivity. Indeed, the impact of temperature-driven changes on reactivity primarily stems from the first resonances, whose effect is concentrated in the outer shell of the cylinder (Figure 5.11).

5.5.3 Alternative core configuration

The last model modification is motivated by two key observations:

1. Doppler induced reaction rate change and reactivity effect is dominated by low-energy resolved resonance region (∼1–100 eV); hence, neutron thermalization by the graphite moderator enhances the temperature impact on the reactivity.

2. The neutron flux is the highest in the core center as well as the neutron importance, therefore enhanced neutron absorption in the core center yields a substantial reactivity effect.

Following these indications, the Core Center experimental location was modified by replacing the holed lead experimental assembly with a graphite one with the same geometry.

T [K]	$\Delta\rho_{\text{insert}}$	$\Delta\rho_{\text{Dopp}}$
200	-23.6 ± 0.6	
		1.0 ± 0.7
300	-24.7 ± 0.6	
		0.1 ± 0.7
900	-24.55 ± 0.6	

Table 5.12: Values of $\Delta\rho$ by insertion of ^{238}U sample and by temperature change for the new configuration. The $\Delta\rho_{\text{Dopp}}$ values are positioned between the two temperatures that constitute the change, always starting from 300 K.

Figure 5.14 shows the horizontal cut of VENUS-F model with the graphite assembly (orange) in the core center. The sample (yellow) was then inserted into this new experimental location and the reactivity worth at different temperatures was computed.

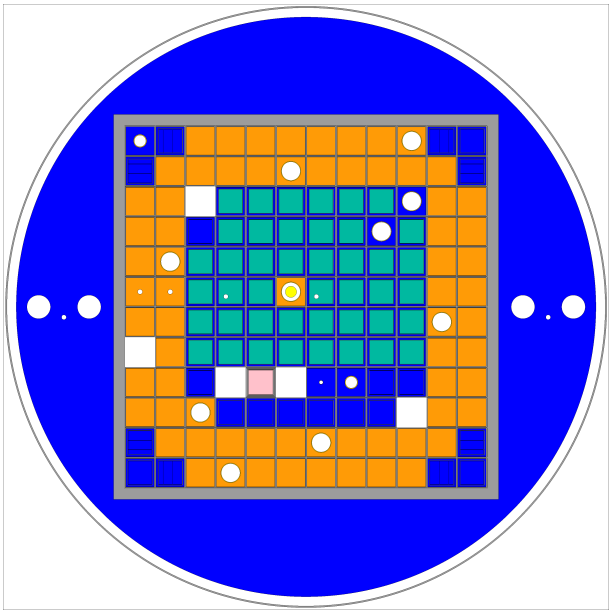


Figure 5.14: Mid-plane view of the simplified VENUS-F core, with the new configuration under analysis. The sample is in (-1,1).

The modification caused the neutron flux spectrum in the Core Center assembly to soften. Figure 5.15 shows the flux spectra comparison between the unperturbed and modified configuration. The epithermalization by the graphite is evident, increasing the flux by hundreds of percentage below 10^4 eV. Overall, the integrated flux spectra grew by 4.0 ± 0.8 %. This is driven by neutron epithermalization, which enhances fissions in adjacent fuel assemblies.

Table 5.12 shows the reactivity worth results (both sample insertion and temperature

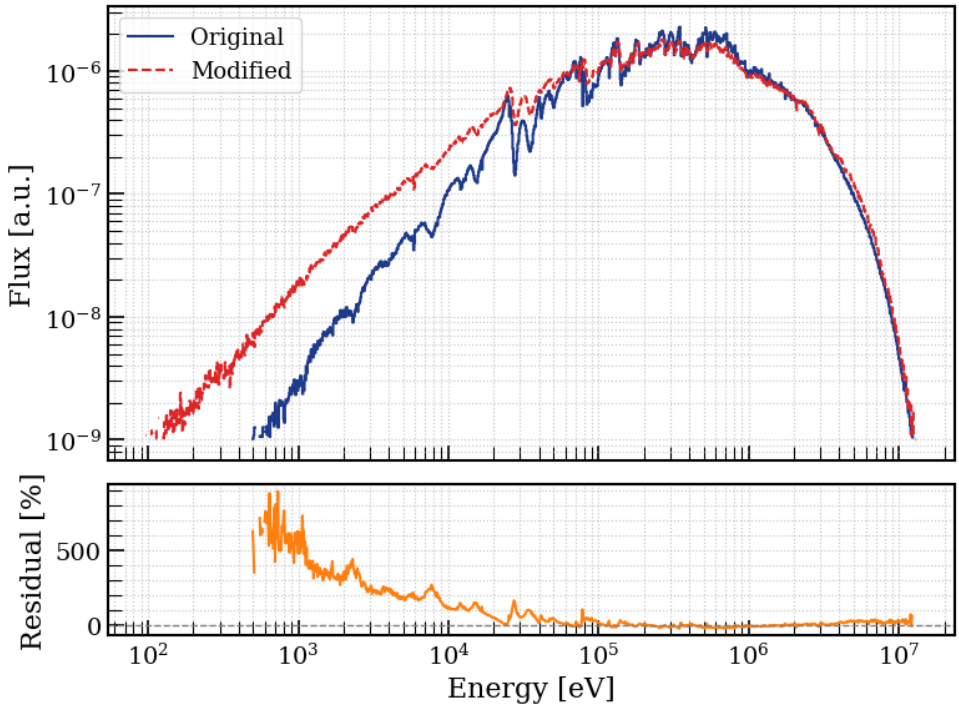


Figure 5.15: Effect of core modification on flux spectra in the Core Center experimental assembly.

change). The sample insertion yields 23 to 25 pcm, double of the effect of the same sample inserted in the same location in a standard lead experimental assembly, see Table 5.3. This is caused by the neutron flux softening which increases capture reactions in the sample as discussed in Section 5.2. The temperature increase does not yield any noticeably change to the reactivity while cooling the sample seems to give a positive $\Delta\rho$ of 1 pcm, comparable to that of the most promising location (Graphite Reflector). This behavior is difficult to account for, as a phenomenon with these characteristics has not been observed previously in this investigation. However, because the reported uncertainty of 0.7 corresponds to the 1-σ level, this result is subject to a notable statistical uncertainty.

In conclusion, the performance of the new configuration does not justify the required effort, as modifying the core would have negligible impact in the capability to assess Doppler reactivity effects.

Chapter 6

Reactivity worth of alternative materials

This chapter extends the temperature-dependent sample reactivity worth analysis to an additional fissile nuclide (^{240}Pu) and other relevant materials for lead-cooled reactors (^{56}Fe, O_{16} in Al_2O_3) with strong resonances at high energy. Both the computational methodology and the sample size remain the same. Furthermore, the analysis is restricted to the two promising locations identified in the previous chapter. This facilitates a straightforward quantitative comparison focusing exclusively on the sample's physical effect on the core's nuclear characteristics. Future investigations could also include the Core Center, given the high resonances of both materials at fast energies.

As for the simulations with the ^{238}U sample, the cross-sections at different temperature are produced with SANDY. These are incorporated in the sample material definition within the SERPENT2 input file.

6.1 ^{240}Pu sample temperature-dependent reactivity worth

^{240}Pu is analyzed because of its importance for Gen IV reactors and its contribution to the nuclear data uncertainty on the Doppler coefficient in fast systems [8]. Both standard and long sample geometry were studied, with a brief comparison between them. Figure 6.1 shows the results for the 10 cm long sample.

The reactivity worth of inserting the sample is positive, since fission dominates over capture reactions and the net reactivity effect is larger in magnitude compared to the ^{238}U sample. The reactivity effect is maximized in the Core Periphery, that is closer to the fuel and has a lower epithermal tail. The spectral influence on the relationship between capture and fission in the different locations can be quantified using the procedure explained in Chapter 4, focusing on the reaction rates. In fact, Table 6.1 reports the integrated capture and fission reaction rates together with their ratios, in the two locations. The fission

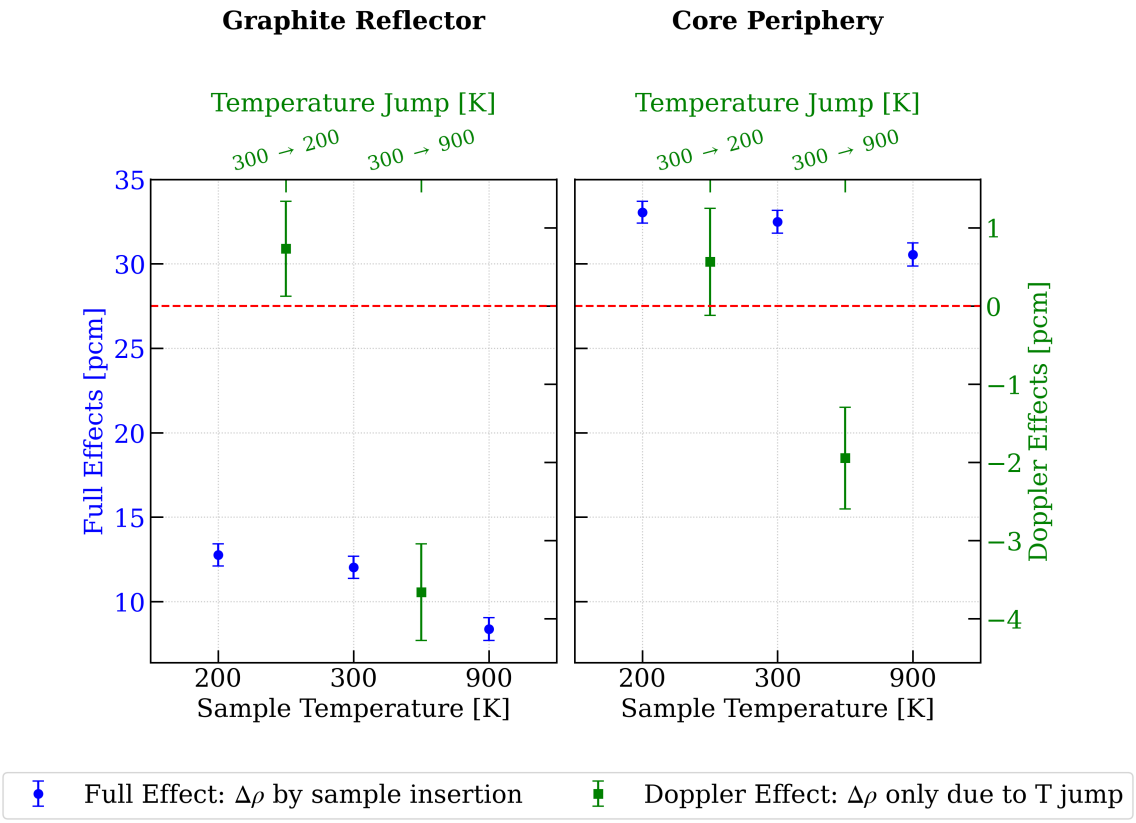


Figure 6.1: ^{240}Pu sample $\Delta\rho$ in two core locations. The blue points show the $\Delta\rho$ of sample insertion across various temperatures (bottom x-axis). The green points show the net $\Delta\rho$ due to the temperature jump (top x-axis). Error bars represent 1-σ.

rate is always 3 order of magnitude lower than capture, but it relatively increases in the Core Periphery, where the F/C ratio grows by about 32% as compared to the Graphite Reflector.

Position	Total Fission	Total Capture	Ratio (F/C)
Graphite Reflector	1.38×10^{-4}	3.10×10^{-2}	4.46×10^{-3}
Core Periphery	1.84×10^{-3}	2.82×10^{-1}	6.52×10^{-3}

Table 6.1: ^{240}Pu total capture and fission reaction rates comparison between the two positions.

Concerning the Doppler effect, the results are quite similar to the ^{238}U sample, both for inverse proportionality with temperature and for the actual values (few pcm for heating, slightly below 1 for cooling). This similarity reflect the affinity in the capture cross sections, shown in Figure 6.2. Moreover, it is consistent with the results obtained by Kato et al. [12]

(Section 1.2). Additionally, the Graphite Reflector position remains optimal, indicating that the characterization of spatial and energy distribution of the neutron population prior to modeling the perturbation, reported in Chapter 3, gives useful insights for studying small-sample reactivity effects. However, a comprehensive prediction must account also for the neutron importance and the sample's properties (i.e. cross sections).

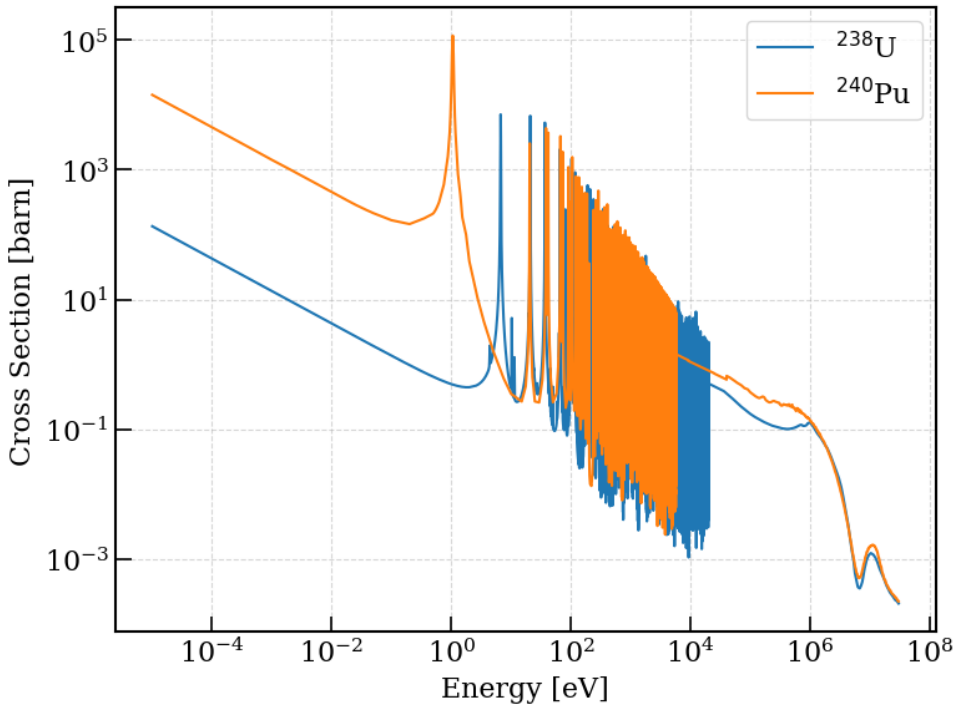


Figure 6.2: Capture cross sections of ^{238}U and ^{240}Pu.

6.1.1 Long sample

The effect of increasing the sample length is presented in Table 6.2. Unlike for the ^{238}U samples (Table 5.10), in the Graphite Reflector assembly the increase in reactivity worth is much larger than the one of mass.

	Graphite Reflector		**Core Periphery**	
T [K]	**Insertion**	**Doppler**	**Insertion**	**Doppler**
200	5.0 ± 0.3	4.2 ± 3.6	3.1 ± 0.1	4.2 ± 5.2
300	5.0 ± 0.3	–	3.1 ± 0.1	–
900	6.2 ± 0.5	2.4 ± 0.4	3.1 ± 0.1	3.1 ± 1.1

Table 6.2: Ratio comparison (30cm / 10cm) for ^{240}Pu, for insertion and temperature change effects, in the two locations, at different temperatures.

While large uncertainties in the Doppler $\Delta\rho$ by cooling results preclude definitive conclusions, the results for the 300 $\rightarrow$ 900 K transition are significantly clearer. The sample elongation increases $\Delta\rho_{300\rightarrow900}$ of about 3 times in the Core Periphery and by a factor 2.4 in the Graphite Reflector. The difference from the previous case is clear especially for $\Delta\rho$ by sample insertion. While the ratio on reactivity worth is consistent with the volume growth in the Core Periphery configuration (around 3), a significant larger value is found for the other location (between 5 and 6). This implies that the positive reactivity effect is amplified at the long sample top and bottom edges, potentially due to an increase of fissions reactions in those regions.

To better analyze the situation, the axial neutron flux profile along the height of the experimental assembly and the neutron flux spectrum at the ends of the long sample position (in the absence of the sample) is examined (Figure 6.3). The neutron population is, as expected, cosine-distributed and mostly concentrated at energies around 0.1/1 MeV, for both the locations. Regarding the spectra, at the edges they are practically identical between top and bottom and reduced with respect to the midplane. The discrepancy is quite uniform across energy and larger for the Core Periphery, around 67% versus the 34% of the Graphite Reflector case.

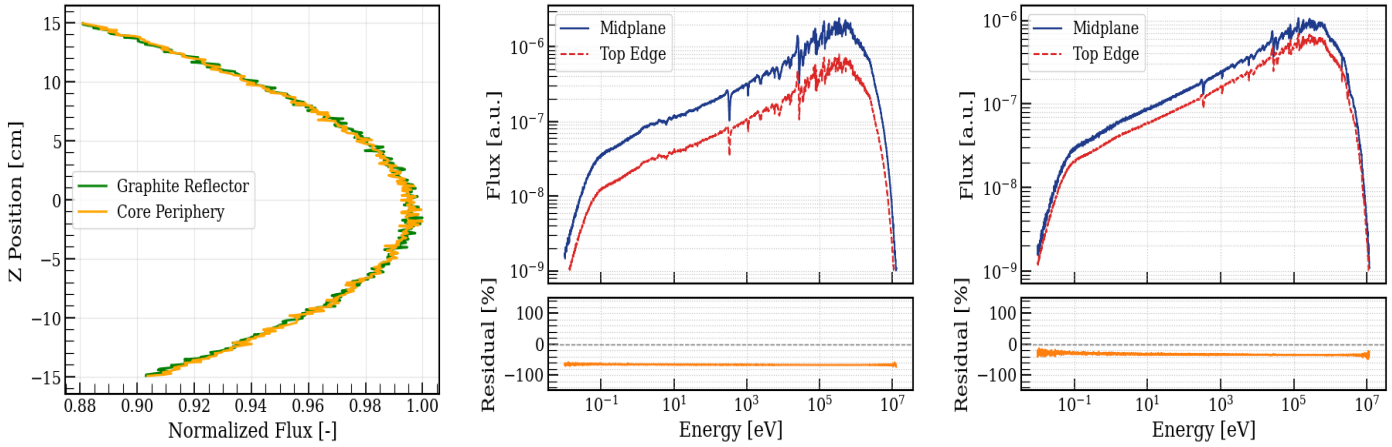
The investigation then focused on the reaction rates, comparing ^{240}Pu and ^{238}U, applying the procedure presented in Chapter 4. The distributions in energy do not provide valuable insights, while from the integrated values and their ratios, reported in Table 6.3, some considerations can be derived.

	^{238}**U**		^{240}**Pu**	
	GR	**CP**	**GR**	**CP**
Midplane	4.50×10^{-3}	6.452×10^{-3}	7.14×10^{-3}	1.08×10^{-2}
Edges	6.18×10^{-3}	4.23×10^{-3}	1.04×10^{-2}	6.90×10^{-3}
Ratio	**1.37**	**0.65**	**1.46**	**0.64**

Table 6.3: Absolute values of F/C inside the sample, at the midplane and in the edges, together with their ratio (Edge/Midplane). Both fissile materials are reported, for the two promising locations.

For both nuclides, the two locations present opposite behavior on the F/C value between the center and the edges of the sample. In the Core Periphery, the F/C decreases by about 35% for each nuclides, while in the Graphite Reflector it increases. However, the increase at this location is more pronounced for ^{238}U (46% vs. 37%). These values indicate that at the edges, the sample exhibits a higher capture rate only in the Core Periphery (CP), whereas in the Graphite (GR), the reaction rate actually shifts toward fission. However, the results on $\Delta\rho$ ratios only partially agree with this finding. Specifically, the ratios for ^{238}U in the GR validate the increase in fission, as the $\Delta\rho$ values are all negative and the ratios are lower than 3 (which is the mass increase). In contrast, for ^{240}Pu, for which the $\Delta\rho$ values are positive, the C/F growth do not justify the excessively large ratios observed.

Similarly, the prevalence of captures in the sample edges inside the CP is confirmed for ^{238}U (where the ratios tend to exceed 3), but this trend is not reflected for ^{240}Pu, as its values do not fall below 3. In summary, in the presence of fission, standard reaction rate analysis reveals its limitations., because the impact of the emitted particles in the system is of great importance.



(a) Axial flux **(b)** Core Periphery **(c)** Graphite Reflector

Figure 6.3: Neutron flux in the large sample volume (empty). First figure shows the axial profiles in the Core Periphery and Graphite Reflector; the middle and right figures present the neutron flux spectrum at top edge (bottom is identical), together with the one in the midplane, for the two locations.

6.2 Temperature-dependent reactivity worth of additional non-fissile materials

This section investigates the reactivity worth of non-fissile materials relevant to heavy-metal-cooled reactor designs, focusing on nuclides with strong high-energy resonances that can have a significant Doppler reactivity effect. The evaluation centers on two key elements: iron (primarily its most abundant isotope, ^{56}Fe) and oxygen (critical for ceramic fuels such as MOX). While iron is evaluated in elemental form within the sample, oxygen is introduced via alumina (Al_2O_3), a solid compound already present in the VENUS-F core.

6.2.1 ^{56}Fe temperature-dependent reactivity worth

^{56}Fe reactivity effect is driven by scattering and capture. The sample density was increased to equal the one of ^{238}U in order to maximize the Doppler reactivity effect. Tables 6.4, 6.5 report the reactivity worth results.

The sample insertion yields a reactivity worth of approximately -6 pcm in the Graphite Reflector and around 2 pcm in the Core Periphery. The $\Delta\rho$ has opposite sign depending on

	Reactivity Worth [pcm]		
Location	**200 K**	**300 K**	**900 K**
Graphite Reflector	-5.8 ± 0.7	-5.8 ± 0.7	-6.6 ± 0.6
Core Periphery	3.0 ± 0.6	2.7 ± 0.7	2.0 ± 0.6

Table 6.4: $\Delta\rho$ by insertion of ^{56}Fe sample at different temperatures

	Reactivity Worth [pcm]	
Location	**300 K → 200 K**	**300 K → 900 K**
Graphite Reflector	-0.00 ± 0.6	-0.8 ± 0.6
Core Periphery	0.3 ± 0.6	-0.6 ± 0.6

Table 6.5: $\Delta\rho$ given by ^{56}Fe sample temperature jump (Doppler effect).

the core location, which was not observed for any other case studied until now. Inserting the sample in the fuel region has a positive reactivity effect, whereas placing it in the reflector gives a negative one. By looking at the capture and elastic scattering reaction rate distributions in energy, shown in Figure 6.4, an hypothetical explanation is proposed. Scattering reactions slow down neutrons, the spectral change impacts ^{238}U and ^{235}U fission rates. The first reduces, as detailed in Section 5.2, the latter increases due to the spectrum softening. Moreover, scattering can reflect them to the active core, causing a net positive effect. The interplay between these phenomena justify the reactivity worth dependence on sample position. Placing it in the Core Periphery (where the incident neutron spectrum is harder) the scattering tends to prevail; given its proximity to the core, this increases overall reactivity. On the other hand, with the sample in the Graphite Reflector the scattered neutrons are less likely to re-enter the active fuel zone. Moreover, at lower energies, the discrepancy in reaction rates between scattering and capture narrows and the high capture peak at 1 keV can have a bigger influence. This gives an additional contribution towards more negative reactivity. Together, these competing mechanisms account for the observed results.

Finally, even with a fictional and much larger density, the computed temperature effect on reactivity worth is negligible, indicating a very weak influence of the Doppler effect.

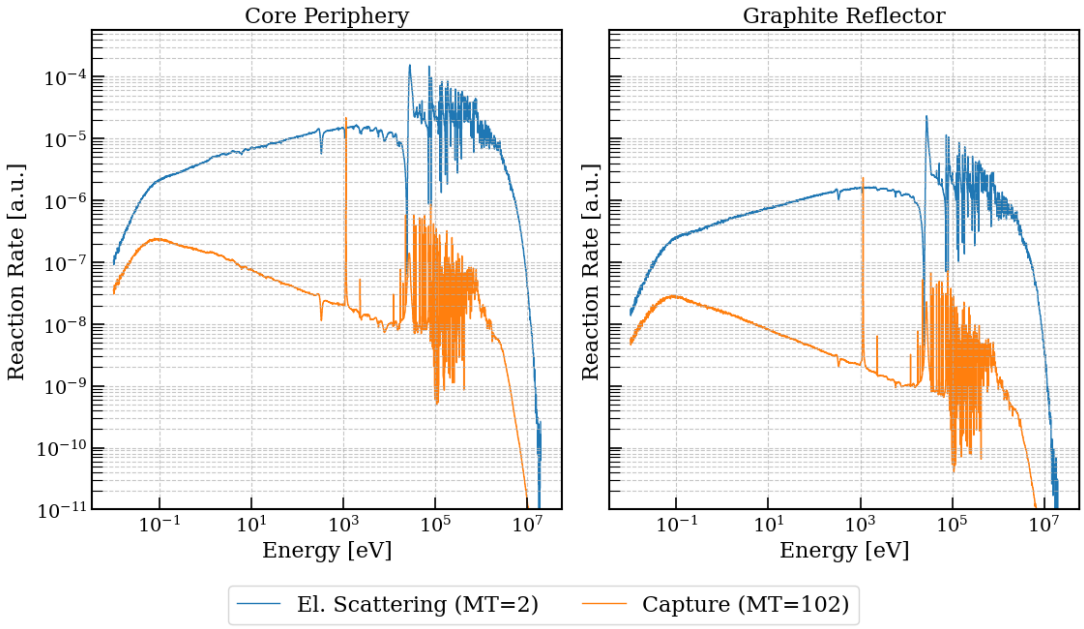


Figure 6.4: ^{56}Fe reaction rate distributions in energy: elastic scattering and capture.

6.2.2 Alumina (Al_2O_3) temperature-dependent reactivity worth

The last material analyzed is alumina, containing ^{16}O, which has a strong capture resonance around 0.2 MeV and important others in the elastic cross section, shown in Figure 6.5. Oxygen is highly present in oxide-fuels and alumina is a convenient solid form. Moreover, it is already present in VENUS-F, to mimic the oxide fuel of Lead-cooled reactors . The computations have been performed with the standard sample size, the actual alumina density and the results are presented in Figure 6.6.

The $\Delta\rho$ from sample insertion is positive and ranges between 12 and 15 pcm. The effect in the Core Periphery is larger by about 20%; this indicates that, as for the ^{56}Fe case, and deducible also by looking at the cross sections, the scattering dominates, slowing down neutrons and producing a larger positive reactivity if the sample is nearer the active fuel region.

The temperature effect on reactivity worth is very small, with no clear trend for both heating and cooling. The statistical uncertainties, of approximately 0.7 pcm, preclude the possibility of identifying a net effect of temperature changes. Therefore, in conclusion, the Doppler effect has a marginal influence on reactivity on the alumina sample, that cannot be precisely identified with the methodology implemented in this investigation.

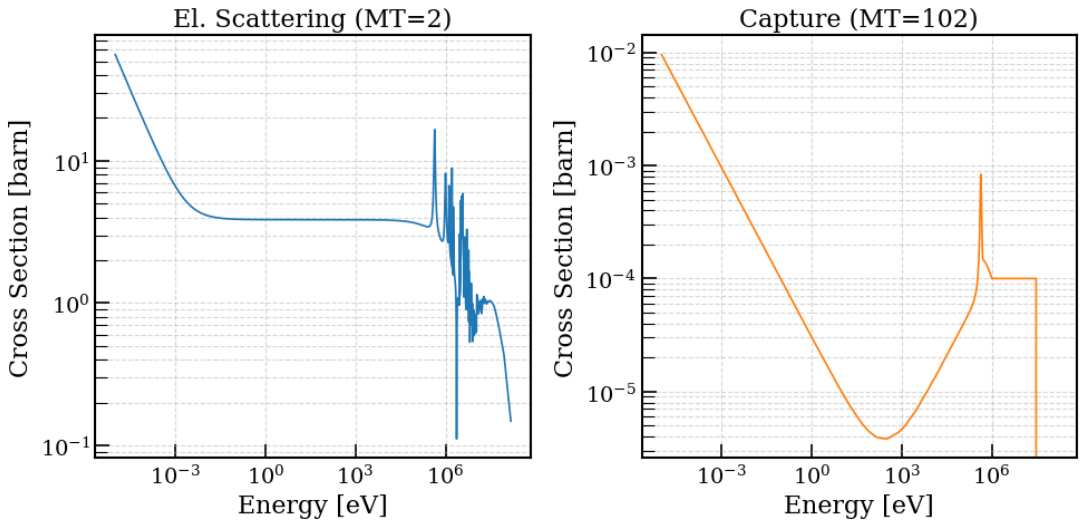


Figure 6.5: Elastic scattering and capture cross section of ^{16}O. Obtained using SANDY.

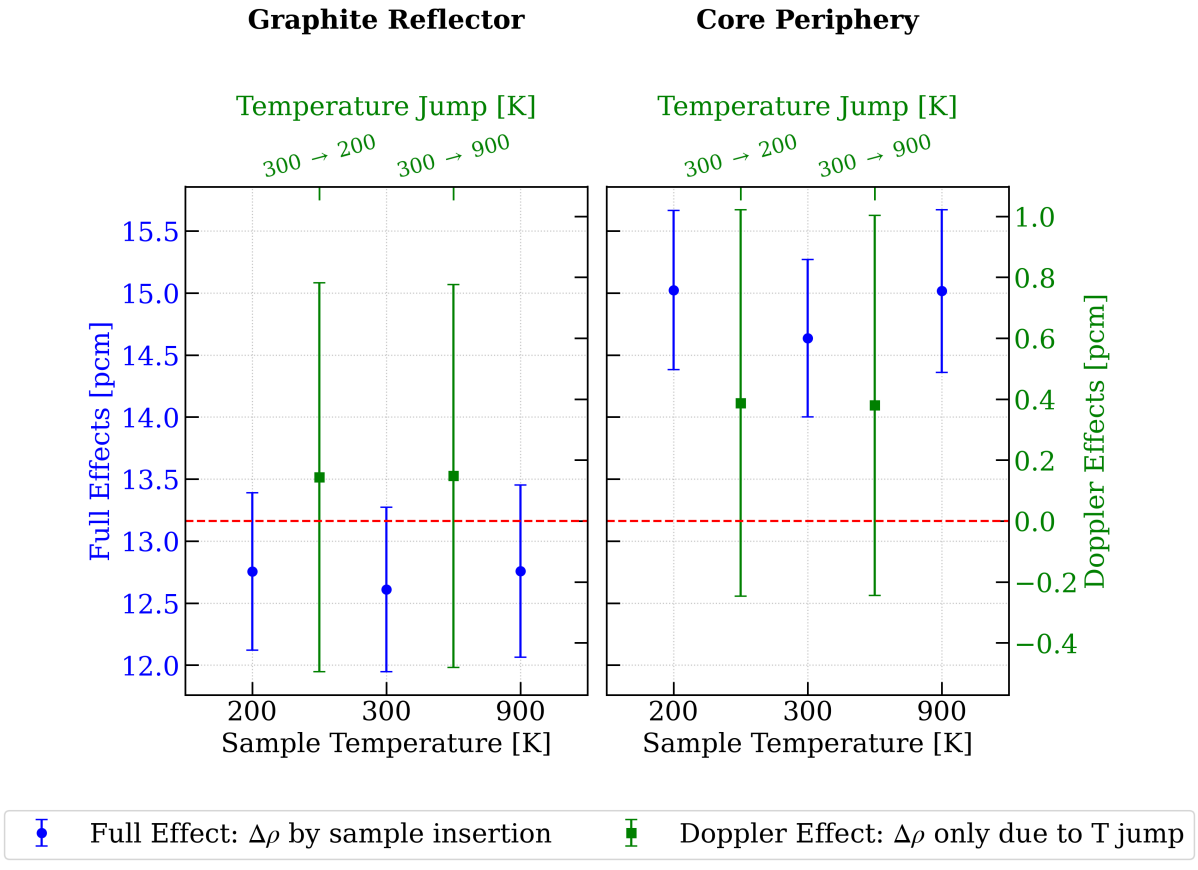


Figure 6.6: The blue points show the $\Delta\rho$ of Al_2O_3 sample insertion across various temperatures (bottom x-axis). The green points show $\Delta\rho$ due solely to the temperature jump (top x-axis). Error bars represent 1-σ.

Chapter 7

Conclusions

Lead-cooled fast reactors are currently investigated as promising revolutionary nuclear technologies that ensure high performance, improved fuel utilization, and inherent passive safety features. VENUS-F is a zero-power reactor operated at SCK CEN, designed as a neutronic mock-up for fast heavy-metal-cooled technologies. A wide range of experiments can be performed, including oscillation experiments, which investigate reactivity worth of small samples.

This work presented the computational feasibility study for a new experimental campaign in the VENUS-F reactor. The primary target of the experiment is to reproduce the temperature reactivity feedback in power fast reactors, specifically the fuel Doppler effect without increasing the full reactor temperature, which would be practically challenging. The planned strategy consists in measuring the reactivity effect due to the insertion of small samples in the reactor, with a particular emphasis on their temperature dependence. The objective of this work was to identify the suitable experimental conditions to measure the Doppler effect through this method, considering the technical experimental constraints. The experimental setup is constrained by the achievable sample temperature range (77-1200 K), the requirement for a sufficiently large reactivity effect ($\geq$ 1 pcm) to ensure adequate measurement precision, and the availability of experimental channels. The analysis explored the reactivity worth dependence on three parameters: sample characteristics (size and material), temperature (both heating and cooling) and spectral conditions achieved in the experimental channel where the sample is inserted. In line with the literature review, ^{238}U constituted the main subject of study, complemented by a less detailed analysis of other sample materials such as ^{240}Pu, ^{56}Fe, and Al_2O_3.

The entire work implemented the JEFF 3.3 nuclear data library. Further investigations could focus on repeating the computations with different libraries, assessing the bias due to nuclear data evaluations.

Firstly, this work presented the comparison of a fully detailed VENUS-F model, which is computationally expensive, and a simplified, homogenized model specifically developed to reduce computational cost and ease this study. The similarity of simplified model with the detailed one was assessed by comparing the neutron flux spectrum and ^{238}U capture

rate in selected experimental locations.

Then, the analysis focused on reaction rates, exploiting the proportionality between the change of the sample reactivity worth and the change of reaction rate caused by variation in sample temperature. The model folds ^{238}U capture cross section with VENUS-F neutron flux spectra. Regarding the cross section, the GroupWise (GW) representation exhibited high sensitivity to energy grid parameters, particularly in the complex resonance region reconstructed via NJOY. Collapsing the cross section on the energy grid produces a marked discretization error that prevents the curve from being tracked accurately. This limitation persists even with a very fine 2000-group mesh, which has been used for the calculations. However further analysis on the group-wise cross section indicated that the absolute discrepancy caused by the discretization in the high energy resonance region tends to be minor.

The neutron flux spectra were computed with the detailed model in four experimental locations, both inside the active core region and in the reflector. While the fission peak was present at all locations, the presence of an epithermal tail was strongly conditioned by the proximity of the moderating graphite in the reflector. This presence was expected to have a considerable impact.

The multi-group reaction rates were then computed. The energy-dependent reaction rates showed good approximation of the resonance impact, even though the representation of the resonances degrades at high energies. Moreover, the temperature effect was clearly visible in the first resonances, where variations in the order of tens of percentages can be found. The cumulative reaction rates highlighted that between 80 and 85% of the interactions happen along the first 4-5 resonances (between 5 and 100 eV).

The integrated capture rate variations due to temperature changes remain very small, often they are compatible with zero effect within 1σ of statistical uncertainty. Furthermore, the four selected experimental locations respond differently to temperature variations: while most reaction rates generally increase with temperature, the results inside the Graphite Reflector show an exception to the trend. Only the Monte Carlo errors were considered, and their propagation required uncertainty quantification, in particular for the reaction rate variation due to temperature. The computation considered the correlation among reaction rates at different temperatures. The correlation was found to be strong (lower values around 0.93) and exploiting the covariance matrix, it was possible to obtain the associated error. Features of the Doppler effect were detected, with temperature increase enhancing the captures. Still, the variations are minimal and no definitive answers can be given.

The reactivity worth calculations employed the *EigenValue Difference Method*, which computes $\Delta\rho$ as the difference of eigenvalues ($\frac{1}{k_{\text{eff}}}$) of unperturbed and perturbed simulated states. The simulations were performed with the SERPENT2 Monte Carlo particle transport code, employing the simplified VENUS-F model to improve computational efficiency. Estimates were refined using random sampling across independent simulation runs.

The analysis of the ^{238}U sample started by calculating the absolute reactivity worth of inserting the sample at room temperature. Three of the investigated core locations (Core

Center, Core Periphery and Graphite Reflector) yielded significant negative reactivity effect, larger than 6 pcm. The study of temperature-dependent reactivity changes revealed no effect in Core Center, while non-negligible temperature influence of the order of few pcm was found in the Graphite Reflector and Core Periphery. In these locations the sample reactivity worth decreases with increasing temperature and vice versa, which aligns with the general Doppler theory. For these promising locations, which can be exploited in future experiments, additional calculations were performed investigating multiple temperatures to collect more data points and construct a temperature-dependent sample reactivity worth curve. The curve, which achieves an uncertainty of about 0.3 pcm across most of the temperature range, serves as a tool to evaluate reactivity effects for a sample at different temperatures without repeating the calculations. The fit shows that temperature jumps down to 180 K or up to 500 K push $\Delta\rho$ above the detectability threshold (1 pcm) in both the Graphite Reflector and Core Periphery.

The analysis of the neutron flux perturbation in the sample showed strong energy flux depression, in correspondence of the first few capture cross section peaks, dependent also on temperature. On the other hand, the spatial flux distribution did not show significant self-shielding, in both locations. Regarding the reaction rate, only the capture rate showed non-negligible localization along the first tenths of a millimetre of the sample surface, with the effect concentrated in the energy region that comprises the first resonances. Temperature had a minor influence, tending to smooth out local concentrations.

Three modified sample and reactor configurations were considered to study the sensitivity to these variations. First, tripling the sample height (elongated sample) produced varying effects on reactivity worth depending on the core location where the sample is inserted, between 2-3 times the results from the standard sample. Second, reducing the volume by 16% by removing a central cylindrical part (hollow sample) led to a proportional decrease in reactivity worth (around 13%) in the Graphite Reflector, while the uncertainties in the Core Periphery precluded any indication. The high uncertainties also precluded assessing the impact on temperature-driven reactivity changes. Future analysis should aim at evaluating this impact, since the concentration of capture rates in the shell indicates the possibility to reduce the volume without degrading the Doppler effect on reactivity worth. Finally, testing a new experimental assembly core center, substituting the holed lead assembly with a graphite one, did not yield the expected increase in the temperature-dependent reactivity effects.

The investigation was extended to other materials, always considering the two most promising experimental locations. The insertion of a ^{240}Pu sample produced an absolute positive reactivity worth, opposite to the ^{238}U sample. The temperature effect on $\Delta\rho$ is rather similar to the ^{238}U case. Moreover, tripling the sample height induced a far larger increase (around five times) on $\Delta\rho$ in the Graphite Reflector assembly. After examining the flux spectra at the sample midplane and at the sample edges, resulting in different discrepancies in the two locations, a reaction-rate-based attempt was made to explain the results, with only partial success. Indeed, the change in fission to capture ratios between midplane and edges was not reflected in all the $\Delta\rho$ values and did not justify the results for the sample in the Graphite Reflector. ^{56}Fe showed non-negligible reactivity worth by

insertion only employing a fictitious increased density (same as ^{238}U), while the Al_2O_3 sample, considered to study the effect of oxygen, produced $\Delta\rho$ by sample insertion larger than 10 pcm with its real density. Nonetheless, the temperature change did not affect $\Delta\rho$ in either of the two cases. Future work can include computations for the sample in the Core Center, due to the strong resonances at high energies in the cross sections of both additional materials.

In conclusion, this study demonstrated the feasibility of small-sample temperature reactivity worth experiments for ^{238}U and ^{240}Pu in VENUS-F, confirming the detectability of the associated temperature effects. The Graphite Reflector emerged as the most promising experimental location, followed closely by the Core Periphery. Furthermore, both heating and cooling methodologies proved to be viable experimental approaches.

Appendix A

Further insights on cross section production

The procedure for reaction rates calculations described in Chapter 4 developed additional results on the characteristics of the two approaches for cross section production.

A.1 Number of points for PointWise reconstruction

The first interesting parameter is the number of points on which the PW cross section has been reconstructed, in particular its dependence on temperature. Table A.1 presents those number, that decrease with increasing temperature, with a big drop between stationary nuclei (0 K) and room temperature. A quick explanation can be given: the Doppler effects causes in a smoothing of the curves, which become less steep. Consequently, the linear interpolation optimization procedure needs a smaller number of nodes to follow their profile.

Temperature [K]	**Points**
0.1	138,208
200	70,416
300	65,647
450	61,406
600	58,550
900	54,974
1200	52,750

Table A.1: Number of points for PW reconstruction at different temperatures

A.2 Impact of the grid choice on GroupWise approach

Figure 4.4 shows the discretization error distribution in energy in the GroupWise representation, for different energy grids. While the first resonances are quite accurately resolved, with the discrepancies concentrated at the peaks, but the overall shapes preserved, the higher energy resonances are completely averaged out.

To investigate the discrepancy, a metric for quantification of the impact of the grid refinement has been defined, exploiting the Root Mean Squared Error:

$$\mathrm{RMSE} = \sqrt{\frac{1}{n}\sum_{i=1}^{n}(\sigma_i^{GW} - \sigma_i^{R})^2} \tag{A.1}$$

In this case, the reference is the PointWise representation. In order to have the same number of points in both the vectors, the GW has been "expanded" on the energy grid chosen by NJOY for the PW. This allows to actually produce a point per point distance vector, representing the approximation introduced by the collapsing procedure. Figure A.1 shows the RMSE of the grids with different temperatures and homogeneous weighting flux.

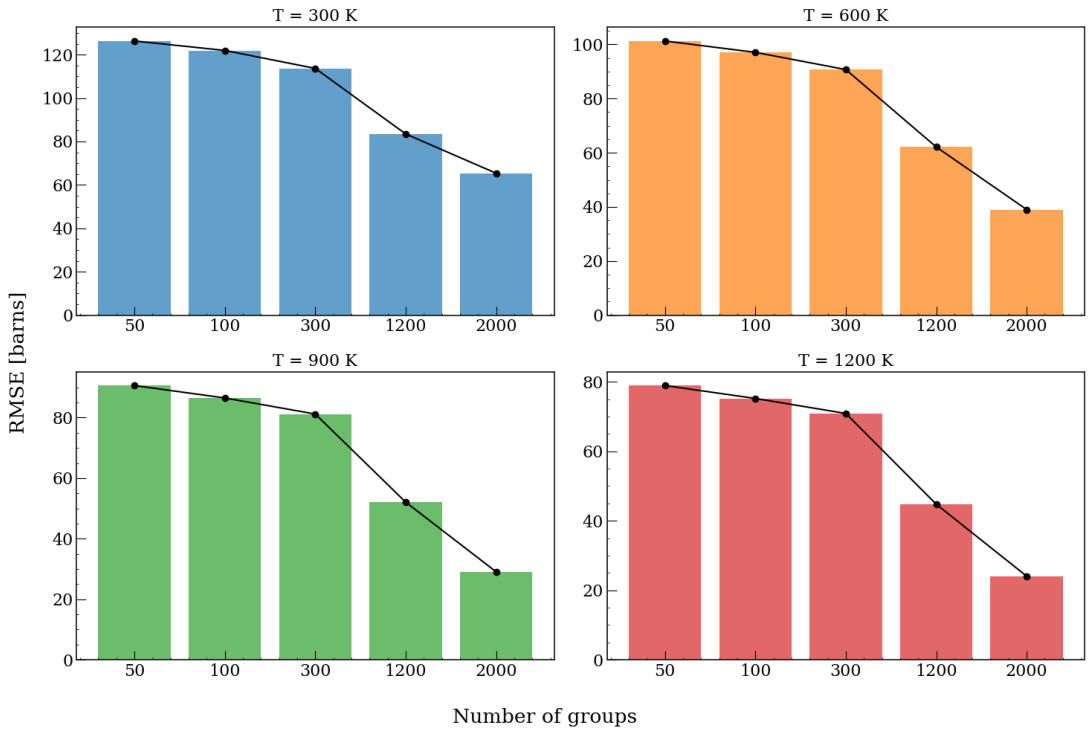


Figure A.1: Total RMSE for w=2 and multiple grids, at different temperatures

As expected, the RMSE decrease with increasing number of groups, but, especially at low temperatures, it still is pretty high, compared to the 50 groups case, even with 2000 groups. With higher temperatures, the RMSE is much smaller, probably due to Doppler broadening smoothing the peaks.

However, considering the previously observed discrepancy error, it is worth investigating where, across the energy domain, the majority of the differences between the two representations is. To do so, the energy range has been subdivided in five regions, looking at the features of ^{238}U capture cross section.

Acronym	Energy Region	Range [eV]
`st`	Thermal Region (ST)	$[0, 6)$
`fr`	First Resonances (FR)	$[6, 100)$
`ir`	Intermediate Resonances (IR)	$[10^2, 10^3)$
`lr`	Last Resonances (LR)	$[10^3, 2 \times 10^4)$
`sf`	Fast/Smooth Region (SF)	$[2 \times 10^4, 2 \times 10^7]$

Table A.2: Energy ranges for local RMSE evaluation

Figure A.2 shows the results, with a logarithmic scale on the y-axis. As expected, the RMSE in the two smooth parts are negligible, but it is important to notice that the discrepancy in the high energy resonance interval, in absolute values, is substantially smaller than in the first part of the resonances. Moreover, increasing the number of groups has different effects at different temperatures: as expected, with the same increase in energy discretization, the broadened curves are easier to represent.

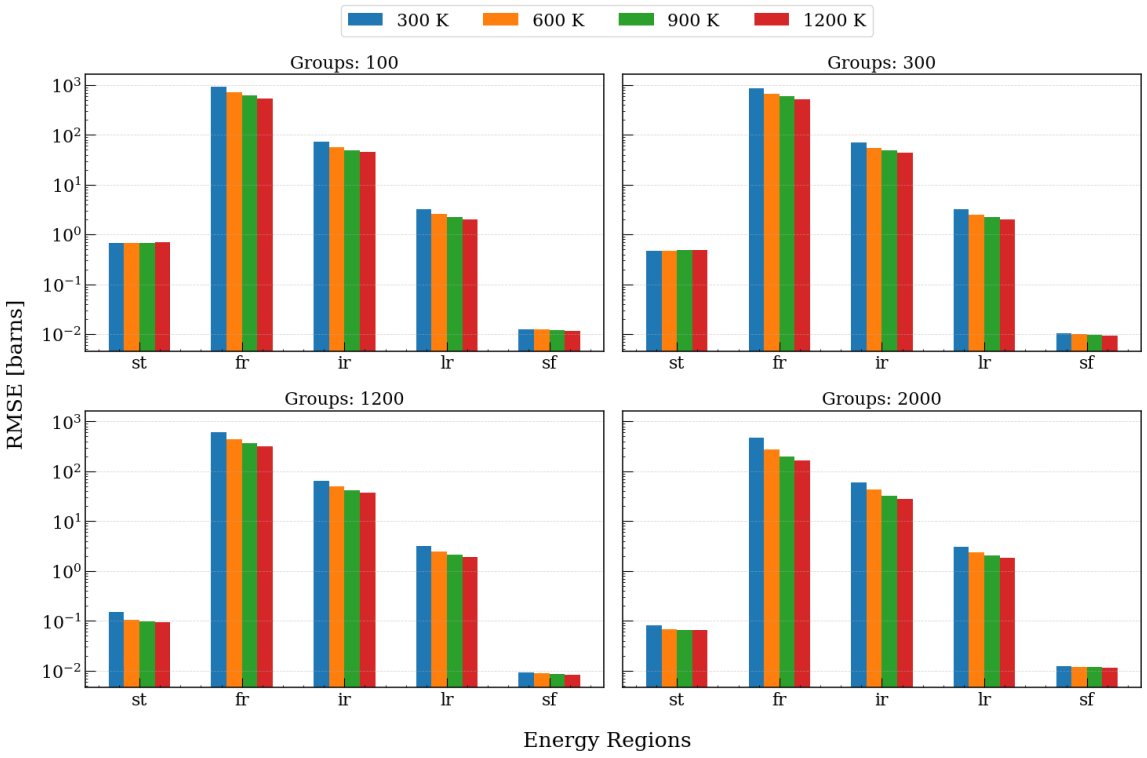


Figure A.2: Local RMSE inside five different energy regions

Appendix B

Flux and Reaction Rates inside the sample

This appendix provides a detailed analysis of the neutron flux and the reaction rates within the investigated sample. The spatial distributions and energy spectra are evaluated for two different experimental locations: the Graphite Reflector and the Core Periphery. Understanding these distributions is essential for assessing the uniformity of the contribution to reactivity and identifying localized physical phenomena, such as resonance self-shielding or macroscopic flux gradients.

B.1 Flux Spectra and Spatial Distributions

First, we analyze the energy distribution of the neutrons inside the sample. Figure B.1 presents the comparison of the flux spectra within the sample and without, located in the Core Periphery, in the full energy domain. Figure B.2 shows a magnified view around the energy interval comprising first major capture resonance of ^{238}U. The flux presents localized depression in correspondence to the peaks of the ^{238}U capture cross section, dominated by the first 4-5 resonances. The spectra are very similar to the one in the Graphite Reflector.

To evaluate the homogeneity of the neutron field, the spatial distribution of the total flux was extracted along different geometric axes. Figure B.3 illustrates the vertical cuts for the sample placed in the Graphite Reflector, while Figure B.4 and Figure B.5 show the horizontal and vertical cuts for the Core Periphery location, respectively.

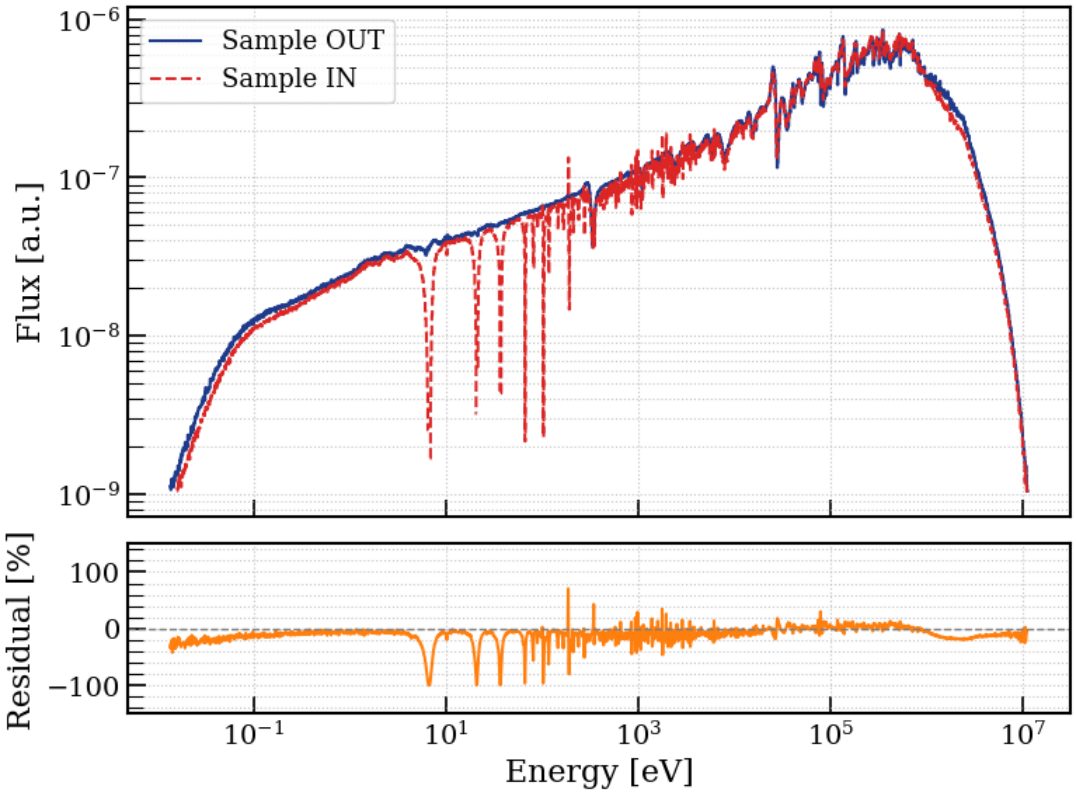


Figure B.1: Comparison of neutron flux without and inside the sample, in the Core Periphery assembly. Sample is at room temperature.

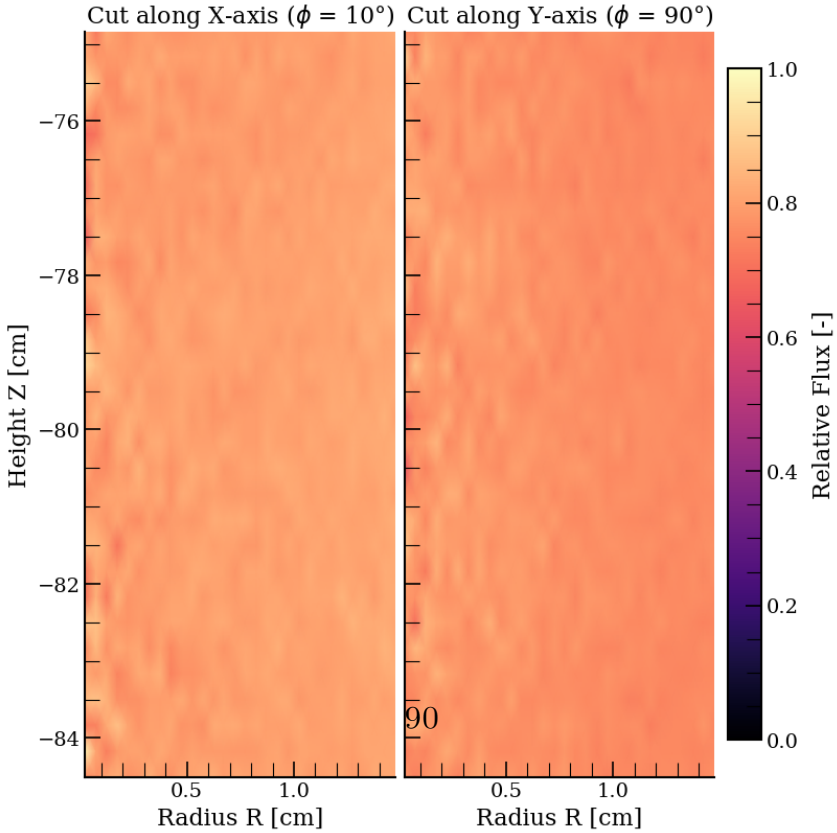


Figure B.3: Total flux spatial distribution in the sample located in the Graphite Reflector channel. The cuts are vertical, along two perpendicular orientations. The core midplane is located at z=79.64.

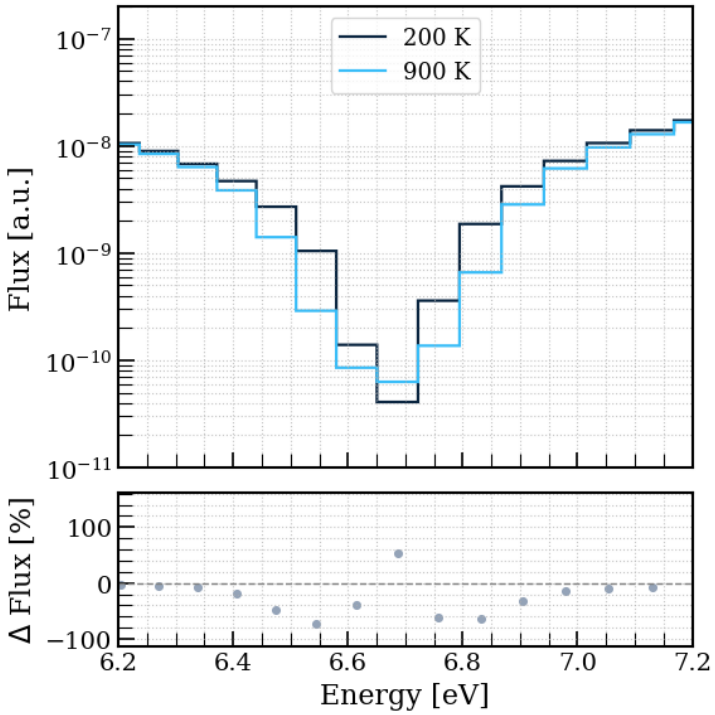


Figure B.2: Comparison of neutron flux around the first capture ^{238}U resonance, located at 6.7 [eV], inside the sample at 200 K and 900 K. Sample is inside the Core Periphery.

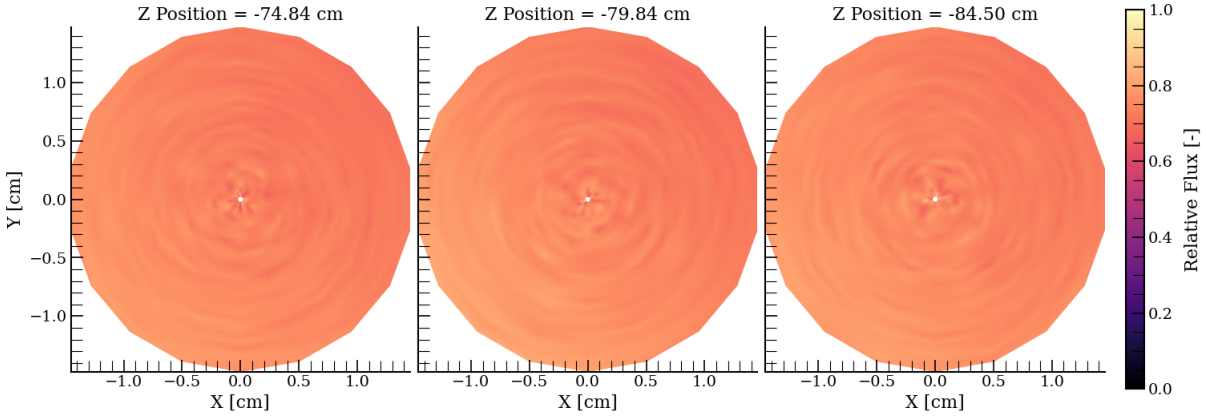


Figure B.4: Total flux spatial distribution in the sample located in the Core Periphery channel. The cuts are horizontal, along the middle and near the ends.

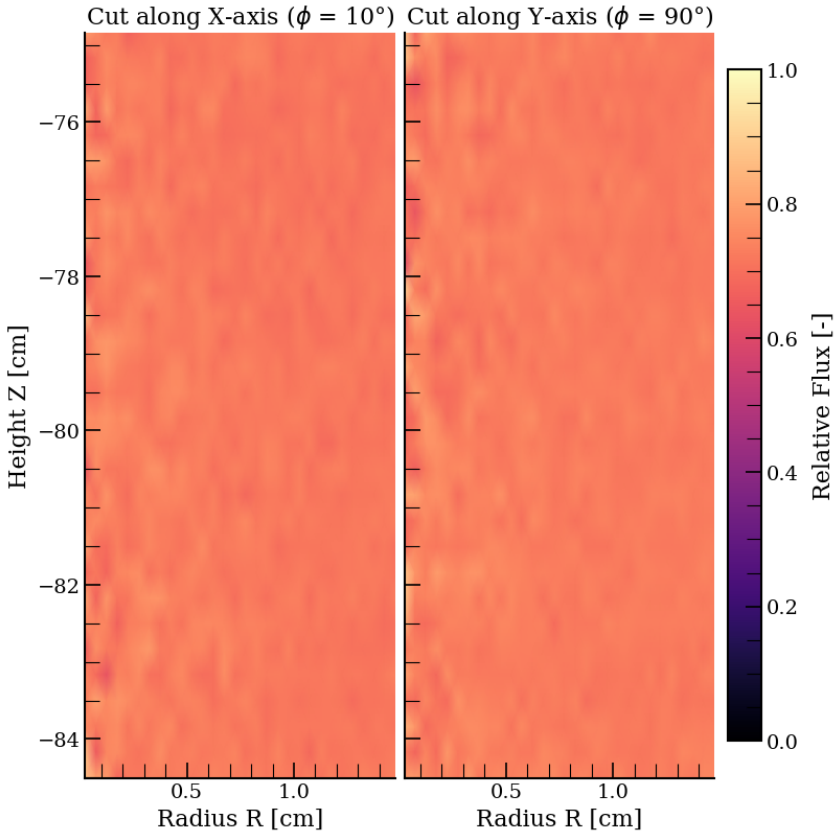


Figure B.5: Total flux spatial distribution in the sample located in the Core Periphery channel. The cuts are vertical, along two perpendicular orientations. The core midplane is located at z=79.64.

As is evident from these figures, the total neutron flux exhibits a remarkably flat profile across the entire sample volume, regardless of the orientation or the irradiation channel. No significant spatial self-shielding is detected for the total flux. This flat behavior indicates that the mean free path of the average neutron traversing the sample material is comparable to, or greater than, the sample diameter itself. Consequently, the overall neutron population does not suffer from heavy localized attenuation, resulting in an unperturbed, uniform total flux distribution.

B.2 Reaction Rates Spatial Distributions

While the total flux remains spatially uniform, specific reaction rates can exhibit local variations depending on the cross-section behavior of the material at certain energies.

B.2.1 Capture Reaction Rates

The spatial distributions of the normalized capture reaction rates at 300 K are reported in Figure B.6 for the Graphite Reflector, and in Figure B.7 and Figure B.8 for the Core Periphery.

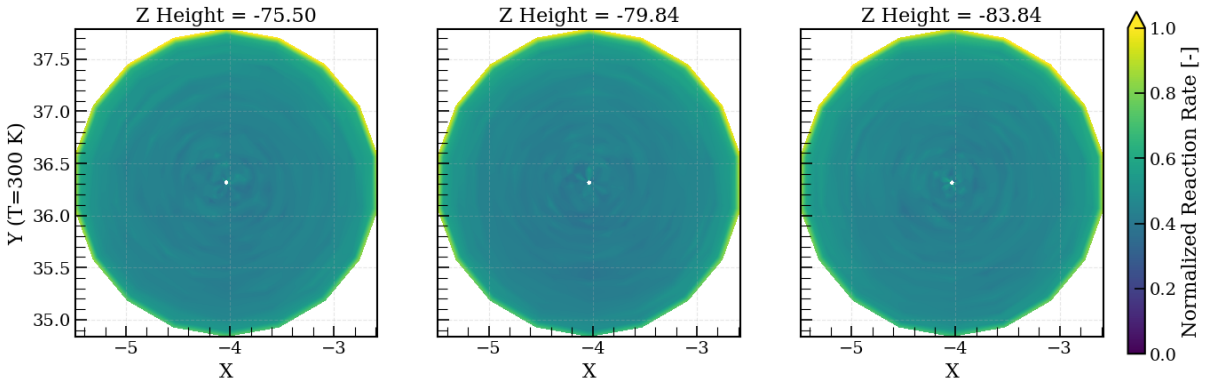


Figure B.6: Normalized capture reaction rate, at 300 K, in the sample inserted in the Graphite Reflector channel. The cut is horizontal, at three heights.

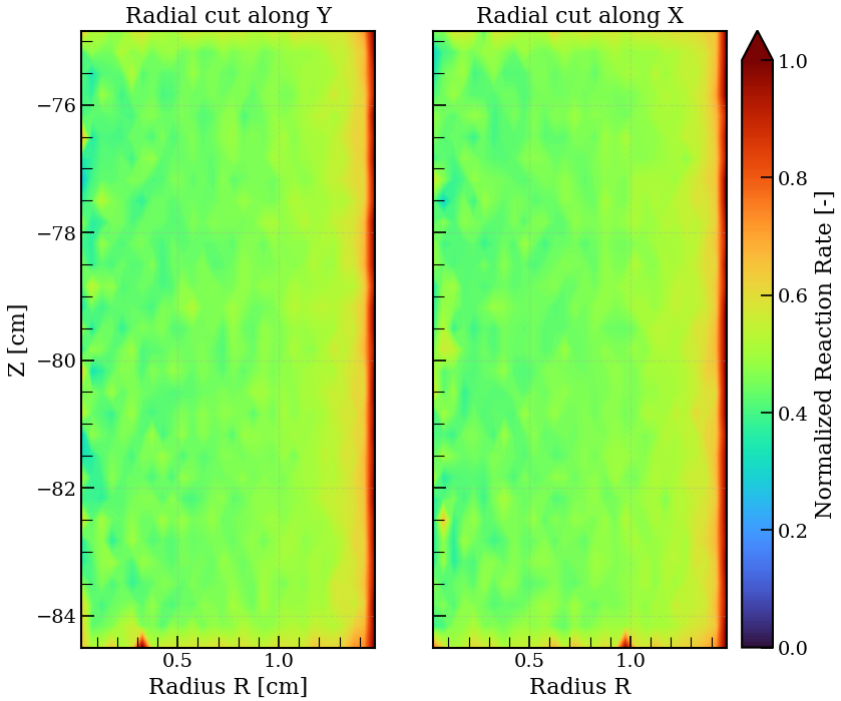


Figure B.7: Normalized capture reaction rate, at 300 K, in the sample inserted in the Core Periphery channel. The cut is vertical, along two directions.

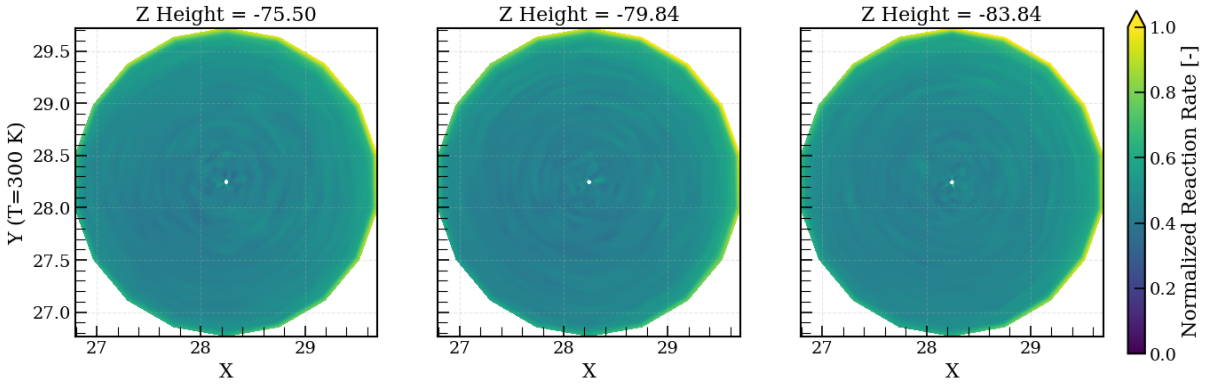


Figure B.8: Normalized capture reaction rate, at 300 K, in the sample inserted in the Core Periphery channel. The cut is horizontal, at three heights.

Unlike the total flux, the capture reaction rates display a noticeable concentration effect on the external shell of the sample. This phenomenon is driven by resonance capture. Neutrons at these resonance peak energies are strongly and rapidly absorbed within the very first outer layers of the sample. As a result, the inner volume is shielded from these specific resonance-energy neutrons, leading to higher capture rates at the boundaries and a depression toward the center.

B.2.2 Fission Reaction Rates

In contrast to the effect observed for capture, the spatial distribution of the fission reaction rates is predominantly governed by the macroscopic geometry of the reactor. Fission rates do not show the same local outer-shell concentration; instead, they exhibit a spatial gradient where the reaction rate is strictly proportional to the physical distance from the active part of the core. The sample regions facing the active core experience a larger neutron spectrum, leading to higher localized fission rates that smoothly decrease as the distance from the fuel increases.

In conclusion, the total reaction rates are completely homogeneous over all the geometrical domain.

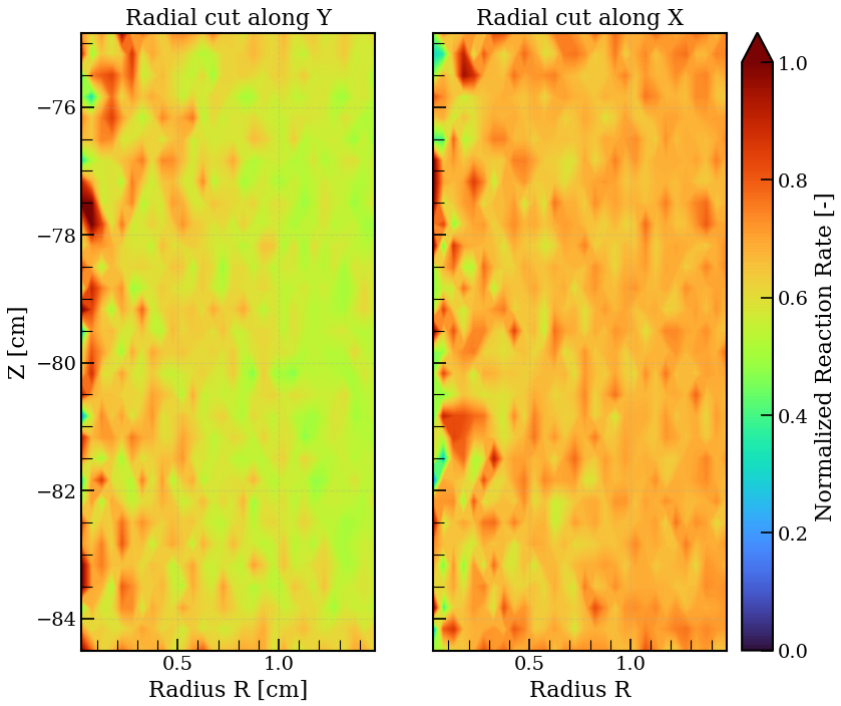


Figure B.9: Normalized fission reaction rate in the sample inserted in the Graphite Reflector channel. The cut is vertical, along two directions.

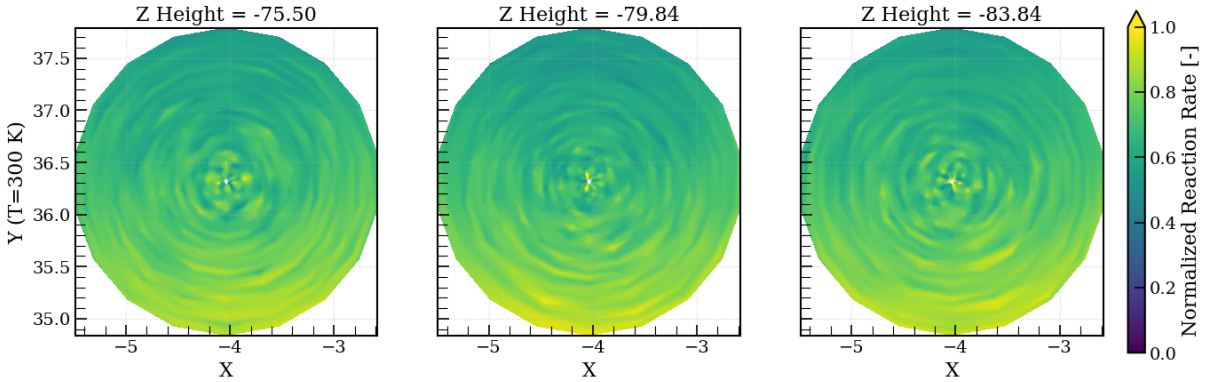


Figure B.10: Normalized fission reaction rate in the sample inserted in the Graphite Reflector channel. The cut is horizontal, at three heights.

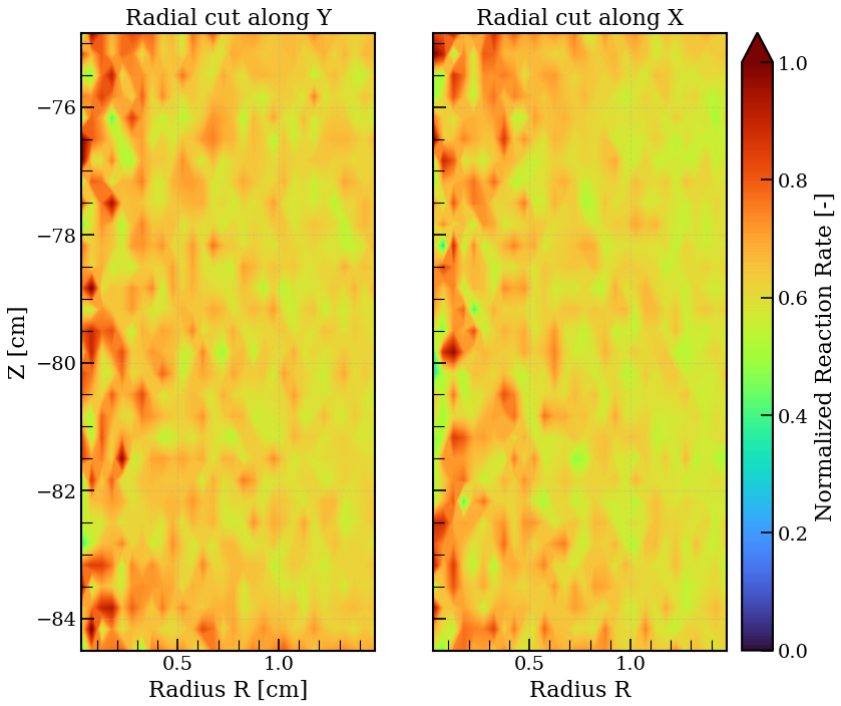


Figure B.11: Normalized fission reaction rate in the sample inserted in the Core Periphery channel. The cut is vertical, along two directions.

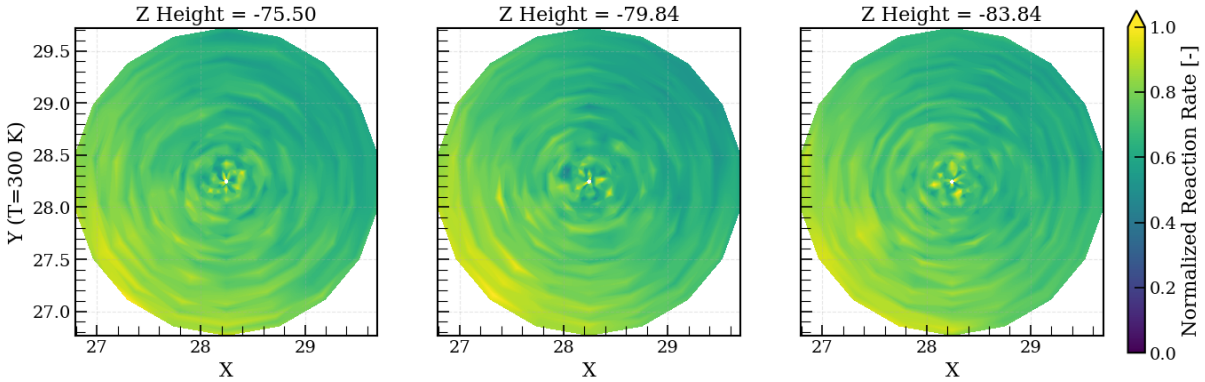


Figure B.12: Normalized fission reaction rate in the sample inserted in the Core Periphery channel. The cut is horizontal, at three heights.

Bibliography

[1] International Energy Agency. *Nuclear Power and Secure Energy Transitions: From Today's Challenges to Tomorrow's Clean Energy Systems*. IEA Report. Paris: International Energy Agency (IEA), June 2022. URL: https://www.iea.org/reports/nuclear-power-and-secure-energy-transitions (cit. on p. 1).

[2] Igor L. Pioro and Gilles H. Rodriguez. «Generation IV International Forum (GIF)». In: *Handbook of Generation IV Nuclear Reactors*. Ed. by Igor Pioro. 2nd. Duxford, United Kingdom: Woodhead Publishing, 2023. Chap. 2, pp. 111–132. ISBN: 978-0128205884 (cit. on p. 1).

[3] Generation IV International Forum. *2024 GIF Annual Report*. Annual Report. OECD Nuclear Energy Agency (NEA) for the Generation IV International Forum, July 2024. URL: https://www.gen-4.org/resources/annual-reports/2024-gif-annual-report (cit. on p. 1).

[4] A. A. Ryzhkov, G. V. Tikhomirov, and M. Yu. Ternovykh. «Nuclear data needs for fast reactors». In: *Proceedings of the International Conference on Fast Reactors and Related Fuel Cycles (FR26)*. FR26-023. International Atomic Energy Agency (IAEA). Beijing, China, May 2026. URL: https://conferences.iaea.org/event/436/contributions/38360/ (cit. on p. 1).

[5] Dimitar G. Chereshkov, Mikhail Yu. Ternovykh, Georgiy V. Tikhomirov, and Alexander A. Ryzhkov. «Nuclear data uncertainty on generation IV fast reactors criticality calculations analysis comparison». In: *Nuclear Energy and Technology* 9.3 (2023). DOI: 10.3897/nucet.9.111919 (cit. on p. 1).

[6] S. Panizo, C. Alfonso, and A. Jiménez-Carrascosa et al. «Sensitivity and uncertainty analyses for advanced nuclear systems (ALFRED, ASTRID, ESFR and MYRRHA)». In: *Progress in Nuclear Energy* 172 (2024), p. 105207. ISSN: 0149-1970. DOI: https://doi.org/10.1016/j.pnucene.2024.105207 (cit. on p. 2).

[7] Hamid Aït Abderrahim, Peter Baeten, Didier De Bruyn, Jan Heyse, Paul Schuurmans, and Jan Wagemans. «MYRRHA, a Multipurpose hYbrid Research Reactor for High-end Applications». In: *Nuclear Physics News* 20.1 (2010), pp. 24–28. DOI: 10.1080/10506890903178913 (cit. on p. 2).

[8] Luca Fiorito, Matteo Zanetti, and Federico Grimaldi et al. «Uncertainty Quantification for the Doppler Reactivity Feedback Coefficient of MYRRHA». In: *Nuclear Science and Engineering* 199.sup1 (2025), S56–S72. DOI: 10.1080/00295639.2024.2353987 (cit. on pp. 2, 18, 36, 73).

[9] W K Foell. *Small-sample reactivity measurements in nuclear reactors*. American Nuclear Society, 1972. URL: https://www.osti.gov/biblio/4351459 (cit. on p. 3).

[10] R. M. Pearce and D. H. Walker. «A Direct Measurement of the Uranium Metal Temperature Coefficient of Reactivity». In: *Nuclear Science and Engineering* 2 (1957), pp. 24–32 (cit. on pp. 3, 6).

[11] Wikipedia contributors. *ZEEP — Wikipedia, The Free Encyclopedia*. [Online; visited on 10-august-2026]. 2026. URL: https://en.wikipedia.org/wiki/ZEEP (cit. on p. 3).

[12] W. Y. Kato and D. K. Butler. «Measurement of the Doppler Temperature Effect in an EBR-I Type Assembly». In: *Nuclear Science and Engineering* 5.5 (1959), pp. 320–330. DOI: 10.13182/NSE59-A25604 (cit. on pp. 3, 4, 6, 74).

[13] J. M. Gasidlo, J. K. Long, and W. P. Keeney. *Doppler Effect Measurements, Sodium Void Coefficients and Critical Studies of a 5,000-Liter Fast Power Breeder Reactor by the Two-Zone Method (ZPR-III Assembly 43)*. Tech. rep. ANL-6838. Argonne, Illinois: Argonne National Laboratory, May 1964 (cit. on pp. 4–6).

[14] Japan Atomic Energy Agency. *Critical Assemblies – Nuclear Science Research Institute*. https://www.jaea.go.jp/04/ntokai/en/facility/critical.html. Nuclear Science Research Institute, JAEA. 2024 (cit. on p. 4).

[15] Masaki Andoh, Masahiro Fukushima, Shigeaki Okajima, and Kenji Kawasaki. «Measurement and Analysis of ^{238}U Doppler Reactivity Effect in FCA Cores Simulating Light-Water-Moderated MOX Fuel Lattices». In: *Journal of Nuclear Science and Technology* 44.4 (2007), pp. 537–547. DOI: 10.1080/18811248.2007.9711306 (cit. on pp. 4–6, 44).

[16] P. Puthiyavinayagam. *Fast Reactor Core Design – Module 2: Core Neutronics*. Lecture Notes SMR 2055-8. Joint ICTP/IAEA School on Physics and Technology of Fast Reactors Systems. The Abdus Salam International Centre for Theoretical Physics (ICTP) / International Atomic Energy Agency (IAEA), 2009 (cit. on p. 5).

[17] U.S. Nuclear Regulatory Commission. *Westinghouse Technology Advanced Manual, Section 2.1: Reactor Physics Review*. Tech. rep. R-304P. Revision 0519. U.S. NRC Technical Training Center, Jan. 2011. URL: https://www.nrc.gov/docs/ML1125/ML11258A304.pdf (cit. on p. 5).

[18] A. Kochetkov, H. Aït Abderrahim, and P. Baeten et al. «Integral experiments in the VENUS-F reactor». In: *Annals of Nuclear Energy* 157 (2021), p. 108230. ISSN: 0306-4549. DOI: https://doi.org/10.1016/j.anucene.2021.108230 (cit. on pp. 6, 7).

[19] Federico Di Croce, Federico Grimaldi, Antonin Krása, Pierre-Etienne Labeau, Guido Vittiglio, and Jan Wagemans. «Oscillation experiment design at the VENUS-F fast reactor». In: *EPJ Web of Conferences* (2025). URL: https://api.semanticscholar.org/CorpusID:283021531 (cit. on pp. 7, 8).

[20] Krása, Antonín, Kochetkov, Anatoly, Baeten, Peter, Vittiglio, Guido, Wagemans, Jan, and Bécares, Vicente. «Comparative study on neutron data in integral experiments of MYRRHA mockup critical cores in the VENUS-F reactor». In: *EPJ Web Conf.* 146 (2017), p. 06019. DOI: 10.1051/epjconf/201714606019. URL: https://doi.org/10.1051/epjconf/201714606019 (cit. on p. 7).

[21] George I. Bell and Samuel Glasstone. *Nuclear Reactor Theory*. Washington, D.C.: U.S. Atomic Energy Commission, 1970 (cit. on pp. 10, 12).

[22] Elmer E. Lewis and Warren F. Miller. *Computational Methods of Neutron Transport*. New York: John Wiley & Sons, 1984. ISBN: 9780471092452 (cit. on p. 11).

[23] F. Di Croce, P. Leconte, F. Grimaldi, A. Krása, {P. E.} Labeau, and J. Wagemans. «Small Sample Reactivity Worth Calculation: Comparison of Serpent2 and TRIPOLI4 Perturbation Techniques». In: *Proceedings of the International Conference on Mathematics and Computational Methods Applied to Nuclear Science and Engineering, M and C 2025*. United States: American Nuclear Society, 2025, pp. 1156–1165. DOI: 10.13182/MC25-47168 (cit. on p. 12).

[24] Alireza Haghighat. *Monte Carlo Methods for Particle Transport*. 2nd. CRC Press, 2020. ISBN: 9780367503888 (cit. on p. 13).

[25] Patrick Billingsley. *Probability and Measure*. 3rd. New York: John Wiley & Sons, 1995. ISBN: 978-0471007104 (cit. on p. 13).

[26] Iván Lux and László Koblinger. *Monte Carlo Particle Transport Methods: Neutron and Photon Calculations*. CRC Press, 1991. DOI: 10.1201/9781351074834 (cit. on pp. 14, 15).

[27] M. Aufiero, M. Martin, and M. Fratoni. «XGPT: Extending Monte Carlo Generalized Perturbation Theory capabilities to continuous-energy sensitivity functions». In: *Annals of Nuclear Energy* 96 (2016), pp. 295–306 (cit. on p. 15).

[28] Pierre Leconte and Alain Santamarina. «OECD EGBUC Benchmark VIII – Comparison of calculation codes and methods for the analysis of small-sample reactivity experiments». In: *PHYSOR2014*. Kyoto, Japan, Sept. 2014 (cit. on p. 15).

[29] Averill M. Law. *Simulation Modeling and Analysis*. 5th. McGraw-Hill Education, 2015. ISBN: 978-0073401324 (cit. on p. 16).

[30] Joint Committee for Guides in Metrology. *Evaluation of measurement data — Guide to the expression of uncertainty in measurement*. Tech. rep. JCGM 100:2008. BIPM, 2008 (cit. on p. 17).

[31] John R. Lamarsh and Anthony J. Baratta. «Introduction to Nuclear Engineering». In: 3rd. Upper Saddle River, NJ: Prentice Hall, 2001. Chap. 7. ISBN: 978-0201824988 (cit. on p. 17).

[32] Elmer E. Lewis. *Nuclear Power Reactor Safety*. New York, NY, USA: John Wiley & Sons, 1977. ISBN: 978-0471531883 (cit. on p. 17).

[33] R.B. Nicholson and E.A. Fisher. «The Doppler effect in fast reactors». In: *Advances in Nuclear Science and Technology*. Ed. by Paul Greebler and Ernest J. Henley. Academic Press, 1968. ISBN: 978-1-4831-9958-0. DOI: https://doi.org/10.1016/B978-1-4831-9958-0.50009-2 (cit. on pp. 17, 18, 33).

[34] Jaakko Leppänen, Ville Valtavirta, Antti Rintala, and Riku Tuominen. «Status of Serpent Monte Carlo code in 2024». In: *EPJ - Nuclear Sciences Technologies* 11 (2025). ISSN: 2491-9292. DOI: https://doi.org/10.1051/epjn/2024031 (cit. on p. 18).

[35] Jaakko Leppänen. *Serpent – A Continuous-energy Monte Carlo Reactor Physics Burnup Calculation Code User's Manual*. VTT Technical Research Centre of Finland. Espoo, Finland, 2015. URL: https://serpent.vtt.fi/ (cit. on pp. 19, 33).

[36] Los Alamos National Laboratory. *About – NJOY21*. https://www.njoy21.io/about. Accessed: 2026-08-17 (cit. on p. 20).

[37] Robert E. MacFarlane, Douglas W. Muir, Rose M. Boicourt, Albert C. Kahler, and Albert C. Kahler III. *The NJOY Nuclear Data Processing System, Version 2016*. Tech. rep. LA-UR-17-20093. Los Alamos, NM, USA: Los Alamos National Laboratory, 2017 (cit. on pp. 20, 38).

[38] V. Alessi et al. *SANDY: A sensitivity analysis and uncertainty quantification tool for nuclear data*. Available at: https://github.com/sandy-group/sandy. 2020 (cit. on pp. 21, 22).

[39] Luca Fiorito. *SANDY: Sampling Tool for Nuclear Data Documentation*. Accessed: 2026-08-17. 2021. URL: https://luca-fiorito-11.github.io/sandy-docs/ (cit. on p. 21).

[40] Wes McKinney. *Python for Data Analysis: Data Wrangling with pandas, NumPy, and Jupyter*. O'Reilly Media, 2022 (cit. on p. 22).

[41] Andrew P. Johnson et al. «serpentTools: A Python package for the analysis of Serpent Monte Carlo input and output files». In: *Journal of Open Source Software* 4.43 (2019), p. 1764. DOI: 10.21105/joss.01764 (cit. on p. 22).

[42] J. D. Hunter. «Matplotlib: A 2D graphics environment». In: *Computing in Science & Engineering* 9.3 (2007), pp. 90–95 (cit. on p. 22).

[43] Michael L. Waskom. «seaborn: statistical data visualization». In: *Journal of Open Source Software* 6.60 (2021), p. 3021. DOI: 10.21105/joss.03021. URL: https://doi.org/10.21105/joss.03021 (cit. on p. 22).

[44] Federico Grimaldi, Federico Di Croce, and Antonin Krása et al. «The CoRREx neutron spectrum filtering campaign at VENUS-F for calculation-to-experiment discrepancy interpretation». In: *Annals of Nuclear Energy* 219 (2025), p. 111425. ISSN: 0306-4549. DOI: https://doi.org/10.1016/j.anucene.2025.111425 (cit. on p. 23).

[45] Ligonnet Thomas, Laureau Axel, and Simbsler Philippe et al. «Design of an Open-Loop Pile-Oscillation Program in the CROCUS Reactor». In: *IEEE Transactions on Nuclear Science* 71.5 (2024), pp. 1001–1009. DOI: 10.1109/TNS.2024.3371183 (cit. on p. 36).

[46] Juan José Gómez Rodriguez, Alexander Knospe, and Marco Viebach et al. «Monte Carlo modelling of the AKR-2 training and research reactor». In: *Annals of Nuclear Energy* 231 (2026), p. 112217. ISSN: 0306-4549. DOI: https://doi.org/10.1016/j.anucene.2026.112217 (cit. on p. 36).

[47] Plompen A., Cabellos O., and De Saint Jean C. et al. «The Joint Evaluated Fission and Fusion Nuclear Data Library, JEFF-3.3». In: *EUROPEAN PHYSICAL JOURNAL A* 56 (2020), p. 181. ISSN: 1434-6001 (online). DOI: 10.1140/epja/s10050-020-00141-9(online) (cit. on p. 37).

[48] Weston M. Stacey. «Nuclear Reactor Physics». In: 2nd. Weinheim: Wiley-VCH, 2007. Chap. 4. ISBN: 9783527406791 (cit. on p. 40).

[49] William Boyd, Adam Nelson, and Paul K. Romano et al. «Multigroup Cross-Section Generation with the OpenMC Monte Carlo Particle Transport Code». In: *Nuclear Technology* 205.7 (2019), pp. 928–944. DOI: 10.1080/00295450.2019.1571828 (cit. on p. 40).

[50] Tung Dong Cao Nguyen, Hyunsuk Lee, and Deokjung Lee. «Use of Monte Carlo code MCS for multigroup cross section generation for fast reactor analysis». In: *Nuclear Engineering and Technology* 53.9 (2021), pp. 2788–2802. ISSN: 1738-5733. DOI: https://doi.org/10.1016/j.net.2021.03.005 (cit. on p. 40).

[51] Ho Jin Park, Hyung Jin Shim, Han Gyu Joo, and Chang Hyo Kim. «Generation of Few-Group Diffusion Theory Constants by Monte Carlo Code McCARD». In: *Nuclear Science and Engineering* 172.1 (2012), pp. 66–77. DOI: 10.13182/NSE11-22 (cit. on p. 40).

[52] H. H. Ku. «Notes on the Use of Propagation of Error Formulas». In: *Journal of Research of the National Bureau of Standards, Section C* 70C.4 (1966), pp. 262–273. DOI: 10.6028/jres.070c.025 (cit. on pp. 47, 48).

[53] Sheldon M. Ross. *Introduction to Probability and Statistics for Engineers and Scientists*. 5th. TA340.R67 2014. London, UK: Academic Press (Elsevier), 2014. ISBN: 978-0-12-394811-3 (cit. on p. 48).

[54] Theodore Wilbur Anderson. *An Introduction to Multivariate Statistical Analysis*. 3rd. Wiley Series in Probability and Statistics. Chapter 2, Section 2.2.3. Hoboken, New Jersey: John Wiley & Sons, 2003. ISBN: 978-0471360919 (cit. on p. 48).

[55] Virtanen Pauli, Gommers Ralf, and Oliphant Travis E. et al. «SciPy 1.0: Fundamental Algorithms for Scientific Computing in Python». In: *Nature Methods* 17 (2020), pp. 261–272. DOI: 10.1038/s41592-019-0686-2 (cit. on p. 59).

[56] Nuclear Power. *Self-shielding - Energy and Spatial | Definition*. nuclear-power.com. URL: https://www.nuclear-power.com/nuclear-power/reactor-physics/nuclear-engineering-fundamentals/neutron-nuclear-reactions/self-shielding/ (visited on 09/07/2026) (cit. on p. 61).